



universität  
wien

# DIPLOMARBEIT

Titel der Diplomarbeit

Investigation of seismic reflectors in the lower lithosphere  
of the Eastern Alps and adjacent regions

angestrebter akademischer Grad

Magister der Naturwissenschaften (Mag. rer.nat.)

Verfasser: Thomas Oeberseder

Matrikel-Nummer: 0403430

Studienrichtung: A416 Geophysik

Betreuer: Univ.Prof.Dr.Dipl.Ing. Ewald Brückl

Wien, im September 2009



## Zusammenfassung

Die Analyse von seismischen Weitwinkel-Reflexionsdaten, akquiriert während der seismischen Experimente CELEBRATION 2000 und ALP 2002 in Mitteleuropa, zeigt neben bekannten seismischen Signalen aus der Erdkruste und der Erdkrusten-Erdmantelgrenze auch signifikante Reflexionseinsätze bei größeren Offsets. Diese Einsätze stammen möglicherweise von einem Reflektor im oberen Mantel. Mittels Laufzeitinversion wurden im Rahmen der vorliegenden Arbeit Tiefe und Struktur dieses Reflektors ermittelt. Um ein bestmögliches Resultat zu erzielen, mussten die Reflexionslaufzeiten so genau wie möglich gepickt werden. Zur Hilfestellung wurden mittels Ray Tracing Reflexionslaufzeiten für verschiedene Reflektor-Tiefenmodelle (55 km, 60 km, 70 km und 80 km) modelliert. Nach einer Optimierung der Laufzeitpicks wurden diese nach Tiefe und Struktur invertiert, wobei ein iteratives Verfahren zum Einsatz kam. Das zugrunde liegende Krustengeschwindigkeitsmodell basiert auf bereits existierenden Ergebnissen der oben genannten Experimente. Die Geschwindigkeitsverteilung im oberen Mantel ist hingegen nicht ausreichend bekannt; die Inversion wurde daher für drei Mantelgeschwindigkeitsmodelle (Geschwindigkeitsgradienten  $0.01 \text{ s}^{-1}$ ,  $0.005 \text{ s}^{-1}$  und  $0.002 \text{ s}^{-1}$ ) durchgeführt. Da die Beziehung zwischen Laufzeit und Reflektortiefe nicht linear ist, wurden jeweils drei Iterationen ausgeführt. Von den resultierenden drei Reflektor-Tiefenmodellen wies jenes basierend auf einem Gradienten von  $0.005 \text{ s}^{-1}$  die geringsten Laufzeitfehler auf und wird daher als plausibelstes Ergebnis angesehen.

Der subhorizontale Reflektor befindet sich in einer Tiefe von durchschnittlich 55 km und liegt geographisch gesehen im Grenzgebiet zwischen Österreich, Ungarn und der Slowakei. Geologisch stellt dieses Gebiet die Übergangszone zwischen Ostalpen und Karpaten dar. Die Entstehung des Reflektors kann womöglich mit der Intrusion von mafischen Material in die Lithosphäre in Verbindung gebracht werden. Diese Interpretation wird durch Schwereanomalien und hohe Unterkrustengeschwindigkeiten im Untersuchungsgebiet unterstützt.

In manchen seismischen Sektionen ist zusätzlich ein zweiter Reflexionseinsatz erkenntlich. Dieser wurde als zweiter Reflektor in größerer Tiefe ( $\sim 70 \text{ km}$ ) interpretiert.

## Abstract

Analysis of seismic wide-angle reflection data acquired during the CELEBRATION 2000 and ALP 2002 experiments in Central Europe reveal – besides known phases – significant reflection events at greater offsets. These most likely originate from an upper mantle reflector. Travel times correlated with this reflector have been inverted to determine its depth and shape. In order to get the best possible result, reflection travel times had to be picked as accurately as possible. Based on ray tracing, travel times have been modelled for several reflector depth models (55 km, 60 km, 70 km and 80 km) to support the picking. After having optimised the amount of travel time picks, an iterative inversion scheme was applied. The underlying crustal velocity model was based on the results of the above mentioned experiments. The dependence of the upper mantle velocities with depth, in contrary, is less known; inversion has therefore been carried out for three different velocity models (mantle velocity gradients of  $0.01 \text{ s}^{-1}$ ,  $0.005 \text{ s}^{-1}$  and  $0.002 \text{ s}^{-1}$ ). Since the relationship between travel time and reflector depth is non-linear, three iterations were carried out. In terms of travel time errors, the reflector depth model based on a gradient of  $0.005 \text{ s}^{-1}$  showed the best performance and is therefore considered as the most plausible result.

The reflector lies in a depth of  $\sim 55 \text{ km}$  and is situated geographically in the border area of Austria, Hungary and Slovakia. This region represents the transition zone between Eastern Alps and the Carpathians. The reflector origin may be related to intrusion of mafic material into the upper mantle and lower crust. This assumption is further supported by positive gravity anomalies and high lower crustal velocities in our area of investigation.

On some seismic sections additional second reflective events appear. These have been interpreted as a second reflector in a depth of  $\sim 70 \text{ km}$ .

# Content

---

<b>1</b>	<b>Introduction</b>	<b>7</b>
1.1	Tectonic setting of the investigation area	8
1.2	Objective of this thesis	10
<b>2</b>	<b>Reflectors in the uppermost mantle</b>	<b>11</b>
2.1	Petrophysical parameters of crust and mantle	11
2.2	Evidence for upper mantle reflectors	13
2.3	Categories of mantle reflections	14
2.4	Geological models for upper mantle reflectivity	16
<b>3</b>	<b>Theory of travel time modelling and inversion</b>	<b>18</b>
3.1	Eikonal equation	18
3.2	Methods based on ray tracing	20
3.1.1	Ray tracing equations	20
3.1.2	Initial-value ray tracing	25
3.1.3	Two-point ray tracing	25
3.3	Finite difference method	27
3.4	Travel time inversion	31
3.5	Parameterization of the velocity model	34
<b>4</b>	<b>Data and correlation of travel times</b>	<b>35</b>
<b>5</b>	<b>Modelling of ‘R1’- travel times</b>	<b>41</b>
5.1	Initial estimation of the reflector depth	41
5.2	Travel time computation based on the ray tracing equations (program ‘ANRAY’)	48
5.2.1	Depth and velocity model	48
5.2.2	Travel time computation for pre-defined reflector models	50
5.3	Travel time computation based on the finite difference approach	57
5.3.1	Velocity parameterization	57
5.3.2	Introduction of interfaces	57
5.3.3	Forward modelling of travel times for pre-defined reflector models	59
5.3.4	Comparison with ‘ANRAY’-computed travel times	60
5.4	Inversion results	61

<b>6</b>	<b>Interpretation of ‘R2’- travel times</b>	<b>73</b>
<b>7</b>	<b>Comparison with related studies and tectonic interpretation</b>	<b>77</b>
<b>8</b>	<b>Conclusion and outlook</b>	<b>81</b>
<b>A</b>	<b>Appendix</b>	<b>83</b>
A.1	Inversion program by Hole (1996)	83
A.2	Description of the program ‘ANRAY’	88
	<b>References</b>	<b>93</b>

# 1 Introduction

The complicated geologic setting of Central Europe has been attracting scientific interests for several decades with numerous extensive wide-angle reflection and refraction experiments carried out in recent years. Amongst them are the POLONAISE 1997, CELEBRATION 2000, ALP 2002 and SUDETES 2003 experiments, which aimed for a better understanding of the structure and the evolution of the lithosphere, with a special focus on the investigation of the crustal structure [Brückel *et al.* 2007]. A network of arbitrarily oriented and intersecting seismic profiles cover most of Central Europe from northern Poland down to northern Italy and even further to Croatia (Figure 1.1).

The seismic profiles of ALP 2002 and CELEBRATION 2000 (Figure 1.1) are used for this thesis. Geologically, this region extends from the Bohemian massif to the north, across the Molasse basin, the Eastern and Southern Alps to the Dinarides in the south, and the Panonnian basin in the south-east.

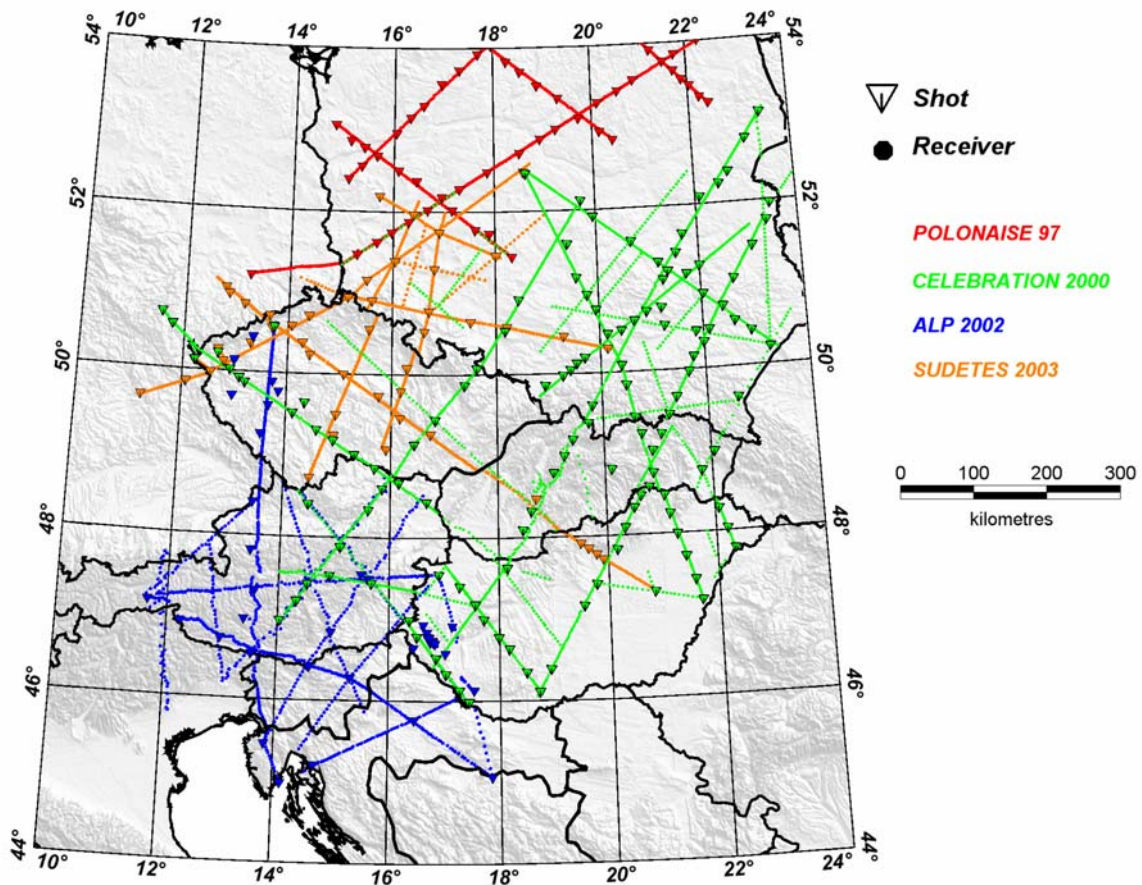
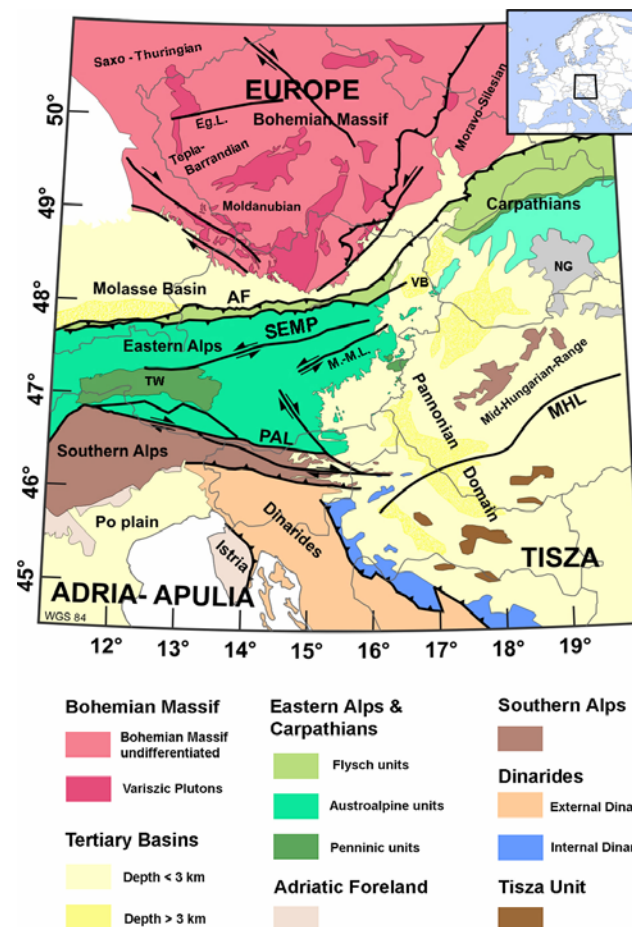


Figure 1.1. Field layout of recent large wide-angle reflection/refraction experiments in Central Europe [Behm *et al.* 2007].

## 1.1 Tectonic setting of the investigation area [from Behm et al. 2007 and references therein]

The major geologic units of the Eastern Alps and their surrounding tectonic provinces are shown in *Figure 1.2*. The Bohemian massif in the north represents the European platform. To the south, European crust dips below the Molasse basin, the foreland of the Alpine orogen. The Molasse basin is overthrust to the north by the accretionary wedge of the Eastern Alps, which comprises the Flysch belt and the Austro-Alpine nappes. European crust has been exhumed in the Tauern Window. The Periadriatic lineament (PAL) is a distinct fault and separates the Eastern Alps from the Southern Alps.

The Southern Alps share similar lithologies with the Eastern Alps, but need to be distinguished by their tectonic evolution with a southward directed vergency. They are bounded to the south by the External Dinarides and the Adriatic foreland (Po plain and the Istria peninsula). To the north-east, the Eastern Alps continue into the Carpathians. The Pannonian domain, which comprises parts of the Internal Dinarides and the Tisza unit, marks the south-eastern border of the Eastern Alps. The Pannonian domain is characterised by deep sedimentary basins and high heat flow. The Mid-Hungarian Line (MHL), an important SW-NE trending fault zone, runs through the Pannonian domain.



**Figure 1.2.** Tectonic setting of the investigated area [Behm et al. 2007], generalized after Schmid et al. 2004, Doglioni & Bosselini 1987, and others. SEMP: Salzach-Enns-Mariazell-Puchberg line; M.-M.L: Mur-Muerz line; Eg.L: Eger line; AF: Alpine Front; PAL: Periadriatic lineament; MHL: Mid-Hungarian Line; TW: Tauern Window; VB: Vienna Basin; NG: Neogene Volcanics.



Most elements of the present-day crustal structure result from tectonic events since the opening of the Atlantic and Indian Ocean in the Jurassic. The anticlockwise rotation of Africa with respect to Europe was followed by convergence between Europe and Africa in the Cretaceous, leading to a first phase of Alpine orogenic activity. In the Oligocene, the closure of the Alpine ocean basins led to the collision of the Adriatic microplate (subplate of Africa) with the European platform, causing a second phase of Alpine orogenic activity. Thereafter, in the late Oligocene and early Miocene, roll-back of the south-westward Carpathian subduction zone generated the Vienna and Pannonian basins. The ongoing movement of the Adriatic plate towards Europe also formed the Dinaridic orogen. Since the late Oligocene and early Miocene, the ongoing north-south oriented compression of the Eastern Alps has been accompanied by vertical and lateral extrusion and tectonic escape of large crustal wedges to the unconstrained margin represented by the Pannonian basin in the east.

The results of the ALP 2002/CELEBRATION 2000 experiments provided new insights into the crustal structure of the Eastern Alps, revealing some features that have been unknown until recently (Figure 1.3, Behm et al. 2007). Amongst them is a remarkable jump in Moho depth from approximately 37 km to 27-29 km at the transition zone between the Alpine domain and the Pannonian domain. This change in Moho depth separates an interpreted Pannonian fragment from the Adriatic microplate. It is regarded as a consequence of crustal thinning due to tectonic escape from the Alpine collision area to the unconstrained margin represented by the Pannonian basin since the late Oligocene to early Miocene.

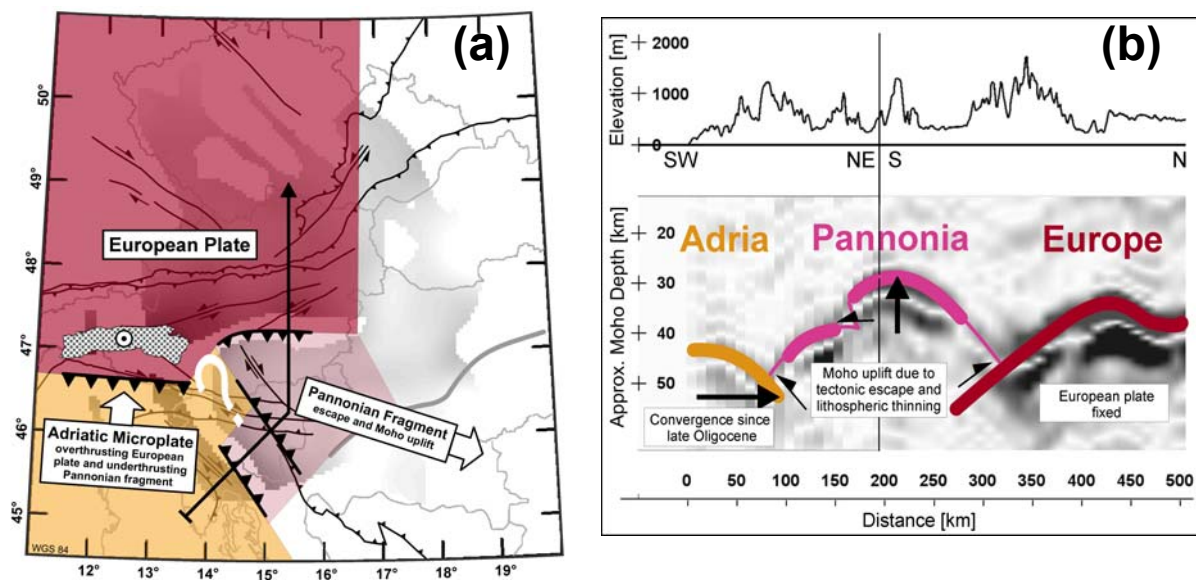


**Figure 1.3.** (a) Results from CELEBRATION 2000/ALP 2002 experiments reveal a new tectonic feature, the Pannonian Fragment, which forms a triple junction with the European Plate and the Adriatic Microplate, which underthrusts this fragment. (b) The newly discovered plate boundary is indicated by a shift in Moho depth from approximately 37 km to 28 km between the Adriatic Plate and the Pannonian Fragment [Behm et al. 2007].

## 1.2 Objective of this thesis

---

The ALP 2002 and CELEBRATION 2000 experiments were carried out to investigate the crustal structure with a particular interest in the Moho discontinuity. In areas with high signal/noise ratio, however, not only the typical seismic arrivals such as the Pg- (diving wave through the crust), PmP- (Moho-reflection) and Pn-phases (refracted wave from the uppermost mantle) are obtained, but also significant reflective events from below the Moho, whose investigation poses the main task of this thesis. Those mantle reflections are abundant in certain regions and are most prominent on cross-section profiles. A very interesting feature is obtained at specific seismic sections where apparently two different reflective events can be recognized.

Observed reflections appear at offsets between 200 and 500 km and accumulate significantly in three regions: a) in the transition zone between the Eastern Alps, the Pannonian Basin and the Carpathians, b) in the Eastern Alps of Carinthia, c) in the Bohemian Massif in the central Czech Republic.

This thesis aims for the investigation of these reflective events from the upper mantle including an inversion for depth and shape by applying ray tracing techniques as well as travel time inversion. Both approaches will be presented here, their parameters and adjustments explained and the accuracies of both systems will be compared.

In the first step an appropriate starting model will be elaborated to get a first depth estimation which subsequently facilitates the application of ray tracing. 3-D ray tracing for simple models is applied to support travel time picking. Inversion of these travel time picks allows a more accurate determination of the reflector structure. It will be shown that the output of the inversion is significantly influenced by the chosen velocity models. Crustal velocities are quite well determined, whereas upper mantle velocities are rather poorly constrained. Thus, several upper mantle velocity distributions will be tested and their influence on the reflector depth will be shown.

## 2 Reflectors in the uppermost mantle

---

### 2.1 Petrophysical parameters of crust and mantle

---

Intensive seismological studies reveal a quite complex structural composition of crust and mantle with a strongly varying distribution of petrophysical parameters such as P- and S-wave velocities and density (see *Figure 2.1b* and *Figure 2.2*). *Figure 2.1a* shows a cross-section through the crust and the upper mantle with the appropriate geological subdivisions.

#### The crust

The crust can be divided into continental and oceanic crust, with depths of 30 - 50 km beneath the continents and 5-10 km beneath the oceans. The average crust density is 2700 kg/m<sup>3</sup> and the P-wave velocities range typically from 5 km/s at shallow depths to about 6.5 - 7 km/s at a depth of 30 - 50 km. Due to the complex composition of the crust, seismic velocities do not generally increase continuously with depth but sometimes decrease in zones with different geological settings.

Feldspar (K-feldspar, plagioclase) is the most abundant mineral in the crust, followed by quartz and hydrous minerals, such as micas and amphiboles [[www.gyff.tu-freiberg.de/geologie/geo\\_minerale.html](http://www.gyff.tu-freiberg.de/geologie/geo_minerale.html)].

The boundary between crust and mantle is defined by a sharp increase in P-wave velocity to about 8 km/s; this transition zone is usually called ‘Mohorovicic discontinuity’ or ‘**Moho**’.

#### The upper mantle

The uppermost mantle between the Moho and a depth of 80-120 km is rigid, with slightly increasing P- and S-wave velocities. This layer is sometimes called the ‘lid’. Together with the crust, the lid forms the lithosphere. An increase of P- and S-wave velocities by 3 - 4 % has been observed at around  $220 \pm 30$  km depth (*Figure 2.2*). However, this discontinuity, also known as ‘Lehmann discontinuity’, is not found everywhere [*Lowrie, 1997*].

Between the lid and this discontinuity, in a depth range of 100 - 200 km, body-wave velocity gradients are weakly negative. The layer is called the low-velocity layer (LVL) and is usually associated with the top of the asthenosphere. The decrease in seismic velocities is attributed to reduced rigidity in this layer.

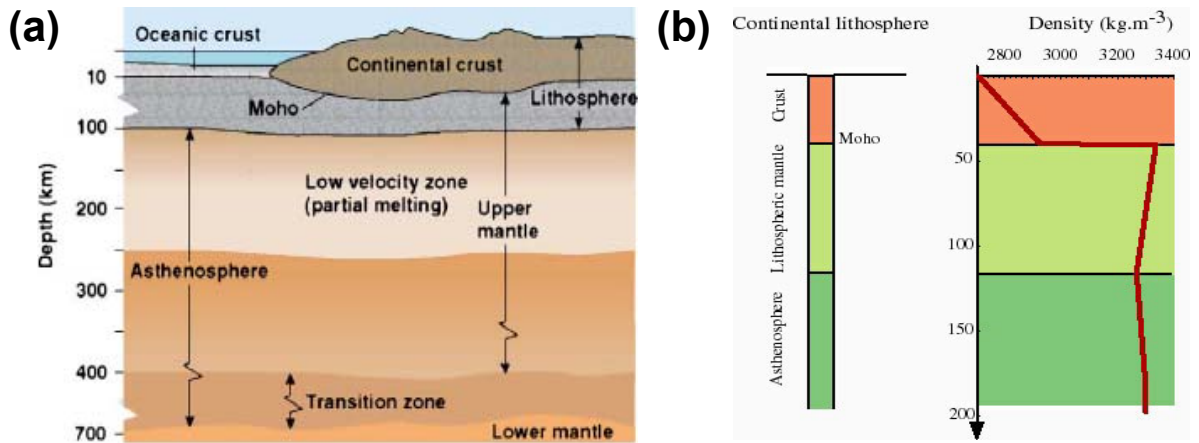


**Figure 2.1.** (a) Cross-section through crust and mantle with internal subdivisions; (b) density-depth profile: in the crust the density of rocks increases with depth due to an increase in pressure; in the lithospheric mantle (pale green), the density decreases with depth because of increasing temperature [www.geosci.usyd.edu.au/users/prey/Geol-1002/HTML.Lect1/sld015.htm].

Upper mantle P-wave velocities start around 8 km/s and increase slightly with depth until the low-velocity layer is reached (e.g. *Figure 2.2*). *Christensen & Mooney (1995)* investigated the petrophysical parameters of the lithosphere obtained from worldwide data and proposed an average P-wave velocity of 8.1 km/s and a density of 3350 kg/m<sup>3</sup> for the uppermost mantle. The composition of the upper mantle mainly comprises the rock types peridotite, dunite (olivine-rich peridotite) and eclogite. Eclogite typically results from high-pressure metamorphism of mafic igneous rock (typically basalt or gabbro) as it plunges into the mantle in a subduction zone.

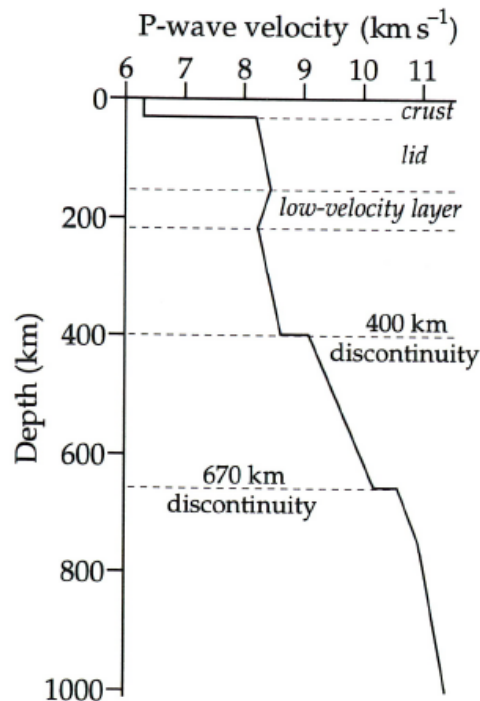


**Figure 2.2.** P-wave velocity – depth profile in the upper mantle beneath the Canadian shield [Lowrie, 1997].

## 2.2 Evidence for upper mantle reflectors

In 1975, as the first deep seismic profiling experiments took place, excitement arose among seismologists when reflections from the Moho could be obtained, allowing them to study the Moho structure in different geologically interesting places. However, on most profiles recorded around the world, no reflectors were found within the mantle, except at sites of recent continental collision (e.g. the Pyrenees) or active oceanic subduction zones (e.g. Vancouver Island) where probably crustal material diving into the mantle was imaged.

In recent years, the number of deep seismic experiments increased throughout the world, with the result that nearly every deep reflection program has reported some type of mantle structure (Figure 2.3). Reflection energy from the mantle lithosphere is observed in both near-normal incidence and wide-angle data.

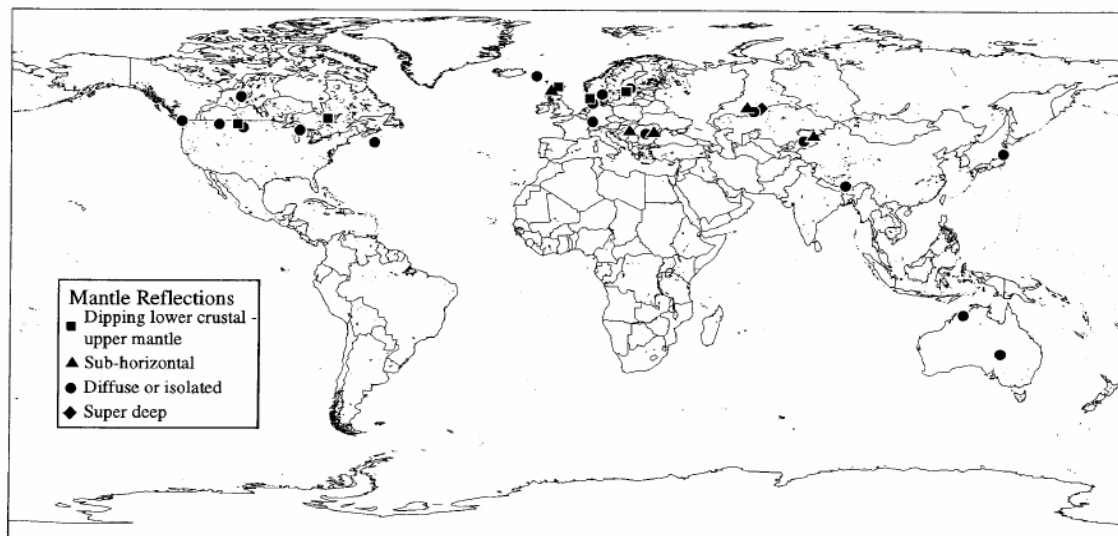


Figure 2.3. Location map indicating surveys reporting mantle reflections [Steer et al. 1998]

The first experiment to reveal significant mantle reflectors was in 1982 by the BIRPS group, off the north coast of Scotland [[www.earthscrust.org/earthscrust/science/startups/birps-su.html](http://www.earthscrust.org/earthscrust/science/startups/birps-su.html)]. In the following years research on the upper mantle was carried out by Lie et al. (1990), BABEL Working Group (1990), Posgay et al. (1990), Calvert et al. (1995), Alsdorf et al. (1996), Knapp et al. (1996), MONA LISA Working Group (1997b), Cook et al. (1998, 1999), DEKORP-BASIN Research Group (1999), ANCORP Working Group (1999) and Balling (2000). Despite these investigations in the lithosphere, little is yet known about the formation of mantle structures, why they are preserved, and how they relate to continental evolution.

## 2.3 Categories of mantle reflections (according to *D. Steer, J. Knapp and L. Brown, 1998*)

---

### 2.3.1 Dipping lower crustal to upper mantle reflections

The Flannan and W-features, two distinctive sub-crustal reflectors, are probably the best studied mantle reflections and were first observed on the DRUM profile in 1984, offshore north-west of Scotland. The results of this project, carried out by the BIRPS group, showed for the first time the structural complexity and heterogeneity in the sub-crustal mantle and led to a new understanding regarding the role of the mantle in lithospheric evolution at that time.

The Flannan reflector runs from about 20 km depth within the lower crust down to at least 80 km total depth in the sub-crustal lithosphere, dipping at about 30° to the east. It is interpreted as a fault that had taken up corresponding tectonic movement in the mantle. The W-feature, as seen in *Figure 2.4*, is sub-parallel to the Moho at a depth of 45 km east of the 'Flannan', and is interpreted as part of the crustal shortening caused during the suturing event.

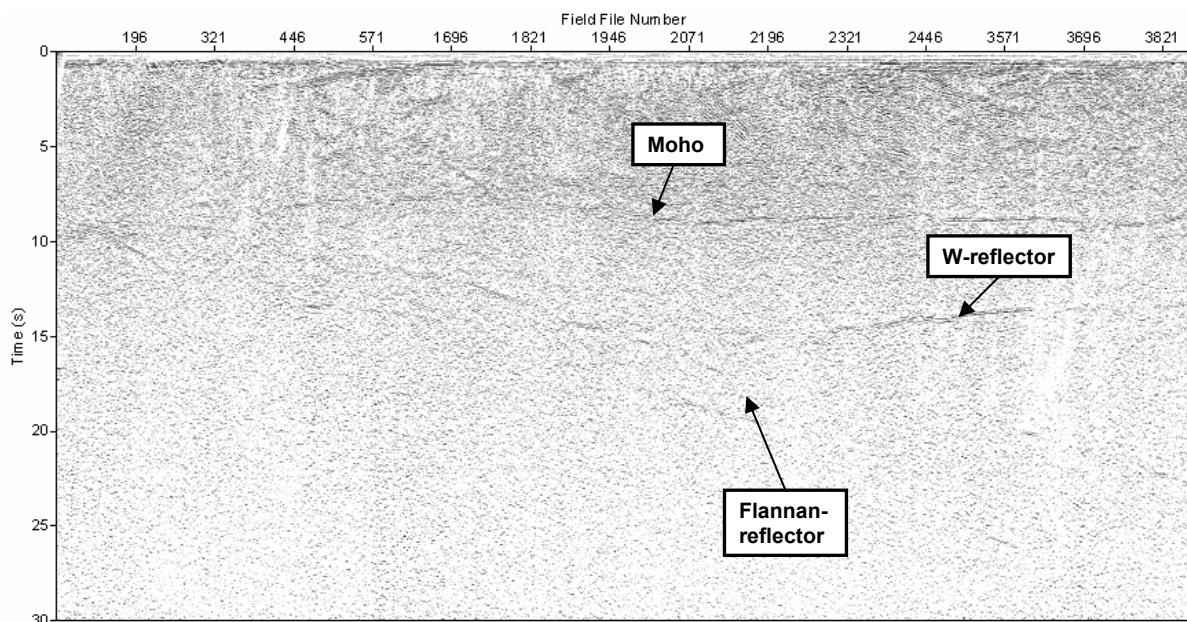


**Figure 2.4.** Cross-section of the DRUM-profile including the prominent W- and Flannan reflectors

Similar reflective characteristics are observed in data acquired from the Bay of Bothnia between Sweden and Finland [*BABEL Working Group, 1990*], with the reflective event starting in the lower crust and dipping 20 - 25° to a depth of 70 km. In the Superior Province of Canada data show lower crustal to upper mantle reflections that dip 25 - 30° to a depth of at least 70 km [*Calvert et al. 1995*].

### 2.3.2 Diffuse or isolated mantle reflections

Diffusely distributed and isolated reflectors are obtained in a number of experiments including the INDEPTH data beneath the Himalayan region and the Trans-Hudson Orogen in North Dakota. Isolated mantle reflections are rather difficult to interpret, with proposed theories ranging from mafic layering (e.g. Lonesome Lake Complex) to upper mantle intrusions (e.g. Mid-Continent Rift).

### 2.3.3 Sub-horizontal mantle reflections

This category of mantle reflections is characterized by laterally continuous, distinct, sub-horizontal events, sometimes appearing as doublet separated roughly by 2 seconds two-way travel time or 4 - 5 km. Data showing this kind of reflection have been acquired in the Skagerrak between Norway and Denmark, during the MONA LISA experiment in the southeastern North Sea, beneath the Pannonian Basin of Hungary, and in the Caledonides and Urals.

Interpretation attempts vary hugely – Posgay suggests that mantle reflectors in the Pannonian Basin may represent structure in the asthenosphere; *Snyder (1991)* proposes the reflector in north-west Scotland either to be a 'Moho relict' or a mafic or ultra-mafic intrusion.

Sub-horizontal reflections have been observed at even greater depths up to 100 km. During the URSEIS project in the Ural Mountains of central Russia, reflectors have been found at a depth of 80 - 100 km. Later data analysis showed a coincidence of the reflector with velocity anomalies at that depth.

### 2.3.4 Super-deep mantle reflections

The URSEIS experiment indicates not only a reflective horizon at a depth of 80 - 100 km, but also reveals two distinctive reflectors in a far deeper portion of the lithosphere, at depths of 135 - 165 km and 225 km. These reflectors are laterally continuous over a distance of 75 km for the reflector at a depth of 135 - 165 km and about 20 km for the second reflector.

Interpretation was mainly done by *Knapp et al. (1996)*, who advanced the hypothesis that these reflections may form the boundary between the lithosphere and the asthenosphere. If they do correspond with the base of the lithosphere, compositional layering or mafic intrusions from the asthenosphere in the mantle lithosphere could produce strong reflections.

## 2.4 Geological models for upper mantle reflectivity

---

The complexity of mantle reflections – from shallow to ultra-deep and from dipping to horizontal reflections – obtained from numerous deep seismic reflection data around the world, makes it difficult to interpret them according to a single geological model. Currently, a couple of models shown in *Figure 2.5* are considered to explain reflectivity. However, two models – relict subduction zones and mantle shear zones – are favoured by many geoscientists. Seismic anisotropy and fluids may also account for seismic reflections in the mantle.

### 2.4.1 Relict subduction and collision

At the subduction of oceanic crust to a depth greater than circa 40 km a transformation from basalt/gabbro to eclogite takes place. This transformation does not occur instantaneously, but needs some additional conditions. Laboratory experiments and field observations show that water plays a key role and stimulates transformation.

Since the density of eclogite is larger than upper mantle peridotite, an increase in density takes place during transformation. In this case, densities vary between  $3470 \text{ kg/m}^3$  and  $3610 \text{ kg/m}^3$  [Anderson, 1989] and  $3480 \pm 70 \text{ kg/m}^3$  [Christensen & Mooney, 1995]. P-wave velocities for eclogites are defined within a broad range –  $7.9 \text{ km/s}$  [Christensen & Mooney, 1995],  $8.2 - 8.6 \text{ km/s}$  [Anderson, 1989] and  $7.7 - 8.6 \text{ km/s}$  [Rudnick & Fountain, 1995].

Studies of mantle reflectors north of Scotland (W- and Flannan reflectors) resulted in the W-reflector to be  $3 - 10 \text{ km}$  thick with a P-wave velocity of  $8.5 \pm 0.1 \text{ km/s}$  and a surrounding mantle P-wave velocity of  $8.2 \text{ km/s}$ . These observations lead to the conclusion that the Flannan and W-reflectors represent reflection events from the tops of slabs of eclogite and therefore favours the subduction hypothesis for these reflectors.

Interpretation in terms of ancient subduction and collision zones has also been advocated for dipping upper mantle reflectors observed in BABEL data from the Baltic shield [BABEL Working group, 1990], MONA LISA data from the North Sea [MONA LISA Working Group, 1997b] and the LITHOPROBE data in the western Canadian shield [Cook et al., 1998, 1999], where the reflectors are interpreted to represent  $1.9 - 1.8 \text{ Gyr}$  old subduction structures.

### 2.4.2 Shear zones

Reflectivity generated by crustal faults and shear zones, both in compressional and extensional processes, has been investigated by Meissner (1996), and is now widely accepted. Studies combining petrophysical measurements, field studies and synthetic reflection modelling have shown that the seismic impedance contrast related to shear zones seems to correspond well with real data.



Shear zones in the upper mantle are unfortunately not well documented, however, field data from exposed upper mantle peridotites in the Alps and the north Pyrenean [Visser *et al.*, 1995, 1997] demonstrate the existence of localized shear zones. Observed grain size reduction and mineral reaction point towards a reduction in P-wave velocity and density and consequently supports the generation of reflectivity.

### 2.4.3 Anisotropy

Anisotropy may also cause reflectivity. Olivine, which is expected to constitute about two thirds of upper mantle minerals, is highly anisotropic. Parts of the upper mantle may develop anisotropy when oriented along a stress. Velocity anisotropy larger than 5 % is uncommon – Dunite, consisting mainly of olivine, shows a P-wave velocity anisotropy of  $8.1 \text{ km/s} \pm 3.9 \%$  [Christensen & Mooney, 1995].

Research by Warner & McGary (1987) on anisotropy in upper mantle peridotite leads to a reflection coefficient of less than 0.04 – in comparison to reflectors on BIRPS profiles which show a reflection coefficient of 0.1 – which is too little to produce significant reflection energy. However, localized deformation in the upper mantle may contribute to the generation of significant reflectivity.

### 2.4.4 Fluids

The effect of fluids (zero shear modulus), even in very small amounts, on seismic waves is not to be neglected as it may cause a significant contrast in reflectivity to the surrounding solid rocks. In young tectonic processes as in subducting events, fluids may be present and influence seismic properties significantly, whereas in old tectonic features fluids may have already migrated away and cause no impact on reflectivity.

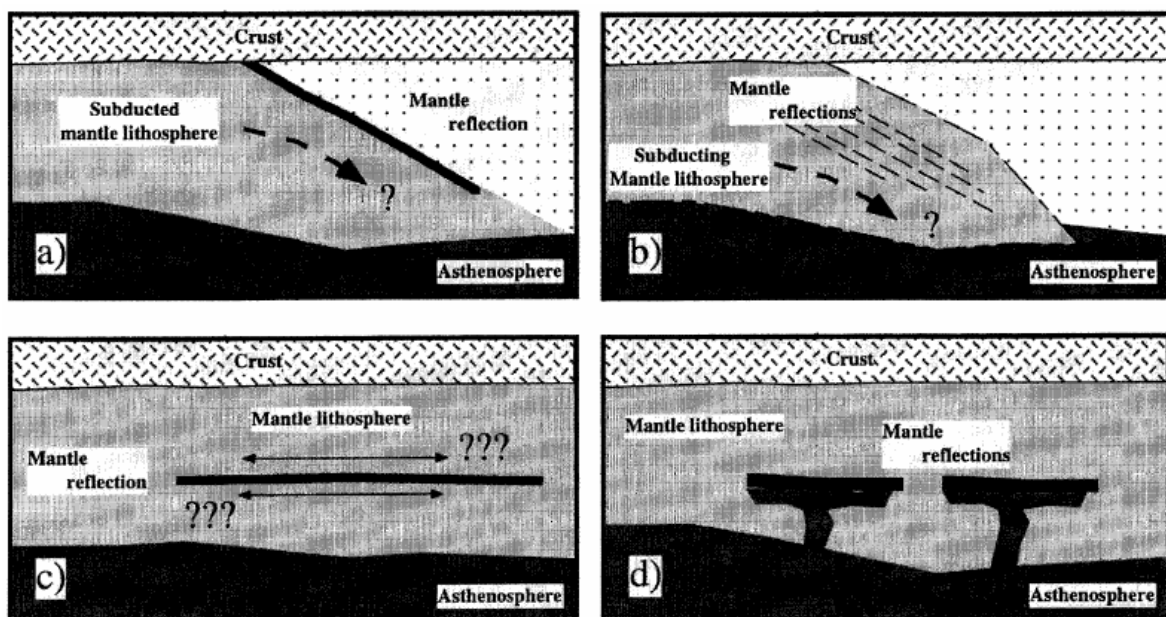


Figure 2.5. Mantle reflections are thought to be caused by: a) remnants of subduction, b) distributed shearing in the upper mantle, c) localized shearing in the upper mantle, or d) mafic intrusions to the upper mantle [Steer *et al.* 1998]

## 3 Theory of travel time modelling and inversion

---

### 3.1 Eikonal equation [Yilmaz, 1987]

---

The Eikonal equation represents the high-frequency solution to the scalar wave equation and allows to compute travel times and ray paths. Its solution represents wavefronts of constant phase. At low frequencies body waves do not decouple and the Eikonal equation is then, in general, not valid.

In order to derive the Eikonal equation we need a solution to the **3D – scalar wave equation**

$$\frac{\partial^2 P}{\partial x^2} + \frac{\partial^2 P}{\partial y^2} + \frac{\partial^2 P}{\partial z^2} = \frac{1}{v^2(x, y, z)} \frac{\partial^2 P}{\partial t^2} \quad (\text{E.1})$$

where  $P(x, y, z, t)$  is a wavefield (e.g. pressure field, displacement field,...) that propagates with a velocity  $v$ .

One solution to this equation is

$$P(x, y, z, t) = P_0 \exp(-i\omega t + ik_x x + ik_y y + ik_z z), \quad (\text{E.2})$$

which can be interpreted as a compressional plane wave  $P(x, y, z, t)$  in 3D-Cartesian coordinates  $(x, y, z)$  with  $P_0$  as its amplitude and  $t$  its travel time. Substitution of equation E.2 into E.1 yields the **dispersion relation** of the scalar wave equation

$$k_x^2 + k_y^2 + k_z^2 = \frac{\omega^2}{v^2} \quad (\text{E.3})$$

with  $v$  as the propagation velocity of the compressional plane wave.

Rewriting the phase term  $[\omega t - (k_x x + k_y y + k_z z)]$  in the plane wave solution of equation E.2 results in

$$P(x, y, z, t) = P_0 \exp\left\{-i\omega\left[t - \left(\frac{k_x}{\omega}x + \frac{k_y}{\omega}y + \frac{k_z}{\omega}z\right)\right]\right\} \quad (\text{E.4})$$

with  $\frac{k_x}{\omega}x + \frac{k_y}{\omega}y + \frac{k_z}{\omega}z = T(x, y, z)$  defined as a 3D-travel time surface.

Thus, using  $T(x, y, z)$ , equation E.2 can be rewritten in the following manner

$$P(x, y, z, t) = P_0 \exp\{-i\omega[t - T(x, y, z)]\}, \quad (\text{E.5})$$

In the next step, E.5 will be substituted into the scalar wave equation E.1. After a split into real and imaginary parts, E.1 reads

$$\omega^2 \left[ \left( \frac{\partial T}{\partial x} \right)^2 + \left( \frac{\partial T}{\partial y} \right)^2 + \left( \frac{\partial T}{\partial z} \right)^2 \right] - i\omega \left( \frac{\partial^2 T}{\partial x^2} + \frac{\partial^2 T}{\partial y^2} + \frac{\partial^2 T}{\partial z^2} \right) = \frac{\omega^2}{v^2(x, y, z)} \quad (\text{E.6})$$

The imaginary part has to go, since the term on the right-hand side is real. Dividing the remaining equation by  $\omega^2$  leads to an expression that is commonly known as the **Eikonal equation**.

$$\left( \frac{\partial T}{\partial x} \right)^2 + \left( \frac{\partial T}{\partial y} \right)^2 + \left( \frac{\partial T}{\partial z} \right)^2 = \frac{1}{v^2(x, y, z)} \quad (\text{E.7})$$

The function  $T(x, y, z)$  has units of time and simply represents the time required by the wavefront to reach a point  $(x, y, z)$  from some reference location  $(x_0, y_0, z_0)$  in a medium with velocity  $v(x, y, z)$ . One solution to the Eikonal equation is  $T(x, y, z) = \text{constant}$ , which defines a wavefront at an instant of time. The gradient of  $T(x, y, z)$  represents the raypath, which is perpendicular to the wavefront.

As mentioned earlier, the Eikonal equation represents just an approximation to the scalar wave equation. We want to examine why it is restricted to higher frequencies only and, thus, which conditions need to be fulfilled to apply this equation properly.

Let us consider the same plane wave as in equation E.5. This time, seismic wave attenuation through geometrical spreading, scattering etc. will be taken into account. The amplitude  $P_0$  then becomes a function of  $(x, y, z)$ .

$$P(x, y, z, t) = P_0(x, y, z) \exp\{-i\omega[t - T(x, y, z)]\} \quad (\text{E.8})$$

Just as before, E.8 will be substituted into E.1. This time, the partial derivatives need to be applied to  $P_0$  as well.

The resulting real part is then given by

$$\left[ \left( \frac{\partial T}{\partial x} \right)^2 + \left( \frac{\partial T}{\partial y} \right)^2 + \left( \frac{\partial T}{\partial z} \right)^2 \right] - \frac{1}{\omega^2 P_0} \left( \frac{\partial^2 P_0}{\partial x^2} + \frac{\partial^2 P_0}{\partial y^2} + \frac{\partial^2 P_0}{\partial z^2} \right) = \frac{1}{v^2} \quad (\text{E.9})$$

To reduce this equation to the Eikonal equation, the second term on the left-hand side has to go. This is done by assuming high frequencies, which results in  $1/\omega$  converging to zero. Since  $\lambda = 2\pi v/\omega$ , where  $\lambda$  is the wavelength, the high-frequency assumption is equivalent to small wavelengths.

In practical applications, it is interesting for which wavelengths the Eikonal equation can be used as an approximation. It is valid as long as the velocity gradient is much less than the

frequency  $v/\lambda$ . Thus, it can not be used across a layer boundary with a sharp velocity contrast or in layers with velocity variations that occur to an extent much lower than the wavelength.

Summing up, the Eikonal equation can be used as an approximation as long as velocities do not vary rapidly.

## 3.2 Methods based on ray tracing

---

### 3.2.1 Ray tracing equations [Cerveny, 1987]

The solution to the Eikonal equation is a function that defines the travel time of a wave at each point. It can be descriptively explained as a wavefront that is perpendicularly cut by a trajectory (or ray).

Let us assume an earth model with assigned velocities, an arbitrary starting point at the surface for a ray to propagate and an initial direction. The ray, emanating from an initial location with known coordinates, is now traced along its path through the model. In practical applications, we are interested in the travel time the ray needs to get to a specific location in the model or on the surface, the ray coordinates at specific points and the direction of the ray at these points.

In order to derive these parameters, we specify the ray by the parametric equation

$$\mathbf{x}(s) = [x(s), y(s), z(s)] \quad (\text{E.10})$$

where  $s$  is the arclength along the ray, with  $s = 0$  indicating the reference point of the ray.

Since the ray is always perpendicular to a wavefront, it is always parallel to

$\nabla T = \left[ \frac{\partial T}{\partial x}, \frac{\partial T}{\partial y}, \frac{\partial T}{\partial z} \right]$ . We will now introduce a new vector  $\mathbf{p}$  which equals  $\nabla T$  and call it

**slowness vector.**

$$\mathbf{p} = \nabla T \quad (\text{E.11})$$

Now we let the ray advance for a short distance  $ds$  along the ray path yielding the following equation

$$d\mathbf{x} = \frac{\nabla T}{|\nabla T|} ds = \mathbf{p} \cdot \frac{ds}{|\nabla T|} \quad (\text{E.12})$$

where  $\frac{\nabla T}{|\nabla T|}$  is the unit vector parallel to  $ds$  (see *Figure 3.1*).

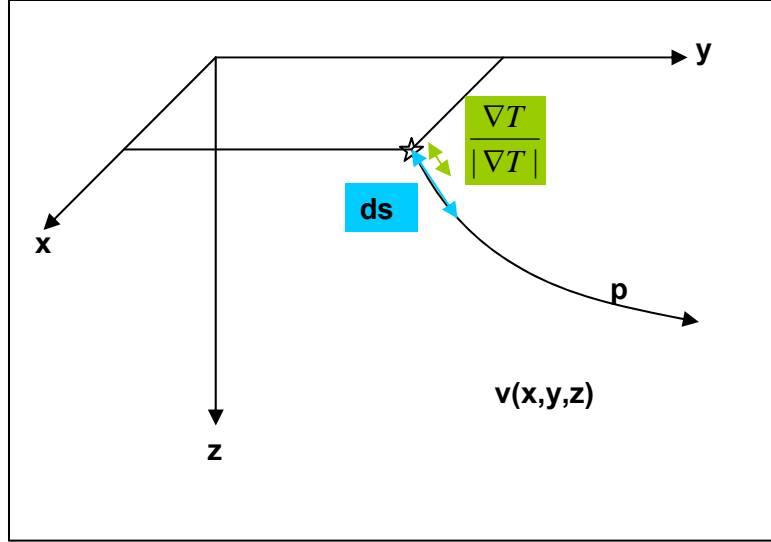


**Figure 3.1.** Sketch illustrating the quantities ( $ds$ ,  $\mathbf{p}$ , unit vector) which are used in the derivation of the ray tracing equations.

Substitution of the Eikonal equation  $|\nabla T| = \frac{1}{v(x, y, z)}$  into equation E.12 produces the

### 1. Ray Tracing Equation

$$\mathbf{p} = \frac{1}{v(x, y, z)} \frac{d\mathbf{x}}{ds} \quad (\text{E.13})$$

Starting from an initial point, this equation allows to determine a new point along the ray path. At each point a new ray direction is needed, consequently, the differential equation  $d\mathbf{p}/ds$  needs to be solved.

$d\mathbf{p}/ds$  can be rewritten in the following manner when using the index notation and applying the rule of changing indices:

$$\begin{aligned} \frac{dp_i}{ds} &= \frac{\partial p_i}{\partial x_j} \frac{dx_j}{ds} = v \cdot p_j \frac{\partial}{\partial x_j} \left( \frac{\partial T}{\partial x_i} \right) = v \cdot p_j \frac{\partial}{\partial x_i} \left( \frac{\partial T}{\partial x_j} \right) = v \cdot p_j \frac{\partial p_j}{\partial x_i} \\ &= \frac{1}{2} v \frac{\partial}{\partial x_i} (p_j \cdot p_j) = \frac{1}{2} v \frac{\partial}{\partial x_i} \left( \frac{1}{v^2} \right) = \frac{\partial}{\partial x_i} \left( \frac{1}{v} \right) \end{aligned}$$

This is called the **2. Ray Tracing Equation**

$$\frac{d\mathbf{p}}{ds} = \frac{\partial}{\partial \mathbf{x}} \left( \frac{1}{v(x, y, z)} \right) \quad (\text{E.14})$$

Information about the travel time along the path is simply obtained through the slowness

$$\frac{dT}{ds} = \frac{1}{v(x, y, z)} \quad (\text{E.15})$$

In some situations it might be advantageous to use some other independent variable  $w$  along the ray rather than using  $s$ . Then the ray is described by

$$\mathbf{x}(w) = [x(w), y(w), z(w)] \quad (\text{E.16})$$

The variable  $w$  can now be chosen in many ways, for example, as one of the three Cartesian coordinates. However, the problem that occurs when using Cartesian coordinates is the non-monotonic behaviour along the ray. If we choose  $x_3$  corresponding to the depth as our variable  $w$ , the ray must then be divided into a down- and an up-going segment. Some difficulties also occur at the turning point of the ray. Therefore, it is more useful to choose a monotonic variable  $w$ .

Instead of  $s$ , the arc length, the travel time  $T$  may be used as the variable. With  $dT = \frac{1}{v} ds$  equations E.13 and E.14 can be rewritten as

$$\frac{d\mathbf{x}}{dT} = v^2 \mathbf{p} \quad (\text{E.17})$$

$$\frac{d\mathbf{p}}{dT} = v \frac{\partial}{\partial \mathbf{x}} \frac{1}{v} \quad (\text{E.18})$$

The ray tracing equations can be written more generally in terms of  $w$ , with  $w$  given as

$$w(T) = w(T_0) + \int_{T_0}^T v^n dT \quad (\text{E.19})$$

leading to the following equations

$$\frac{d\mathbf{x}}{dw} = v^{2-n} \mathbf{p} \quad (\text{E.20})$$

$$\frac{d\mathbf{p}}{dw} = -v^{-1-n} \frac{\partial v}{\partial \mathbf{x}} = \frac{1}{n} \frac{\partial}{\partial \mathbf{x}} (v^{-n}) \quad (\text{E.21})$$

$$\frac{dT}{dw} = v^{-n} \quad (\text{E.22})$$

The general equations of E.20 - E.22 are reduced to equations E.17 and E.18 if we set  $n=0$ , the variable  $w$  then equals then the travel time  $T$ . In case of  $n=1$ , we have  $w=s$ , the arc length, and equations E.20 - E.22 transform to E.13 - E.15.

If we wish to evaluate not only rays, but also wavefronts, it may be useful to choose the travel time  $T$  as the variable along the ray ( $n=0$ ). Then the wavefronts are obtained automatically, as a by-product of the ray tracing. The use of other variables along the ray, for example the arc length  $s$ , makes the wavefront evaluation more complicated requiring an additional integration of equation E.15 or at least an interpolation. In the analytical and cell ray tracing, a very suitable form of the ray tracing system is obtained for  $n=2$ . Therefore, we shall introduce a special symbol  $w=\sigma$  for the variable along the ray:

$$\sigma(T) = \sigma(T_0) + \int_{T_0}^T v^2 dT \quad (\text{E.23})$$

Then, the ray tracing equations read

$$\frac{d\mathbf{x}}{d\sigma} = \mathbf{p} \quad (\text{E.24})$$

$$\frac{d\mathbf{p}}{d\sigma} = \frac{1}{2} \frac{\partial}{\partial \mathbf{x}} \frac{1}{v^2} \quad (\text{E.25})$$

with 
$$\frac{dT}{d\sigma} = \frac{1}{v^2} \quad (\text{E.26})$$

A remarkable feature in equation E.25 and E.26 is the **quadratic slowness  $1/v^2$** , which is more useful in certain ray tracing applications than the velocity  $v$  or the slowness  $1/v$ . This is due to the fact that equation E.25 only contains the first partial derivatives of  $1/v^2$ , not the quadratic slowness  $1/v^2$  itself, and thus can be handled easier in analytical ray tracing.

In order to solve the ray tracing system equations and the equations for the travel time, **initial conditions** must be given. These are:

- coordinates of the initial point  $P$ , which also defines the initial  $\mathbf{x}=\mathbf{x}_0$
- initial direction  $\mathbf{p}=\mathbf{p}_0$
- initial travel time  $T=T_0$

The three components of the initial slowness vector  $\mathbf{p}_0$  have to satisfy the Eikonal equation at the initial location  $P$ ,

$$\mathbf{p}^2 = \frac{1}{v_0^2} \quad (\text{E.27})$$

with  $v_0$  as the initial velocity.

Given the initial direction of the ray at P by two take-off angles  $\delta_0$ , which represents the declination, and  $\varphi_0$ , the azimuth, the components of the initial slowness vector can be expressed in the following way:

$$\begin{aligned} p_x &= \frac{1}{v_0} \sin \delta_0 \cos \varphi_0 \\ p_y &= \frac{1}{v_0} \sin \delta_0 \sin \varphi_0 \\ p_z &= \frac{1}{v_0} \cos \delta_0 \end{aligned} \tag{E.28}$$

As soon as the Eikonal equation is satisfied at the initial point, it is satisfied along the whole ray.

The initial values for  $\mathbf{x}$  and  $\mathbf{p}$  allow us to compute a new point along the ray path by applying the 1<sup>st</sup> ray tracing equation. Through the 2<sup>nd</sup> ray tracing equation we get the new direction at that specific point, in other words, a new slowness vector  $\mathbf{p}$ . That again is used in the first equation to determine the next ray point.

The above mentioned differential equations can be solved either analytically or numerically. The simplest and fastest way to solve the ray tracing equations is based on their **analytic solution**. Its application, however, is limited to simple velocity functions only (e.g. constant velocity, constant gradient of velocity:  $v(z)=v_0 + k.z, \dots$ ) – a criterion that is unfortunately never met in real models. Nonetheless, a solution can be found to this kind of problem. The whole medium, which is defined by a complicated velocity distribution, will be divided into suitable cells, in which the velocity can be approximated in a simpler way that permits analytic solutions. The ray in the whole model is then obtained as a chain of analytically computed segments.

In some cases, though, the direct **numerical solution** of the ray equations is more suitable. Numerous numerical techniques are available including the popular **Runge-Kutta method** and the **method of the predictor and corrector**.

In general, two kinds of ray tracing need to be distinguished – **initial-value ray tracing** and **two-point ray tracing**.



### 3.2.2 Initial-value ray tracing [Cerveny, 1987]

Initial-value ray tracing describes the tracing of rays through a medium by solving the ray tracing equations with given initial conditions (initial point/ initial direction) (see *Figure 3.2*).

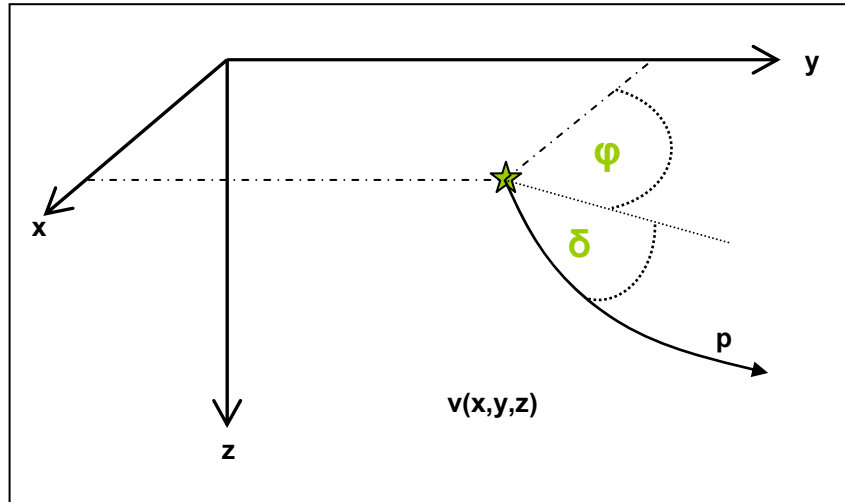


**Figure 3.2.** In the initial-value application, the ray emanates at an initial location  $(x_0, y_0, z_0)$  with its direction defined by the azimuth  $\varphi$  and declination  $\delta$ .

Many procedures have been elaborated in order to solve the ray tracing equations for the initial value problem. To pick a proper procedure depends on many factors such as required accuracy, practical purpose, numerical efficiency of computations and the completeness of ray properties (should travel times be computed alone or together with ray amplitudes).

### 3.2.3 Two-point ray tracing [Rawlinson et al. 2003]

In the initial-value ray tracing the ray is specified by its two take-off angles  $\delta_0$ , the declination, and  $\varphi_0$ , the azimuth, and then propagates through the medium until it reaches any point at a defined surface. Two-point ray tracing, in contrary, involves solving the boundary value problem. That means, the source point and the receiver locations are fixed and the two take-off angles are now varied in a way so that the ray terminates at a specified receiver location (see *Figure 3.3*).

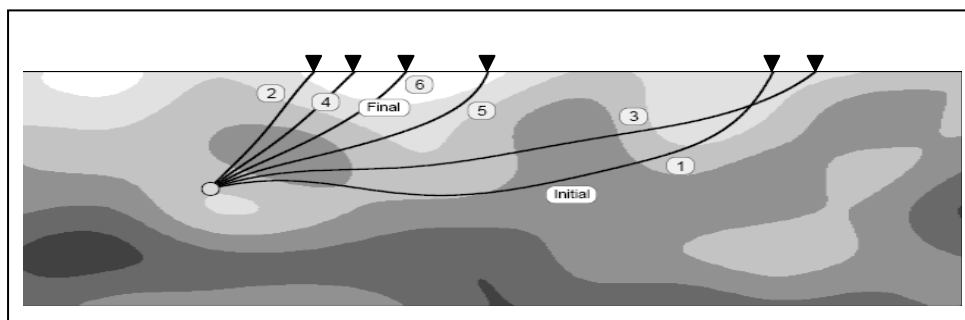


**Figure 3.3.** In the two-point ray tracing technique the angle of radiation is varied until the ray path terminates at a specified receiver [Rawlinson et al. 2003].

Since the ray end point  $(x_e, y_e)$  should coincide with the receiver location  $(X_r, Y_r)$ , the boundary value problem aims to find  $\delta_0$  and  $\varphi_0$  which solve the two non-linear simultaneous equations

$$x_e(\delta_0, \varphi_0) = X_r \quad (\text{E.29})$$

$$y_e(\delta_0, \varphi_0) = Y_r \quad (\text{E.30})$$

Given that  $(x_e, y_e)$  cannot be expressed explicitly as a function of  $(\delta_0, \varphi_0)$  for most velocity fields, it is usually the case that the boundary value problem is posed as an optimisation problem, with the misfit function to be minimised expressed as some measure of the distance between the ray end point and its intended target.

Since the optimisation problem is non-linear, a range of iterative non-linear and fully non-linear schemes can be applied. A common iterative non-linear scheme is **Newton's method**, which amounts to iterative application of the following system of equations:

$$\underbrace{\begin{pmatrix} \frac{\partial x_e}{\partial \delta_0} & \frac{\partial x_e}{\partial \varphi_0} \\ \frac{\partial y_e}{\partial \delta_0} & \frac{\partial y_e}{\partial \varphi_0} \end{pmatrix}}_{\text{derivative-matrix}} \begin{pmatrix} \delta_0^{n+1} - \delta_0^n \\ \varphi_0^{n+1} - \varphi_0^n \end{pmatrix} = \begin{pmatrix} X_r - x_e(\delta_0^n, \varphi_0^n) \\ Y_r - y_e(\delta_0^n, \varphi_0^n) \end{pmatrix} \quad (\text{E.31})$$

Thus, given some starting initial trajectory  $\delta_0^0, \varphi_0^0$ , solution of this equation provides an updated initial trajectory  $\delta_0^1, \varphi_0^1$ , and the process is repeated until an appropriate tolerance criterion is met.

The success of this scheme depends largely on two factors: (1) accurate calculation of the partial derivative matrix, and (2) obtaining an initial guess ray that will converge to the correct minimum under the assumption of local linearity. However, both of these requirements can be difficult to satisfy, particularly in complex media. One way of obtaining an accurate initial guess ray is to shoot a broad fan of rays in the general direction of the receiver array, and then (if necessary) shooting out increasingly targeted clusters of rays towards zones containing receivers until a suitably accurate initial ray is obtained.

### 3.3 Finite difference method

---

Rather than tracing rays from point to point through a medium to determine the travel time from source to receiver, an alternative is to track the propagation path of the entire wavefront. The travel time to any point in the medium can be found using this approach. In order to calculate the first-arrival travel time field, solutions of the Eikonal equation on a regular grid have to be found, which is most conveniently achieved when using the finite difference method.

Wavefront tracking approaches do not explicitly find ray paths. However, in the inversion of reflection times a way of locating ray paths is required. One way of doing this is to start at the receiver and follow the gradient of the travel time field back through the computed travel time field to the source. The gradient will always be perpendicular to the first arrival wavefront and will therefore determine the first-arrival ray path. In practice, this is done on a cell-by-cell basis using the average travel time gradient within each cell. The whole path from receiver to source will be described by piecewise linear segments.

*Vidale (1988)* proposed a finite difference scheme that involves progressively integrating the travel times along an expanding square in 2-D. However, this method does not directly involve the tracking of wavefronts to determine the travel time field, but it represents a precursor of schemes that do. The Eikonal equation (E.7) in 2-D is given by:

$$\left(\frac{\partial T}{\partial x}\right)^2 + \left(\frac{\partial T}{\partial z}\right)^2 = [s(x, z)]^2 \quad (\text{E.32})$$

where  $s(x, z)$  is the slowness field and  $T(x, z)$  is the travel time of a propagating wave. Vidale's method is based on a velocity distribution that is given on the corners of a square grid. Consider the grid points surrounding some local source point A in *Figure 3.4a*. If the travel time to point A is  $T_0$  then the travel time to the points  $B_i$  is determined by the arithmetic mean of the slowness at these points:

$$T_{B_i} = T_0 + \frac{h}{2}(s_{B_i} + s_A) \quad (\text{E.33})$$

where  $h$  is the node separation and  $s_{B_i}$  and  $s_A$  are the slowness at the nodes  $B_i$  and A respectively.

In the next step the travel time to the corner points  $T_{C_i}$  needs to be found. This can be achieved when the known travel times A ( $T_0$ ), B<sub>1</sub> ( $T_1$ ) and B<sub>2</sub> ( $T_2$ ) in *Figure 1a* are used. Point C<sub>1</sub> ( $T_3$ ) can then be determined by applying the Eikonal equation of E.32, with its two differential terms approximated with finite differences in the following way:

$$\begin{aligned} \frac{\partial T}{\partial x} &= \frac{T_1 - T_0}{h} \\ \frac{\partial T}{\partial x} &= \frac{T_3 - T_2}{h} \end{aligned} \Rightarrow \text{summing up and taking the arithmetic mean} \Rightarrow \frac{\partial T}{\partial x} = \frac{1}{2h}(T_1 + T_3 - T_0 - T_2)$$

(E.34)

$$\begin{aligned} \frac{\partial T}{\partial z} &= \frac{T_2 - T_0}{h} \\ \frac{\partial T}{\partial z} &= \frac{T_3 - T_1}{h} \end{aligned} \Rightarrow \text{summing up and taking the arithmetic mean} \Rightarrow \frac{\partial T}{\partial z} = \frac{1}{2h}(T_2 + T_3 - T_0 - T_1)$$

(E.35)

Subsequent substitution of E.34 and E.35 into E.32 yields

$$\frac{(T_1 + T_3 - T_0 - T_2)^2}{h^2} + \frac{(T_2 + T_3 - T_0 - T_1)^2}{h^2} = 4\bar{s}^2$$

and solving the equation for  $T_3$

$$T_3 = T_0 + \sqrt{2(h\bar{s})^2 - (T_2 - T_1)^2}$$

(E.36)

where  $\bar{s}$  is the average slowness of all four points under consideration.

This approach of travel time calculation is only valid for planar wavefronts. Vidale defined a solution for locally circular wavefronts as well (e.g. in the source neighbourhood).

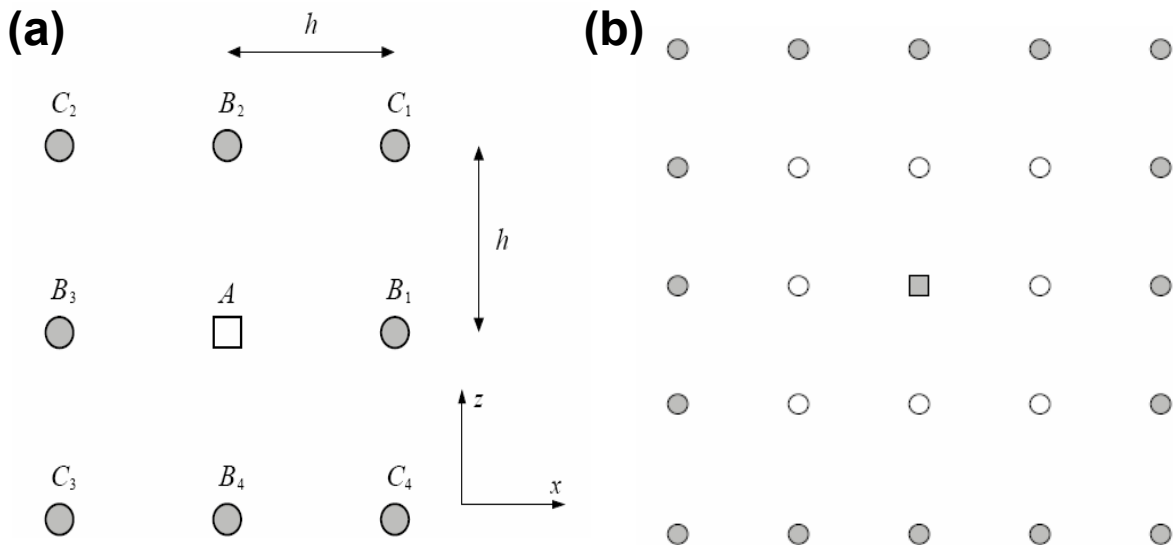


**Figure 3.4.** a) Method used by Vidale (1988) to find the first-arrival travel time field for a continuous velocity medium. b) The expanding square method for travel time determination. Travel times to the filled circles are determined from the open circles. The filled square represents the source [Rawlinson et al. 2003]

The travel times for all the other  $C_i$  can be derived in the same way. The next step involves enlarging the square around the source point as seen in *Figure 4b* and travel time determination for the next set of grid points. However, solving for the travel time to node points cannot be done in an arbitrary order as another condition has to be fulfilled, *Fermat's principle*. That means the travel time has to be an extremum, in our case the shortest travel time to each new node has to be taken. Only these times will be valid seismic travel times. Vidale elaborated such a scheme for minimum travel times and extended the whole method presented here to 3-D.

At the application of the expanding square method problems may occur with the geometry of the travel time field, which does not always resemble the shape of the first arrival wavefront. In areas with large velocity contrast, the computed travel times may not represent first-arrivals (*Figure 3.5*). *Qin et al. (1992)* improved this scheme by introducing an expanding geometry that closely resembles the true shape of the wavefront.

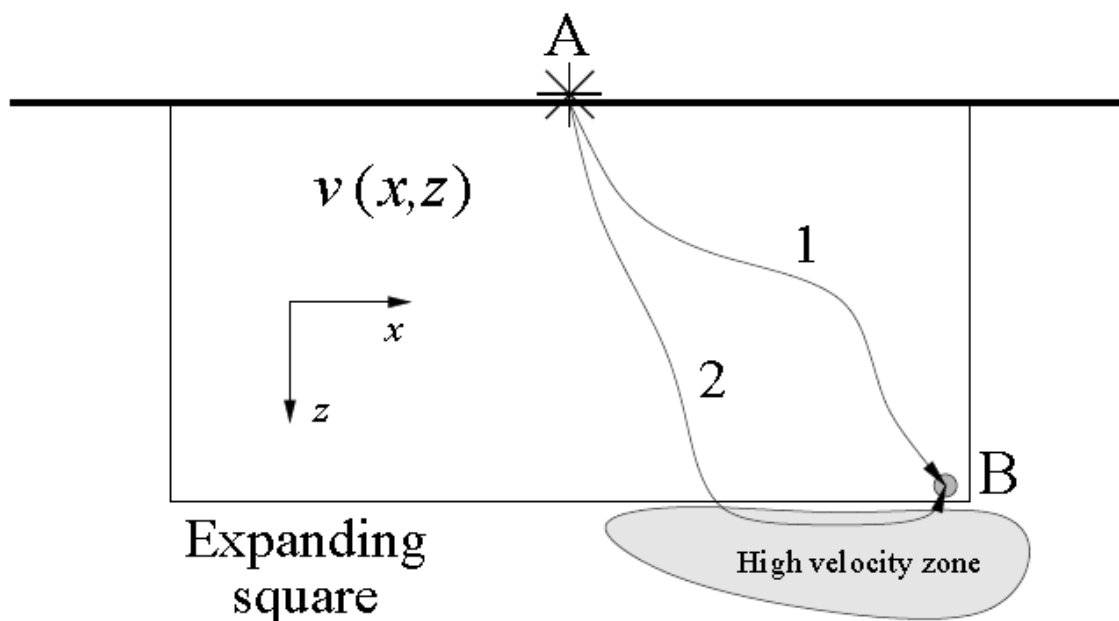


**Figure 3.5.** Schematic illustration showing how the expanding square method can fail . The travel time along path 1 is determined by the expanding square but path 2 has a shorter travel time due to the high velocity zone [Rawlinson et al. 2003].

As soon as reflection travel times are considered, the finite difference method by Vidale needs to be modified. *Hole and Zelt (1994)* describe a method that is more accurate compared to other finite difference methods (e.g. *Lecomte & Hamran (1993)*). Reflection travel times are computed under the assumption that the reflecting interface, the incident wavefront and the reflected wavefront are locally planar. Travel times immediately above the reflector will be replaced with reflected travel times using Snell's law of reflection. This can be achieved by defining the normal vector to the reflector  $\mathbf{n}$  and the incident ray vector  $\mathbf{q}$ .

Illustrated in *Figure 3.6*, the normal vector to the reflector, pointing upward, is defined by local differences as

$$\begin{aligned} n_{i,j}^x &= \frac{d_{i+1,j} - d_{i-1,j}}{2h} \\ n_{i,j}^y &= \frac{d_{i,j+1} - d_{i,j-1}}{2h} \\ n_{i,j}^z &= -1 \end{aligned} \tag{E.37}$$

with  $h$  defined as the grid spacing and  $d_{ij}$  as reflector depth function of the horizontal grid directions  $i$  and  $j$ . Depth values are not required to lie at grid nodes.

The incident ray vector is defined through the already-computed incident-wave travel times

$$\begin{aligned} q_{i,j}^x &= \frac{t_{i+1,j,k2} - t_{i-1,j,k2}}{2h} \\ q_{i,j}^y &= \frac{t_{i,j+1,k2} - t_{i,j-1,k2}}{2h} \\ q_{i,j}^z &= \frac{t_{i,j,k2+1} - t_{i,j,k2}}{h} \end{aligned} \tag{E.38}$$

with  $k2$  defined is the deepest grid node such that all nine grid nodes ' $i \pm 1, j \pm 1, k2$ ' lie above the reflector (*Figure 3.6*).

The travel time at reflector depth  $d_{ij}$  is then given by

$$t_{i,j,d} = t_{i,j,k2} + q_{i,j}^z (d_{i,j} - z_{k2}) \tag{E.39}$$

with  $z_{k2}$  as the depth at the grid node  $k2$ .

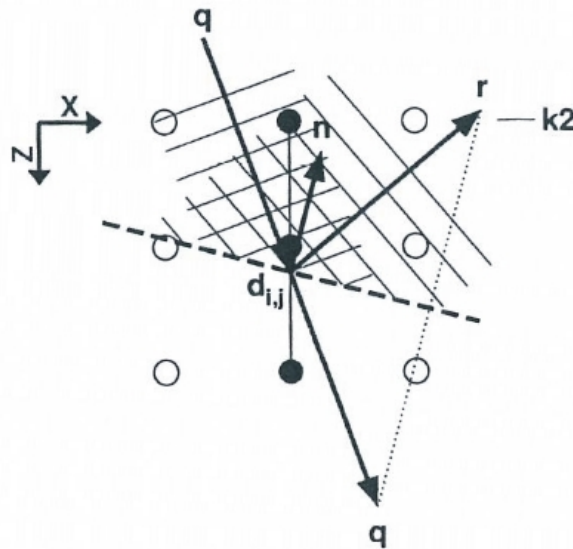


**Figure 3.6.** Illustration of travel time computation at the grid points immediately above the reflector (heavy dashed line) [Hole et al. 1994]. Circles represent grid nodes; reflected travel times are computed at the black grid nodes. Application of Snell's law at the interface results in the reflected ray  $\mathbf{r}$ . Derivation of  $\mathbf{r}$  requires to take the dot product (dotted line) used in E.40.

The reflected vector is now obtained through Snell's law:  $\mathbf{r} = \mathbf{q} - 2(\mathbf{q} \cdot \mathbf{n} / |\mathbf{n}|)\mathbf{n} / |\mathbf{n}|$  (E.40)

The reflected travel times at the grid nodes between the reflector and  $k_2$  are

$$t_{i,j,k} = t_{i,j,d} + r_{i,j}^z (z_k - d_{i,j}) \quad (\text{E.41})$$

This algorithm is accurate for smoothly dipping reflectors with 2-D dips up to  $\sim 45^\circ$  and 3-D dips up to  $\sim 35^\circ$ . For larger dips,  $k_2$  is too distant from the underlying reflector and the local plane assumption is no longer valid.

### 3.4 Travel time inversion

---

Here a simple inversion scheme based on the 3-D finite difference algorithm of *Vidale (1990)* is presented. The procedure described by *Hole (1996)* requires the velocity model to be uniformly spaced on a 3-D grid and to coincide with the depth grid; the node interval, however, can be adjusted accordingly. To get this inversion system working, the travel times of the phases to be inverted have to be known and need to be introduced into the system. Additionally, an initial guess of the reflector depth is required. The principle of this method includes the calculation of travel times for the initial reflector depth and subsequent comparison to real travel times. As they may not coincide the first time, the reflector depth will be changed slightly and the travel times will be calculated anew and compared until the real travel times and the calculated ones fit together.

The reflection travel time of a ray in a model that contains one horizontal interface is given as

$$\begin{aligned} \cos \theta &= \frac{r}{z} \Rightarrow r = z \cdot \cos \theta \\ t &= \frac{2r}{v} = \frac{2z \cos \theta}{v} \end{aligned} \quad (\text{E.42})$$

with  $z$  as the reflector depth,  $v$  the velocity above the reflector and  $\theta$  the angle between the ray and the interface normal (*Figure 3.7*).

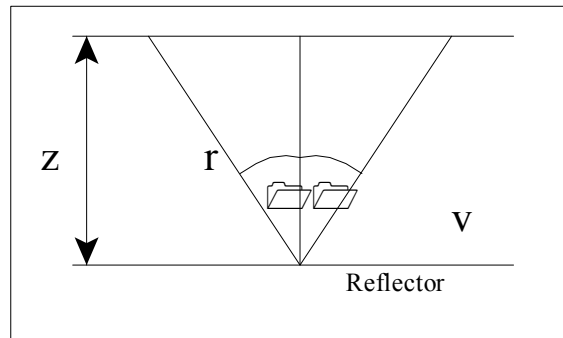


**Figure 3.7.** Sketch illustrating the relationship between the travel time and depth of a reflector.

For a dipping reflector, the above equation extends to

$$t = \frac{2z \cos \theta}{v} \cos \alpha \quad (\text{E.43})$$

with  $\alpha$  as the dip of the reflector (measured as the angle between the vertical axis and the normal to the reflector).

The relation between a small change in reflector depth  $\delta z$  and the resulting change in travel time  $\delta t$  can be expressed when rewriting E.43 in the following way

$$\boxed{\frac{\delta t}{\delta z} = \frac{2 \cos \theta}{v} \cos \alpha} \quad (\text{E.44})$$

The right-hand side of equation E.44 can be calculated for each ray through the velocity and the reflector model (dip  $\alpha$ ) and the ray path ( $\theta$ ). The change in depth  $\Delta z_k$  for the k-th travel time residual  $\Delta t_k$  is then

$$\Delta z_k = \frac{\Delta t_k}{\delta t / \delta z} \quad (\text{E.45})$$

where the depth perturbation applies at the reflection point.  $\Delta t_k$  is obtained when subtracting the calculated travel times for the initial reflector depth from the observed travel times.

Introducing M travel time data into the system will result in M depth perturbations  $\Delta z_k(x, y)$  with  $k= 1$  to M (*Figure 3.8b*), which are gridded to obtain a reflector perturbation model  $\Delta z_{ij}$ . The choice of the gridding scheme is rather important, especially when there are large gaps in reflection point coverage. The Laplace interpolation is based on the equation  $\nabla^2[\Delta z(x, y)]=0$  and introduces a function  $\Delta z(x, y)$  with minimal structure between the depth perturbations (*Figure 3.8c*). For real data sets with errors, spikes may occur at gridding when closely spaced reflection points show different depth perturbations. These effects can be reduced when smoothing the gridded surface using a 2-D moving average filter (*Figure 3.8d*).

Since the relationship between travel time and depth is nonlinear, iterations are needed. Each step of the iterative procedure comprises forward modelling of reflection times, inversion (calculation of the depth perturbation surface), gridding, smoothing and update of the reflector model.

Equation E.43 represents the travel time for a simple 1-layer model with a constant velocity. When considering an interface that separates two media of different known velocities, equation E.44 changes to

$$\boxed{\frac{\delta t}{\delta z} = \left[ \frac{\cos \theta_1}{v_1} - \frac{\cos \theta_2}{v_2} \right] \cos \alpha} \quad (\text{E.46})$$

where  $\theta_1$  and  $\theta_2$  are the angles between the ray and interface normal measured above and below the interface and  $v_1$  and  $v_2$  are the velocities above and below the interface.



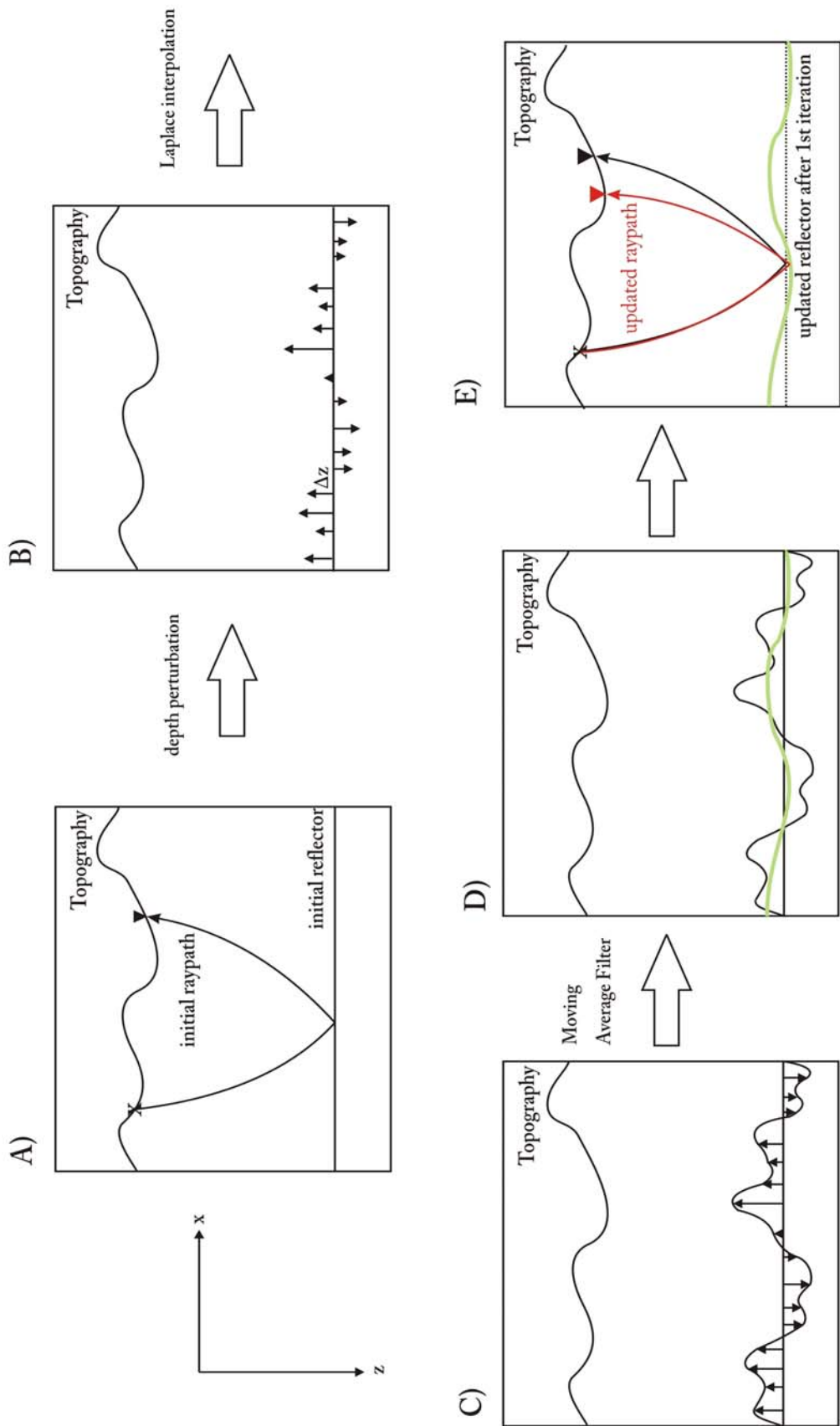


**Figure 3.8.** Illustration of inversion principle by Hole (1996) using a simple depth model. (A) Starting model with a reflector situated at a particular depth, (B) forward modelling of reflection travel times resulting in depth perturbations, (C) gridding of discrete depth perturbation points using Laplace Interpolation, (D) subsequent application of moving average filter, (E) updated reflector model after first iteration.

### 3.5 Parameterization of the velocity model

---

In practical applications, the whole model is subdivided into a network of cells, of which **tetrahedron** and **rectangular box cells** are the most widely used. The velocities are to be specified either at the grid points or, alternatively, in the centres of the cells. The correct grid cell size is mainly dependent on the complexity of the velocity function. Complicated velocity distributions may require a smaller grid size to be suitable for analytical solutions, whereas simpler distributions (e.g. constant velocity gradient) may just be defined by one big cell. The velocity inside the grid cells is approximated by simple analytical velocity laws. The simplest case is to use a constant velocity within individual cells. This, however, automatically implies the introduction of interfaces of first order at the cell boundaries. This can be avoided when using velocity laws that introduce interfaces of second order only. The velocity distribution is then continuous across the cell boundaries, only the gradient is discontinuous.

## 4 Data and correlation of travel times

Data used for this thesis were acquired during CELEBRATION 2000 and ALP 2002 experiments. These include 7 profiles (43 shots and 827 receivers) from the CELEBRATION 2000 data set and all ALP 2002 profiles (see *Figure 4.1a*). The ALP 2002 data set comprises all 39 shots and 947 receivers along 13 profiles. The average receiver distance is 2.9 km on high-density profiles (1208 receivers) and 5.8 km on low-density profiles (583 receivers). The whole data set encompasses 78 933 traces, of which approximately 20 % are inline data.

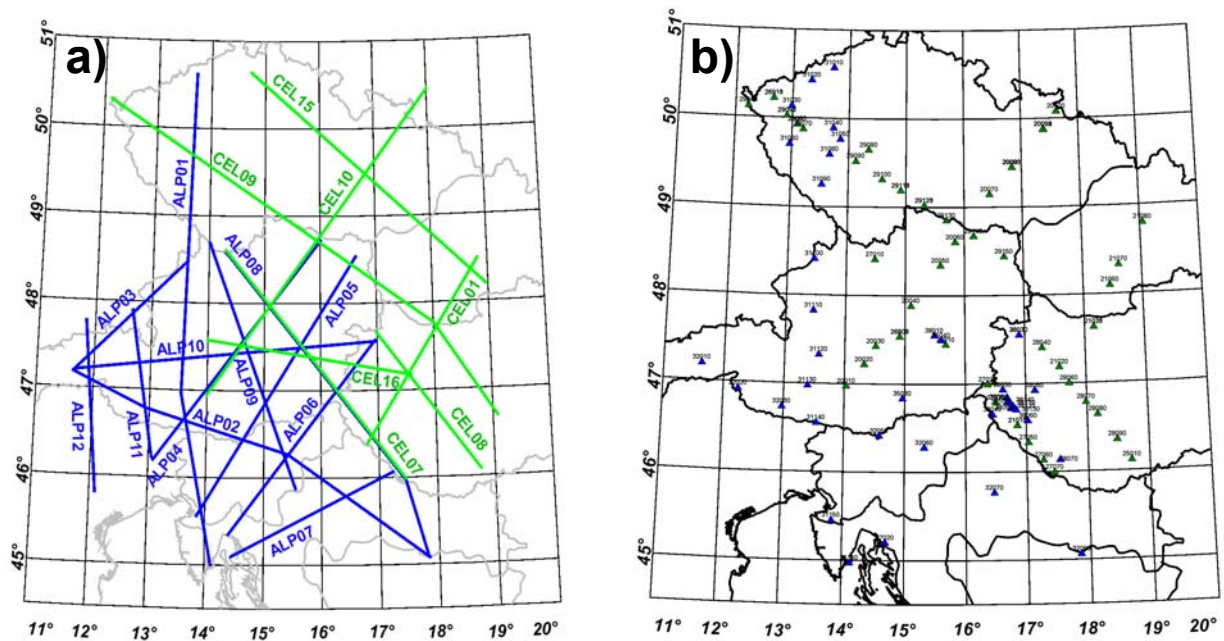


**Figure 4.1.** (a) Profiles of CELEBRATION 2000 and ALP 2002 experiments used for this thesis; (b) according shot layout.

Shots and receivers in the Bohemian Massif and in the Pannonian Basin provide record sections with high signal-noise ratio, compared to a lower signal-noise ratio in the Alpine region.

Analysis of the data reveals significant reflective events which can be associated with upper mantle features. Reflection travel times were picked between offsets of  $\sim 250$  km and  $\sim 500$  km. On most seismic sections only one single reflective event is present; however, on a couple of sections an additional second event can be seen (e.g. *Figures 4.8* and *4.9*). These events appear at offsets  $>350$  km and are separated by a gap in reflectivity from the neighbouring events. Reflection events appearing at greater offsets have been marked with 'R2' and those at lower offsets ( $<350$  km) with 'R'/'R1'. The occurrence of the reflecting events within a limited offset range only points towards a velocity increase below the reflecting interface. As shown in Tooley et al. (1965), strong amplitudes occur around the critical offset for a velocity increase. Ray tracing modelling for a reflector depth of 60 km and a realistic velocity distribution shows that the critical offset is approximately 250 km, which fits nicely with the observed reflections.

The procedure of travel time picking was repeated several times. After a comparison with modelled travel times (section 5.2), those picks that differed significantly were excluded from further computational steps.

Finally 1078 travel times referring to the first reflective event 'R'/'R1' were picked (see section 5.4). Due to the low number of 'R2' travel times, travel time inversion was carried out for travel time picks of 'R'/'R1' only.

In the following section, examples of record sections containing remarkable reflectivity at greater offsets will be presented. These reflective events mainly occur at cross-line recordings, a few are obtained on in-line sections, especially on CEL07 and CEL10.

Travel times on the following seismic sections are reduced by 8 km/s.

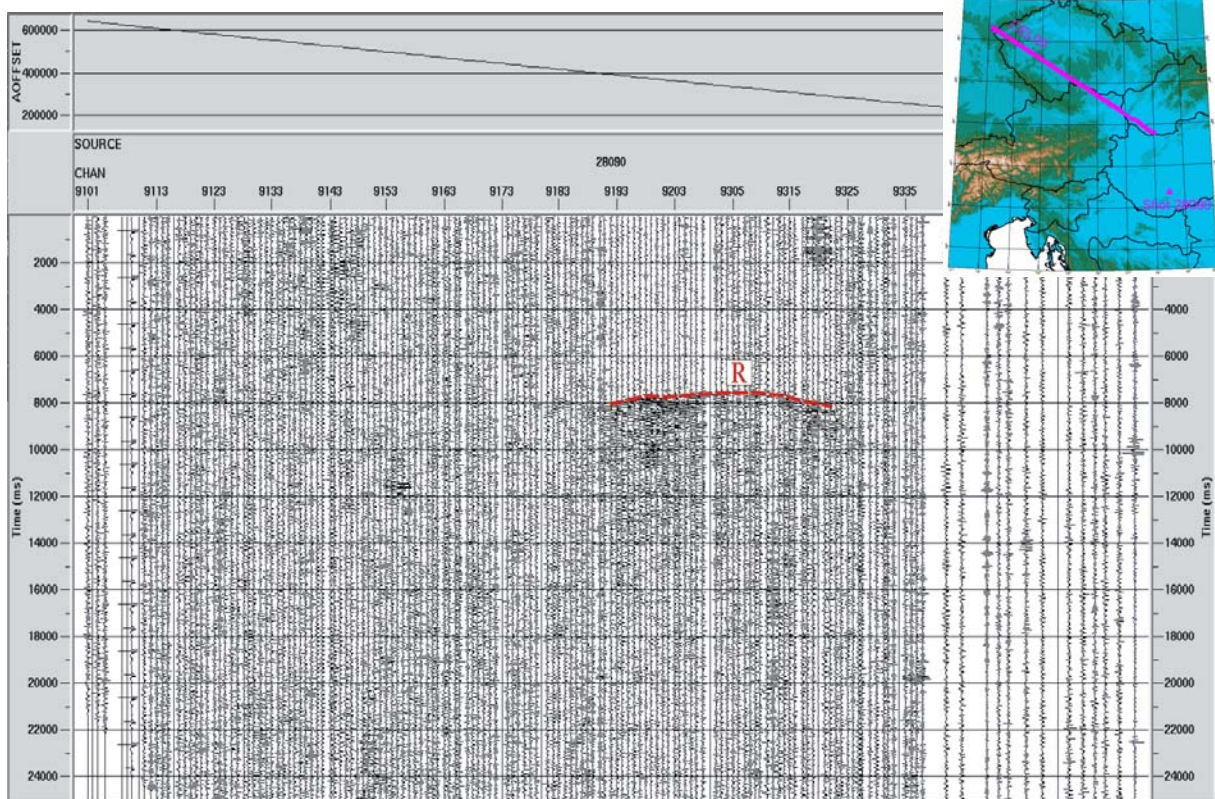


**Figure 4.2.** This cross-line section (NW-SE) is characterised by a single reflective event at an offset range between ~300 km and ~400 km. Absolute offset is shown by the thin black line above the section.

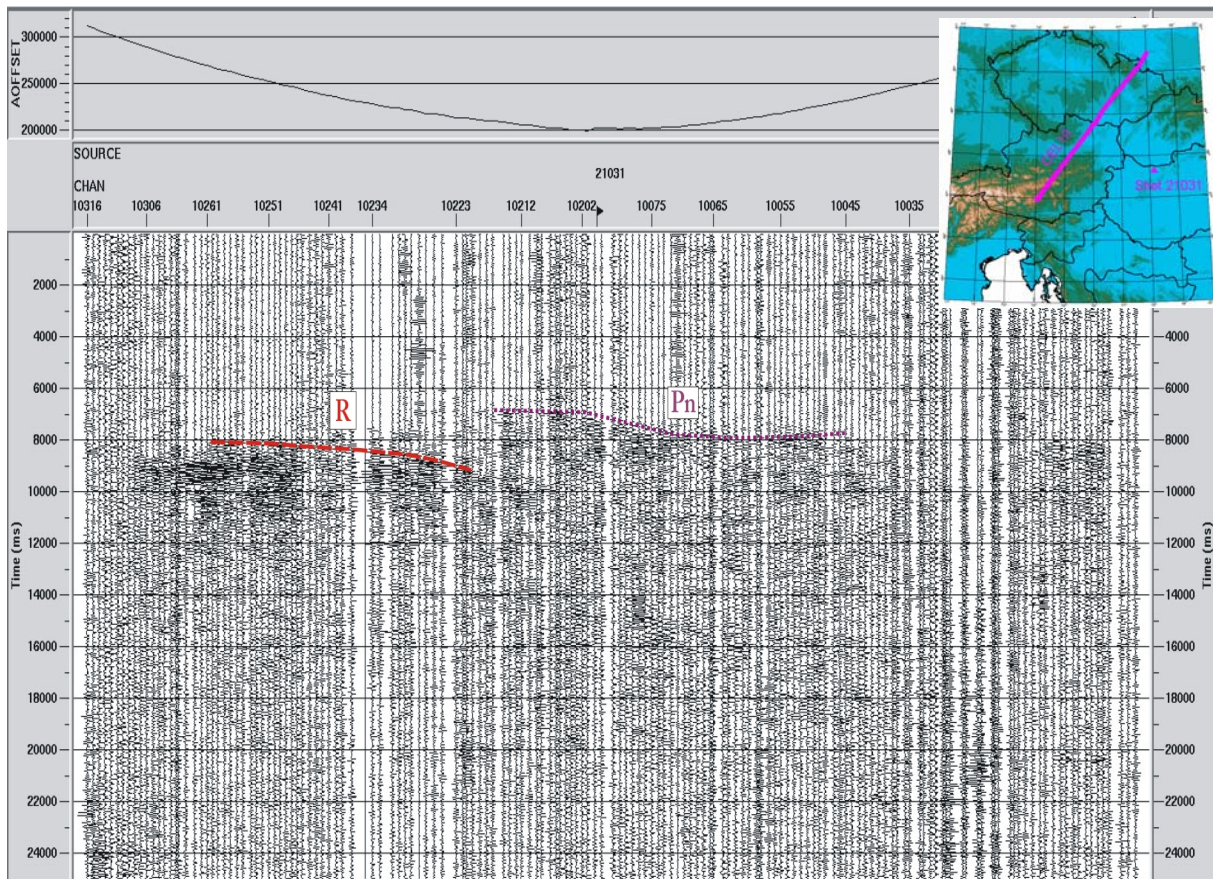


**Figure 4.3.** Strong reflectivity is observed at offsets between  $\sim 220$  km and 270 km; its lateral extent, however, is not clearly limited due to a lower signal/noise ratio. At lower offsets ( $\sim 200$  km) the Pn-phase (diving wave through the upper mantle) can be recognized. The section runs SW-NE.

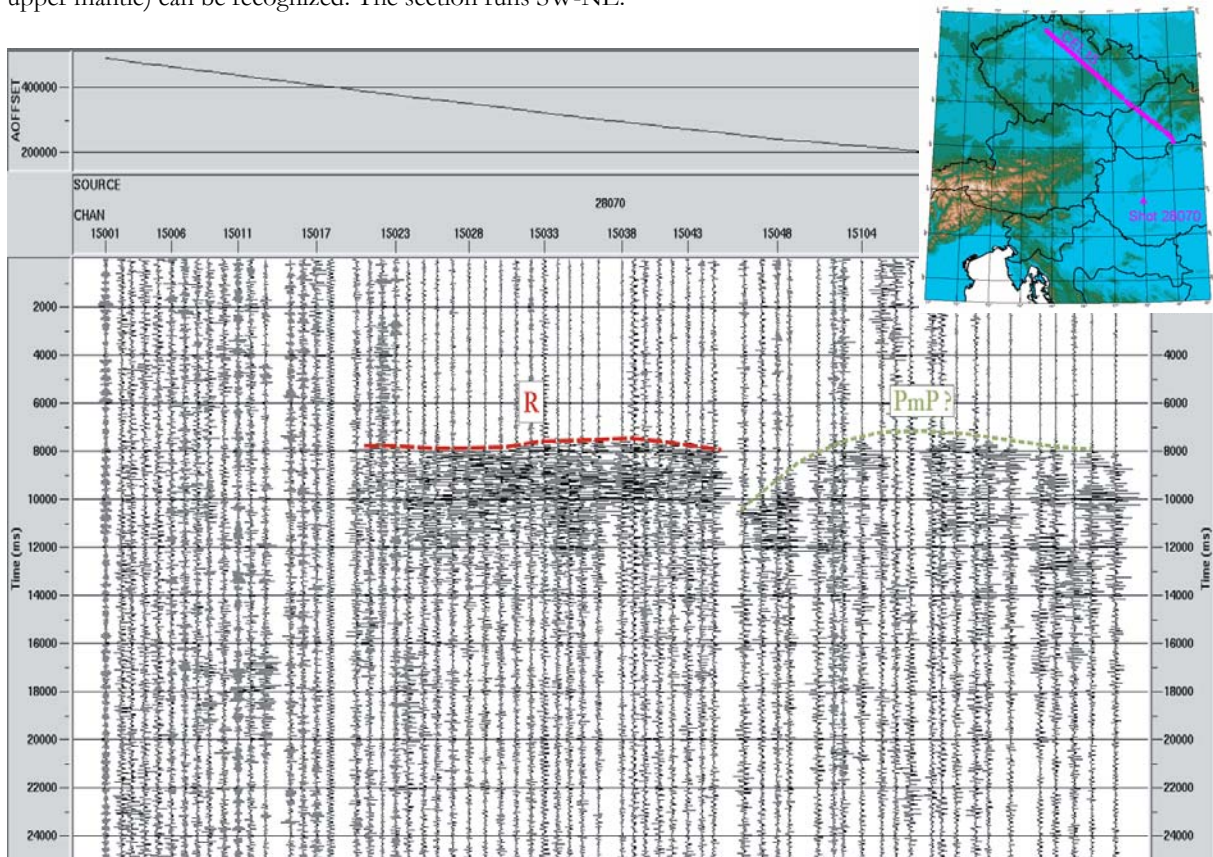


**Figure 4.4.** Due to a good signal/noise ratio the reflective event is indicated by very sharp first-arrivals. A PmP-phase is supposed to be on the right-hand side of the section. The section runs NW-SE.

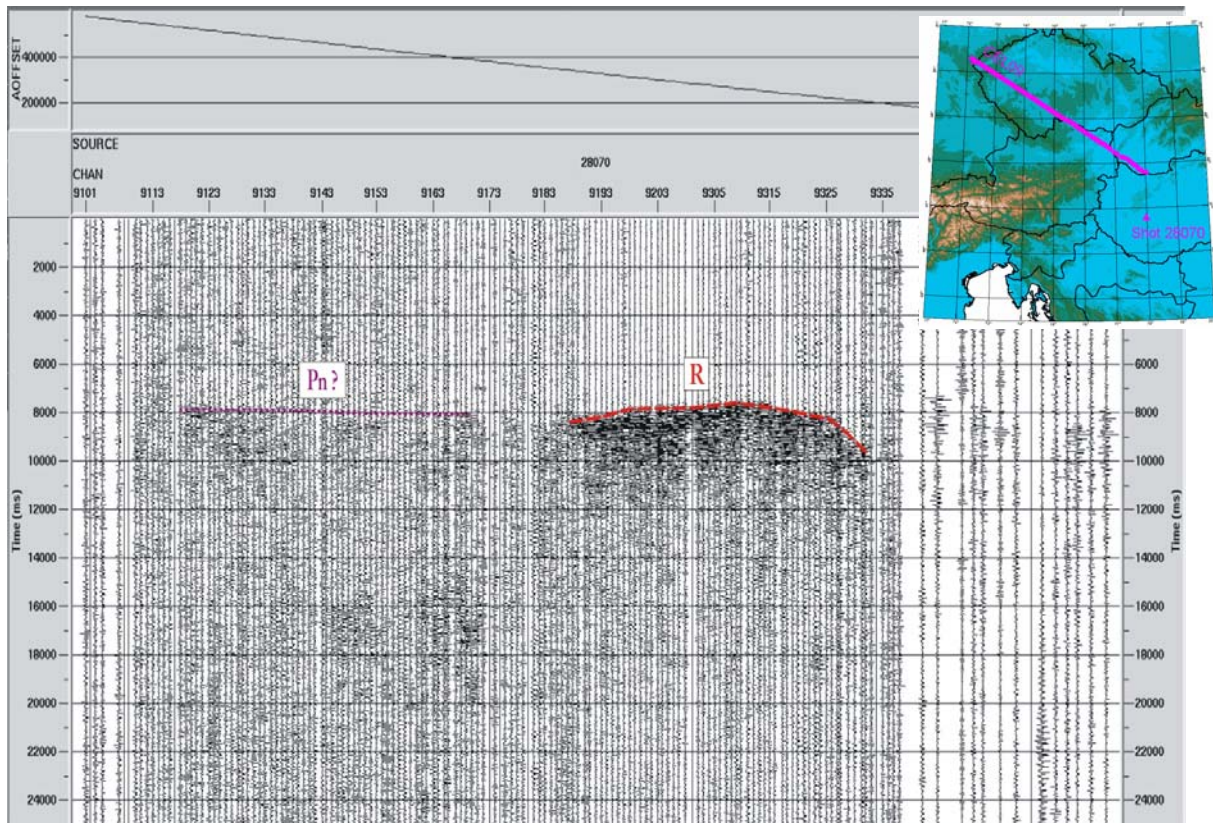


**Figure 4.5.** This section (NW-SE) contains a very strong and clearly bounded reflective phase. Notice the increase in travel time between trace numbers 9325 and 9335. This is due to the low velocities in the Vienna basin which increase travel times. Just left of this event there seems to be another phase (Pn ?) which cannot be seized completely due to a lower signal/noise ratio.

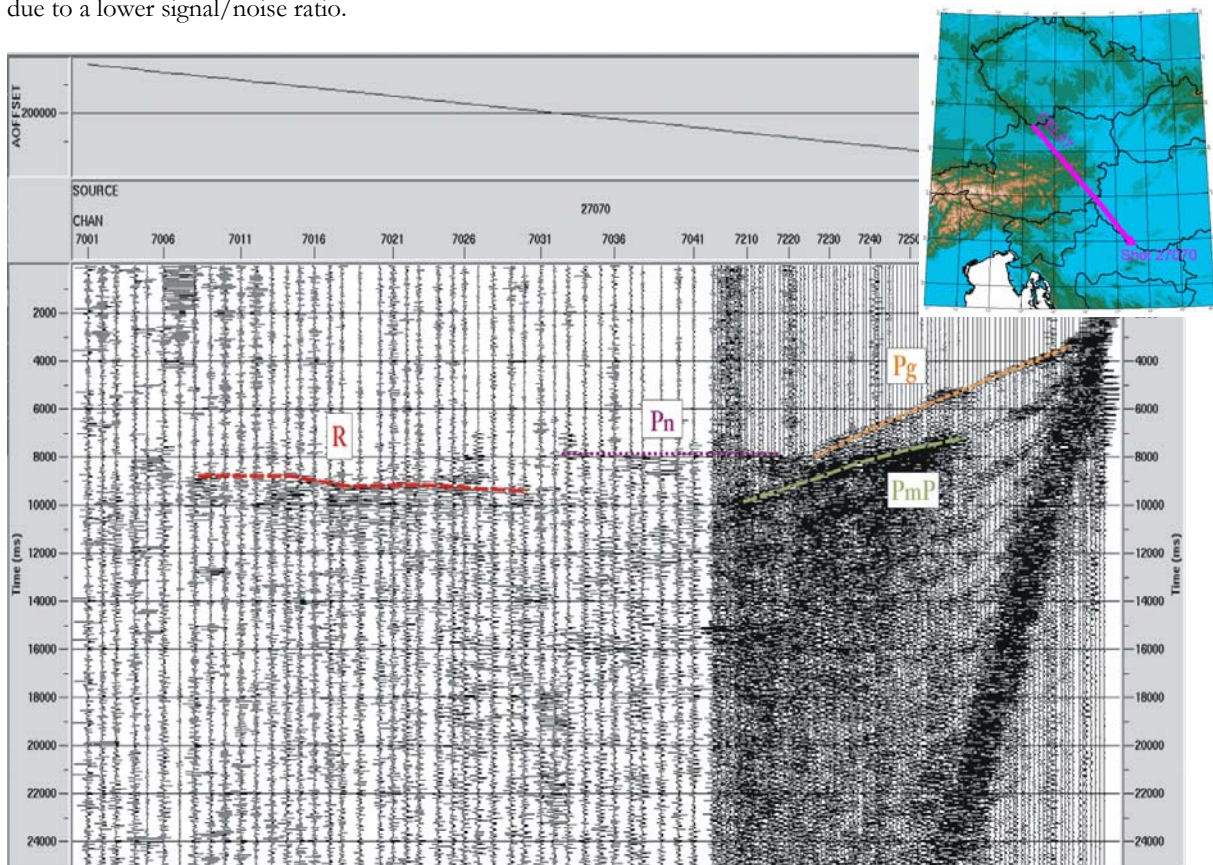


**Figure 4.6.** Beside the significant reflective event at offsets beyond 200 km, this section (NW-SE) shows several other seismic phases: Pn-, PmP- and the Pg-phase (diving wave through the crust).

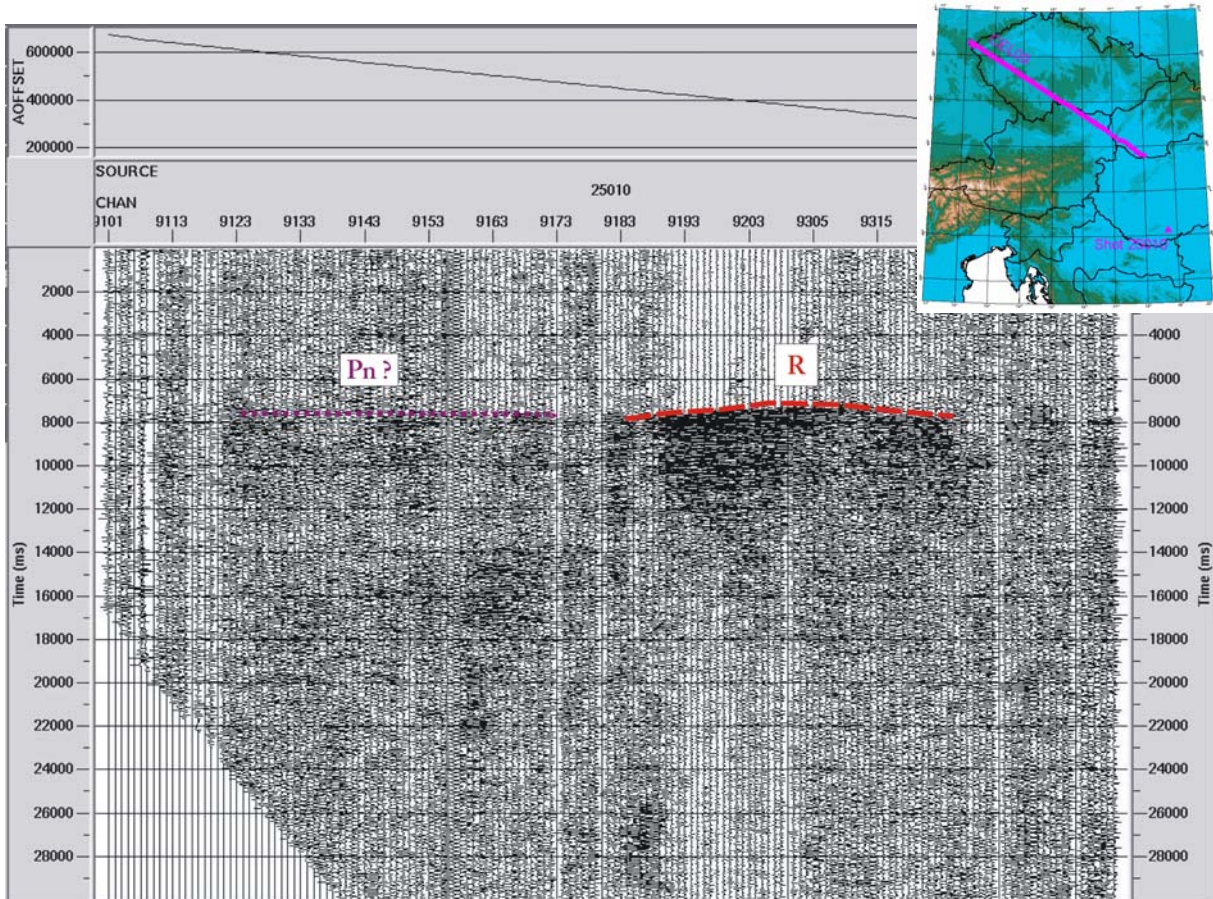


**Figure 4.7.** A very sharp first-arrival event is observed at ~400 km. At greater offsets (500 km, 600 km) a Pn-phase may be observed. The section runs NW-SE.

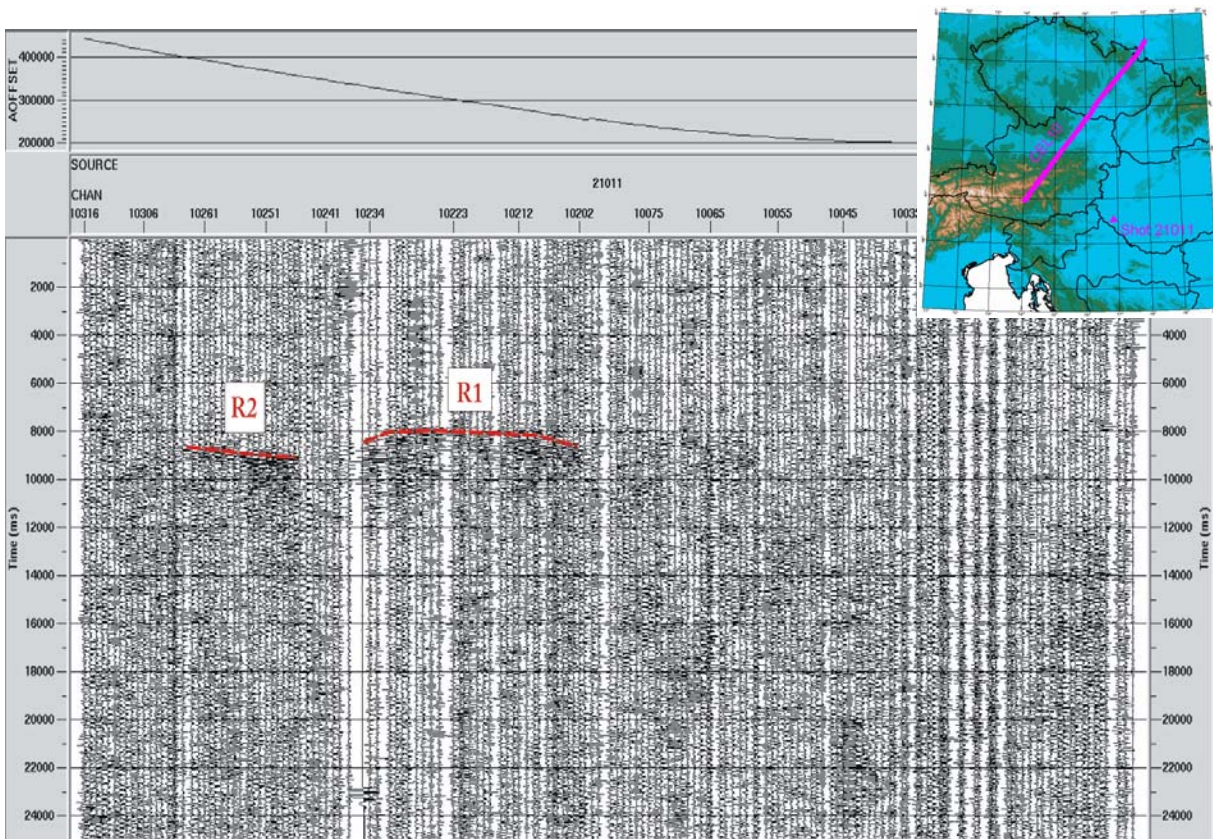


**Figure 4.8.** This is an example of a section in which seemingly two separate reflective events occur. Notice the time shift between them. The section runs SW-NE.

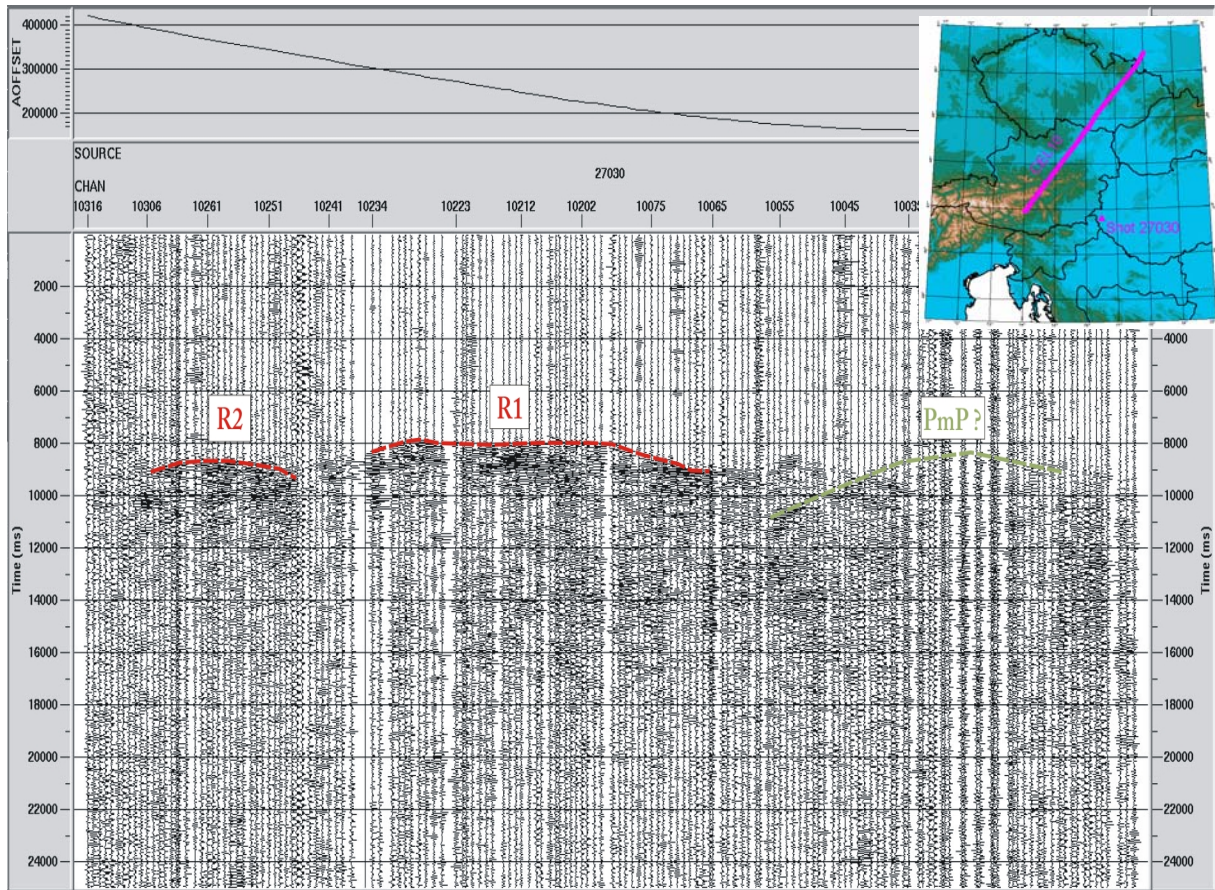


**Figure 4.9.** Another example of two different reflective events separated by a gap in reflectivity. The section runs SW-NE.



## 5 Modelling of ‘R1’- travel times

---

### 5.1 Initial estimation of the reflector depth

---

Before the actual reflector depth can be derived, it is useful to determine the geographic distribution of travel times ‘R1’ in our area of investigation. Travel time coverage is obtained by applying the common mid-point (CMP) method which assumes the interfaces to be horizontal and the velocity to be dependant only on depth (1-D velocity distribution). This assumption, however, is too simple for real data, thus the CMP-method provides only limitedly accurate information about travel time locations.

Three zones of significant occurrences of travel time – A, B and C (*Figure 5.1*) – can be distinguished. Due to a lower signal-noise ratio in the alpine region and sparse 3-D seismic coverage in the Bohemian Massif, reflection points in these regions (B and C) are not as abundant as in area A, which lies within the Pannonian Basin, an area with higher signal-noise ratio. Consequently, this thesis deals with the investigation of region A, where travel times occur in greater number – a fact which allows for better determination of the reflector structure in the inversion process.

Travel times associated with second reflective events (‘R2’), as observed in *Figures 4.8* and *4.9*, are located in region A too, but will be neglected here and be treated more accurately in chapter 6.

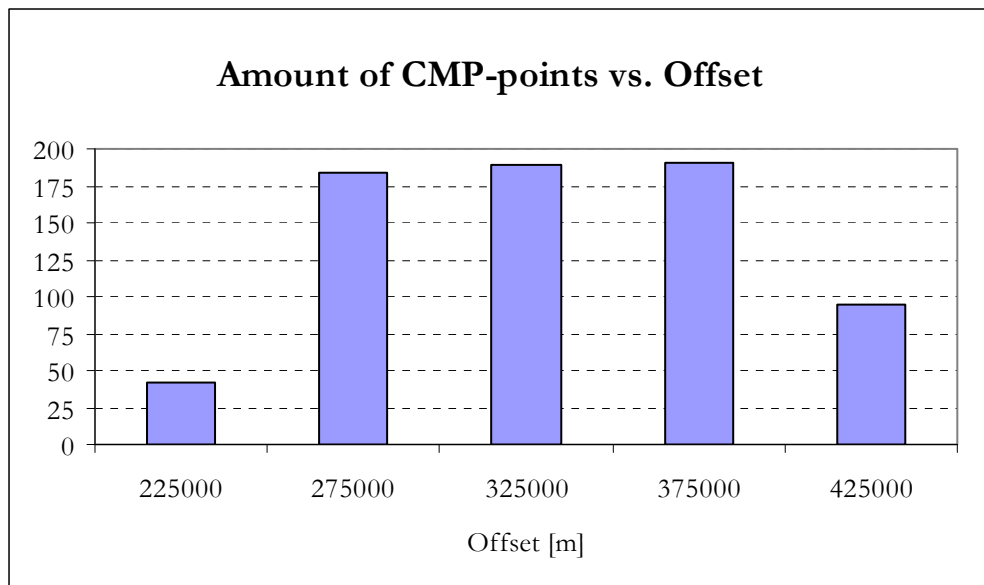
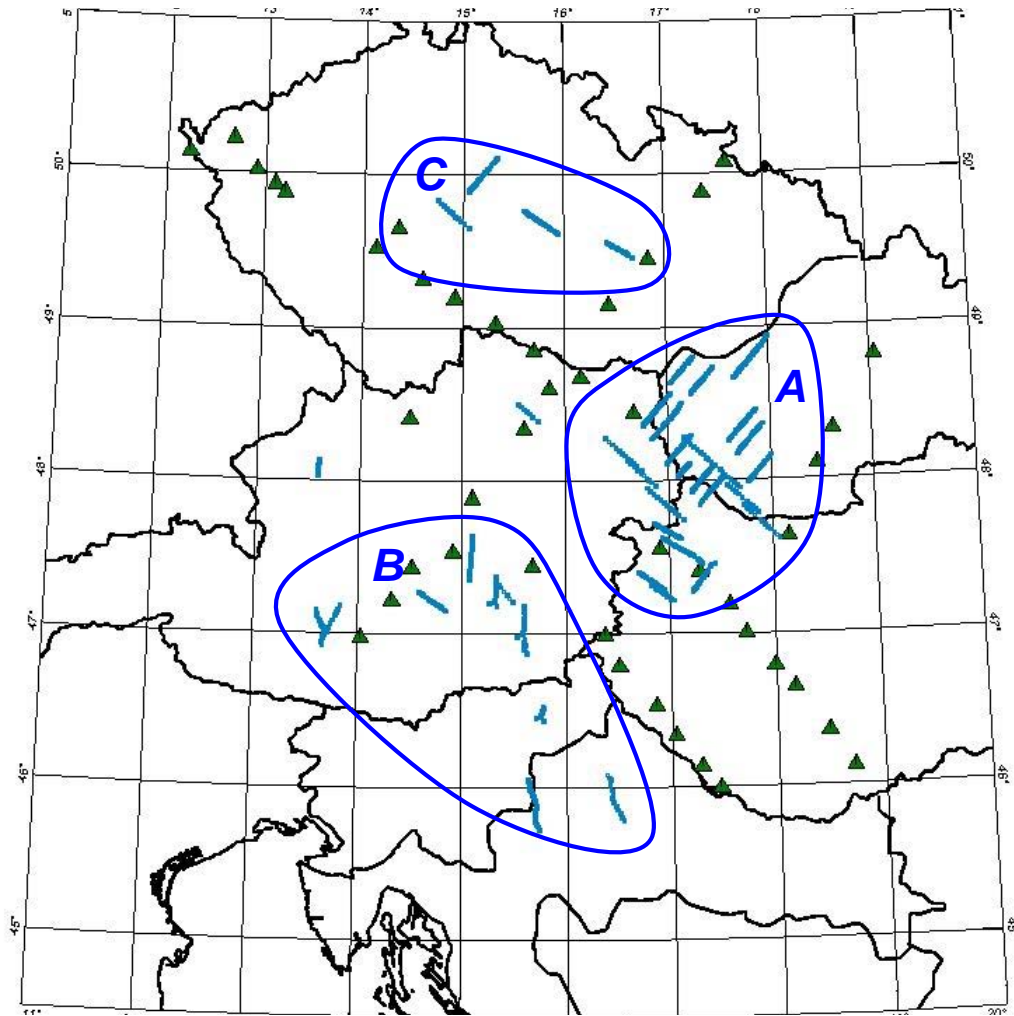


**Figure 5.1.** Picked travel times can be divided into three geographically distinct zones – A, B and C. The histogram at the bottom classifies the CMP-points into offset intervals (column ‘225000’: 197000 m – 250000 m, column ‘275000’: 250000 m – 300000 m, column ‘325000’: 300000 m – 350000 m, column ‘375000’: 350000 m – 400000 m, column ‘425000’: 400000 m – 460000 m).

Derivation of an initial depth model requires the comparison of picked travel times with modelled travel times. For reasons of simplicity, travel times will be calculated for a simple two-layer case with constant velocities. The first layer represents the crust with an average crustal velocity  $v_c$  and the bottom layer the upper mantle with the average velocity  $v_m$  (Figure 5.2). All interfaces (topography, Moho, reflector) are assumed to be horizontal. Based on this model, the seismic phases 'Pg', 'PmP' and 'Pn' will be modelled; the PIP-travel times, on the other hand, will be calculated for a simple 1-layer case with rms-velocities.

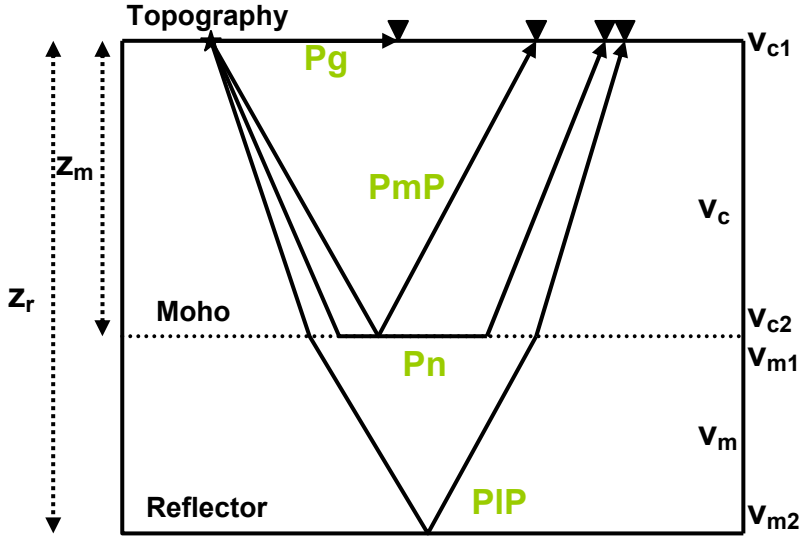


**Figure 5.2.** Illustration of the ray pattern for a simple two layer case with constant velocities. The following seismic phases occur: Pg (diving wave through the crust), PmP (Moho reflection), Pn (diving wave through the upper mantle) and PIP (interface reflection).  $Z_m$ : Moho depth;  $Z_r$ : reflector depth;  $v_{c1}$ : velocity in the upper crust;  $v_{c2}$ : velocity in the lower crust;  $v_{m1}$ : velocity in the upper mantle;  $v_{m2}$ : velocity at reflector depth.

The travel times for these phases are given as

$$t_{Pg} = \frac{x}{v_c} \quad (\text{E.47})$$

$$t_{PmP} = \frac{2}{v_c} \sqrt{\frac{x^2}{4} + z_m^2} \quad (\text{E.48})$$

$$t_{Pn} = 2 \cdot z_m \left( \frac{1}{\cos(\theta_c) \cdot v_c} \right) - \frac{\tan(\theta_c)}{v_{m1}} + \frac{x}{v_{m1}} \quad (\text{E.49})$$

$$t_{PIP} = \frac{2}{v_{rms}} \sqrt{\frac{x^2}{4} + z_r^2} \quad (\text{E.50})$$

with

- $x$ ... offset
- $v_c$ ... average crustal velocity
- $z_m$ ... Moho depth
- $\theta_c$ ... critical angle at Moho
- $v_{m1}$ ... Pn-velocity
- $v_m$ ... average upper mantle velocity
- $z_r$ ... reflector depth
- $v_{rms}$ ... rms-velocity of crust and upper mantle

$$v_{rms} = \sqrt{\frac{v_c \cdot z_m + v_m (z_r - z_m)}{\frac{z_m}{v_c} + \frac{z_r - z_m}{v_m}}} \quad (E.51)$$

The average upper mantle velocity equals the mean of the Pn-velocity ( $v_{m1}$ ) and the velocity at the reflector depth  $z_r$  ( $v_{m2}$ ); the average crustal velocity is calculated the same way as the mean between  $v_{c1}$  and  $v_{c2}$ . Lower mantle and lower crustal velocities are given as  $v_{m2} = v_{m1} + k_m (z_r - z_m)$  and  $v_{c2} = v_{c1} + k_c \cdot z_m$  respectively, with  $k_m$  as the mantle velocity gradient and  $k_c$  as the crustal velocity gradient.

Based on the above equations, travel time curves (Figures 5.3-5.6) have been computed for varying mantle velocity gradients  $k_m$  ( $0.015 \text{ s}^{-1}$  and  $0.005 \text{ s}^{-1}$ ) and reflector depths  $z_r$  (50 km and 70 km).

		Upper-crustal velocity [km/s]	6
Moho depth [km]	30	Lower-crustal velocity [km/s]	6.7
		Pn-velocity [km/s]	8
Reflector depth [km]	70	Mantle velocity gradient [ $\text{s}^{-1}$ ]	0.015
		Velocity at reflector depth [km/s]	8.6
Average crustal velocity [km/s]	6.35	Critical angle at Moho [radians]	0.992691962
Average mantle velocity [km/s]	8.3		
RMS-velocity [km/s]	7.40		

Table 5.1. Input parameters for the travel time model of Figure 5.3.

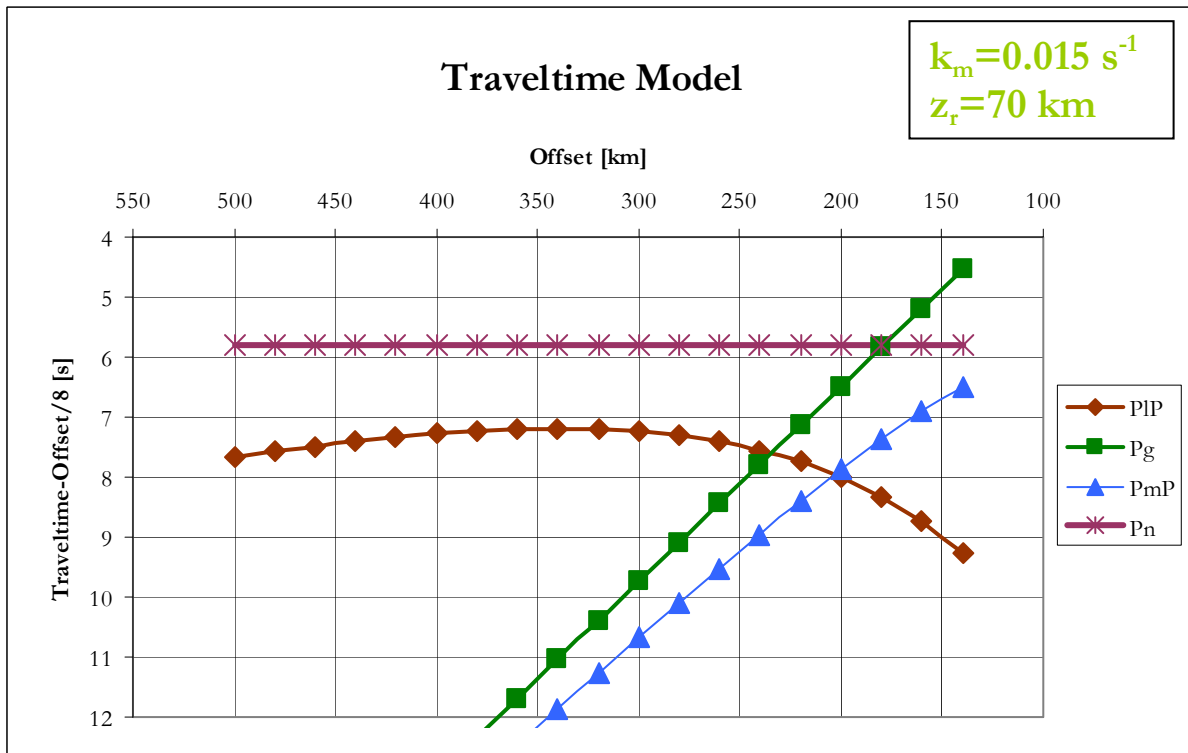


Figure 5.3.

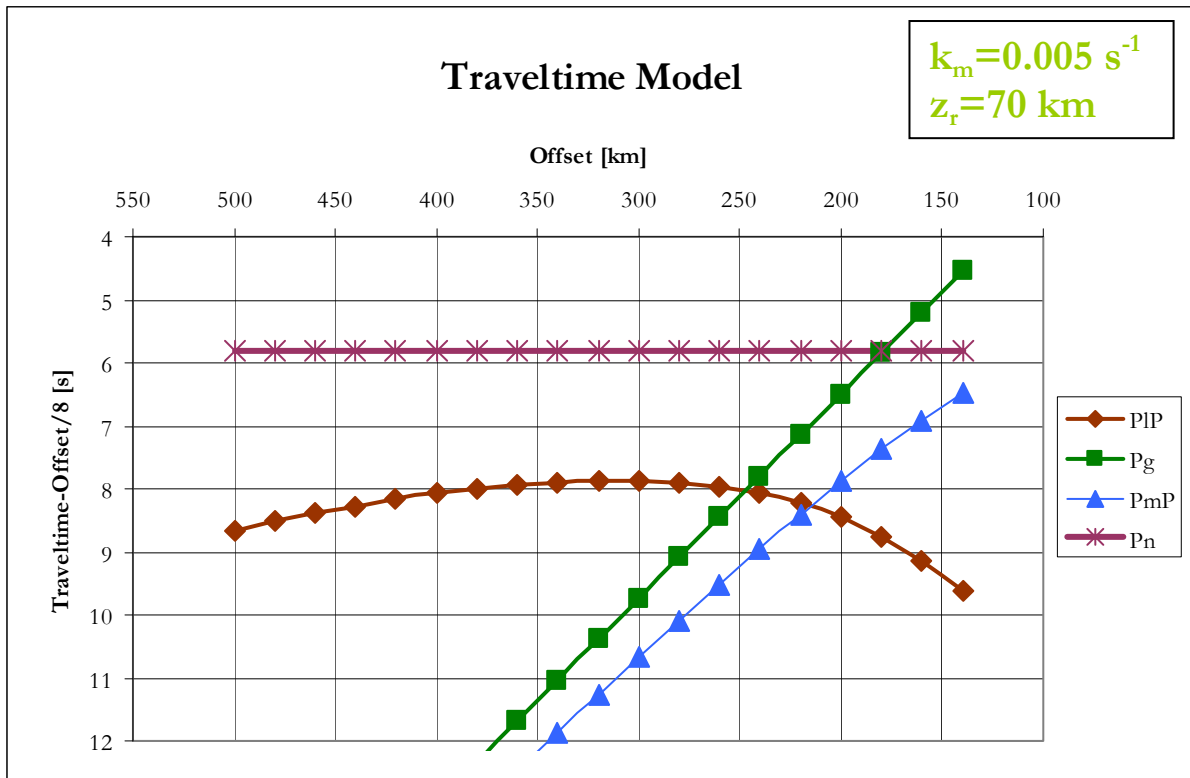


Figure 5.4.

The travel time curves of *Figures 5.3 and 5.4* indicate the influence of varying mantle velocity gradients on first-arrival travel times of the PIP-phase when the reflector depth is kept constant at a depth of 70 km. The lower the gradient, the later the first-arrivals and the stronger the curvature of the PIP-phase, especially at greater offsets.

Changing the reflector depth significantly alters the course of the PIP-Phase (compare Figures 5.3/5.4 and 5.5/5.6) with a stronger curvature in travel times.

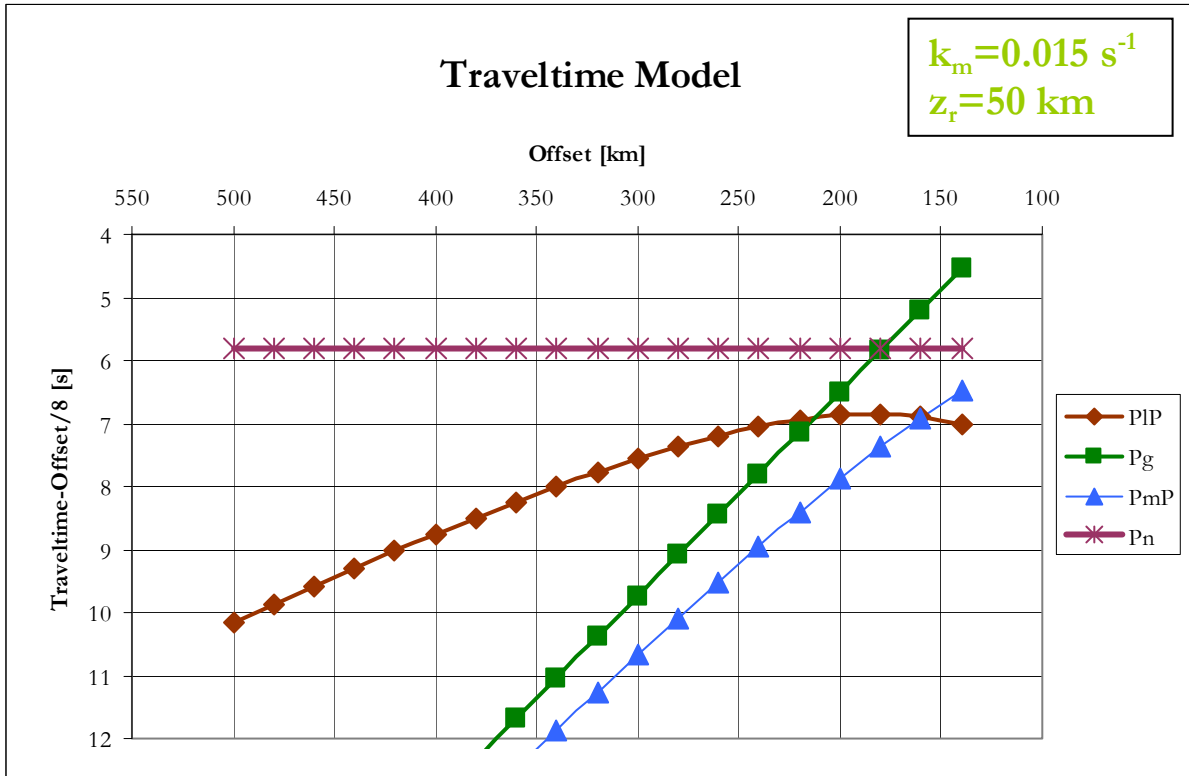


Figure 5.5.

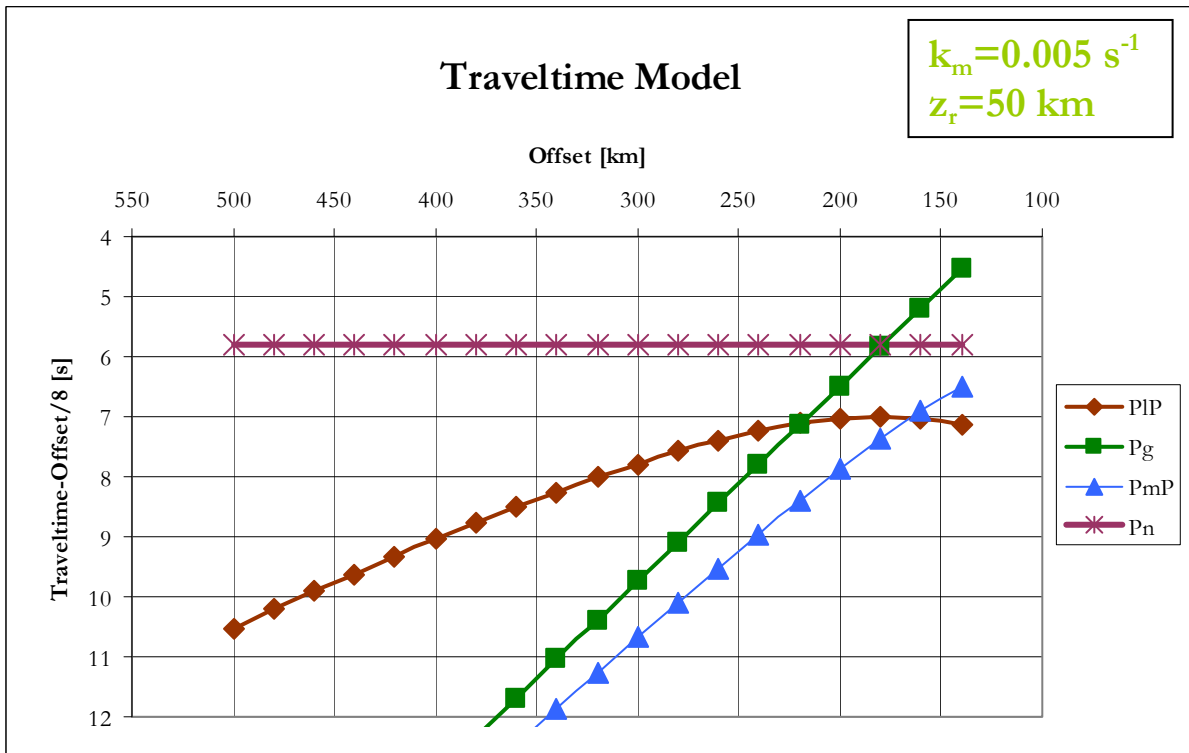


Figure 5.6.

Comparison of modelled PIP-travel times from the reflector interface with picked travel times gives a first estimation of the reflector depth.

Unfortunately, the lack of information about the mantle velocity gradient, which is supposed to range between  $0.01 \text{ s}^{-1}$  and  $0.002 \text{ s}^{-1}$ , and limited information about the reflector depth, permit a variety of travel time models and makes it impossible to extract an exact reflector depth-model. One plausible model is presented in *Figure 5.7*, with a **reflector depth of 70 km** and a **mantle velocity gradient of  $0.01 \text{ s}^{-1}$** . The other parameters such as crustal velocities, Moho depth and Pn-velocities are relatively well determined from previous studies and were not varied.

The simplification of using average velocities, however, significantly influences the resulting reflector depths when compared to models with a real subsurface velocity distributions. The usage of constant velocity layers automatically implies linear ray paths, whereas the ray paths for non-constant velocities are curved. Assuming a common ray starting and ending point for both models, travel times based on linear ray paths are shorter than those for curved ray paths. Thus, to compensate this travel time difference and to yield equal travel times, the reflector needs to be shifted to a greater depth. Calculated reflector depths based on models with constant velocities are generally too deep since their simplified calculation does not account for curved ray paths. This effect impacts particularly on the calculated PIP-travel times which are based on a 1-layer model. Estimated depth values, thus, need to be regarded cautiously.

		Upper-crustal velocity [km/s]	6
Moho depth [km]	30	Lower-crustal velocity [km/s]	6.7
		Pn-velocity [km/s]	8.12
Reflector depth [km]	70	Mantle velocity gradient [ $\text{s}^{-1}$ ]	0.01
		Velocity at reflector depth [km/s]	8.52
Average crustal velocity [km/s]	6.35	Critical angle at Moho [radians]	0.970420153
Average mantle velocity [km/s]	8.32		
RMS-velocity [km/s]	7.41		

Table 5.2. Input parameters for the calculated travel times in Figure 5.7.

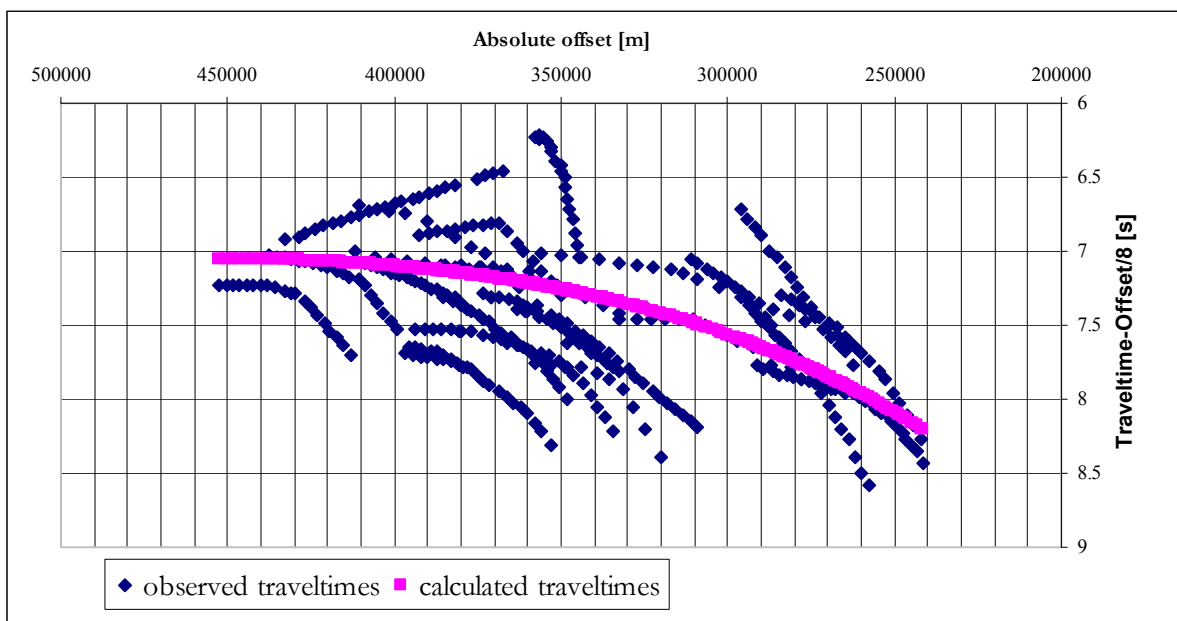


Figure 5.7. Calculated PIP-travel times are adjusted accordingly to fit the picked travel times.

## 5.2 Travel time computation based on the ray tracing equations (program ‘ANRAY’)

The program ‘ANRAY’ (<http://seis.karlov.mff.cuni.cz>; program description, see *Appendix A.2*) is based on the ray tracing equations and can be used to compute rays, travel times and ray synthetic seismograms in 3-D laterally varying anisotropic and isotropic structures. Two different modes of computation need to be distinguished for the application in this thesis – initial-value ray tracing and two-point ray tracing.

### 5.2.1 Depth and velocity model

The model used for computation with ‘ANRAY’ extends over 600 km in x-direction, 660 km in y-direction and 100 km in z-direction. Model building involves the determination of interfaces, which separate layers of different elastic parameters (velocities) and secondly, the definition of velocities inside these layers. In total, four interfaces – topography (top of the model), Moho-discontinuity, reflector interface and bottom boundary of the model – were generated. This is equivalent to three layers. The bottom layer is needed when it comes to amplitude calculation. Interfaces need to be specified on a regular grid; the grid spacing may be adjusted accordingly depending on data density and may be varied from interface to interface. Between the grid points the interface is interpolated with bicubic splines.

The seismic model with its interfaces (topography, Moho discontinuity) and velocities (crustal velocity distribution, Pn-velocities) is based on the results of ALP 2002 and CELEBRATION 2000 experiments. As *Figure 5.8b* indicates, the Moho depths are not defined everywhere; in regions where no depth values are present, interpolation and extrapolation was carried out to make data available everywhere within the model boundaries.

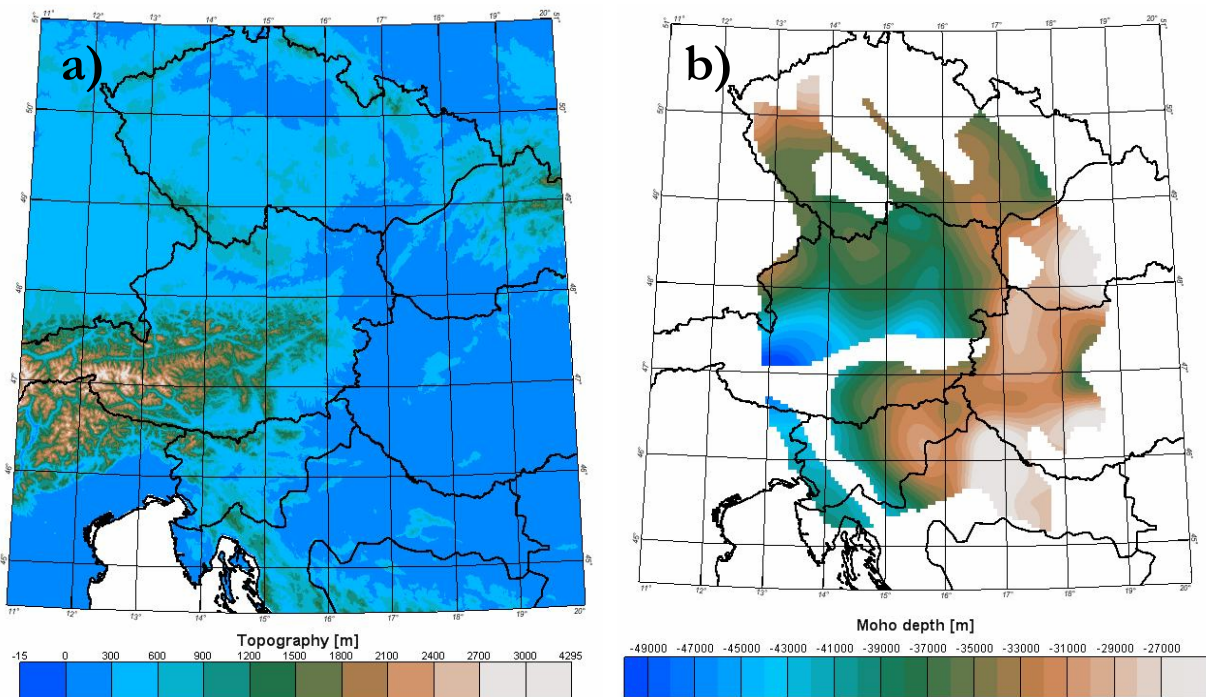


**Figure 5.8.** (a) Topography map and (b) Moho depth map within the area of investigation [Behm et al. 2007].



Grid spacing for topography and Moho is 20 km, both in x- and y-directions. Since the bottom interface of the model is defined as a horizontal plane, depth values can be simply assigned to the grid points at the model edges.

The same grid spacing as used for the interfaces is now used when it comes to allocating velocity values to grid points. Grid spacings in z-direction, however, can be chosen arbitrarily according to the complexity of the velocity distribution. For the first layer, which represents the crust, the number of grid points in x-, y- and z-direction is 34, 31 and 36 respectively, with grid spacings of 20 km horizontally and 1-2 km vertically. Velocity-depth slices for the crust are illustrated in *Figure 5.9*. Just as for Moho depths, velocities need to be interpolated/extrapolated in areas where no values are present.

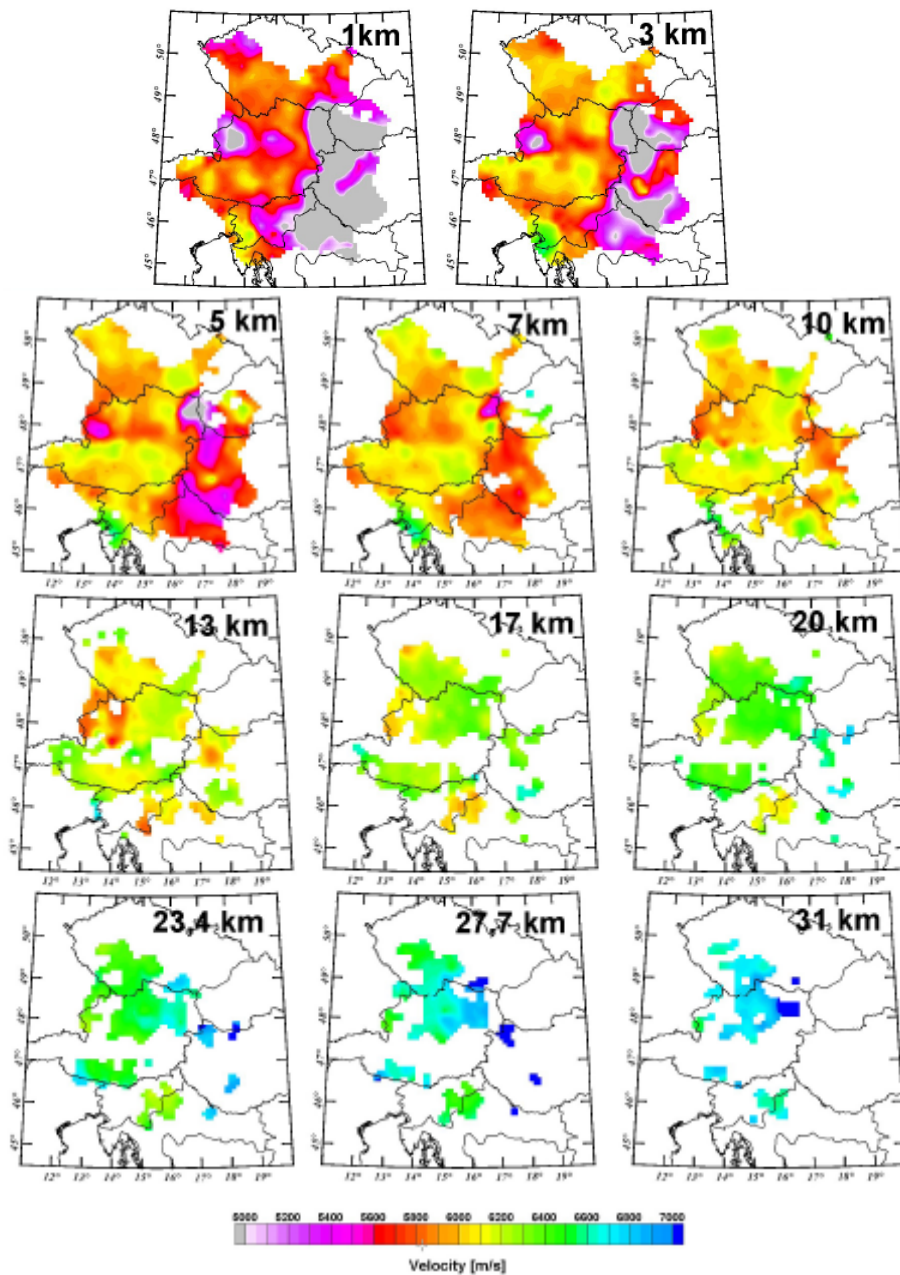


**Figure 5.9.** Velocity-depth slices through the crust down to depths of 31 km [Behm et al. 2007].

The Pn-velocities were determined to lie between 7.8 km/s and 8.2 km/s (see *Figure 5.10*).

The variation of upper mantle velocities with depth is only poorly known from previous studies. Therefore, a simple model is proposed which comprises the velocity on top of the upper mantle layer (*Figure 5.10*) and a vertical velocity gradient. As will be shown, the choice of the latter is crucial for the calculation of travel times.

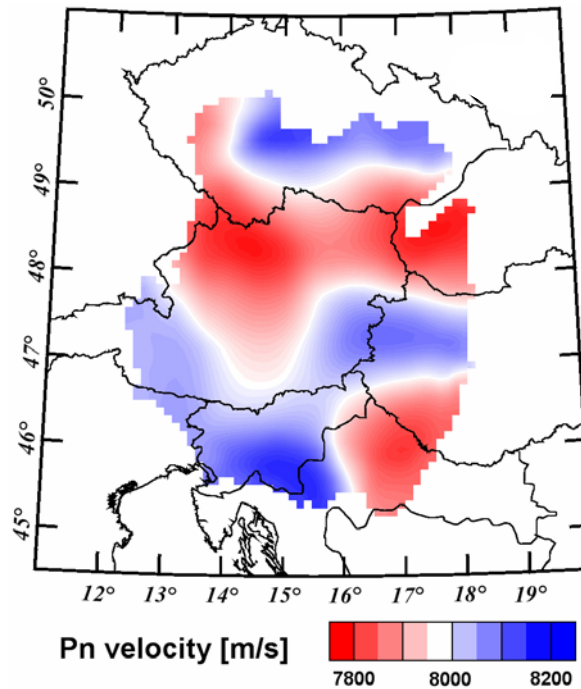


**Figure 5.10.** Pn-velocities within the investigation area are based on the results of CELEBRATION 2000/ALP 2002 experiments [Behm et al. 2007]

### 5.2.2 Travel time computation for pre-defined reflector models

Travel times were computed for several reflector models including reflector depths of **55 km, 60 km, 70 km** and **80 km** – values which scatter about the estimated depth of *Figure 5.7*. Since upper mantle velocities are not well determined, ray tracing was applied to two different velocity gradients, **0.01 s<sup>-1</sup>** and **0.005 s<sup>-1</sup>**.

‘ANRAY’ allows to distinguish between two kinds of ray tracing systems– initial-value ray tracing with given initial values and an arbitrary ray termination point, and two-point ray tracing, where boundary values, such as ray termination coordinates, are introduced. Now, one could try to simply use the two-point ray tracing method by choosing a seismic profile that shows the reflectivity to be investigated and assigning the appropriate shot- and receiver coordinates to the model. This attempt, however, often fails for models with complicated seismic structures due to the non-linearity between the declination angle and the ray termination point. Therefore, two-point ray tracing of travel times may not be feasible for all receivers. This problem can be circumvented when applying **initial-value ray tracing**. The travel times will be computed for a range of azimuth and declination angles with their increment defining the density of coverage of

computed travel times. In cases where the rays do not terminate at specific receivers, interpolation of travel times obtained from nearby rays can be performed.

An important parameter in the initial-value ray tracing application is the choice of the angle increment for both, azimuth and declination, since it strongly influences computation time. A very small increment, e.g. 0.0001, produces a very dense travel time field, which is generally desirable, however, computation time rises significantly. Consequently, a compromise between the choice of angle increment and the density of the travel time field needs to be found.

A very effective way to minimize computation time is to start off with a very rough increment, e.g. 0.1, for both angles, over the whole range of 90°. Afterwards, the travel time field will be plotted in terms of declination angles and the declination range that covers the needed receiver array will be defined (see *Figure 5.11*). Afterwards, the angle increment for the defined range will be enhanced accordingly.

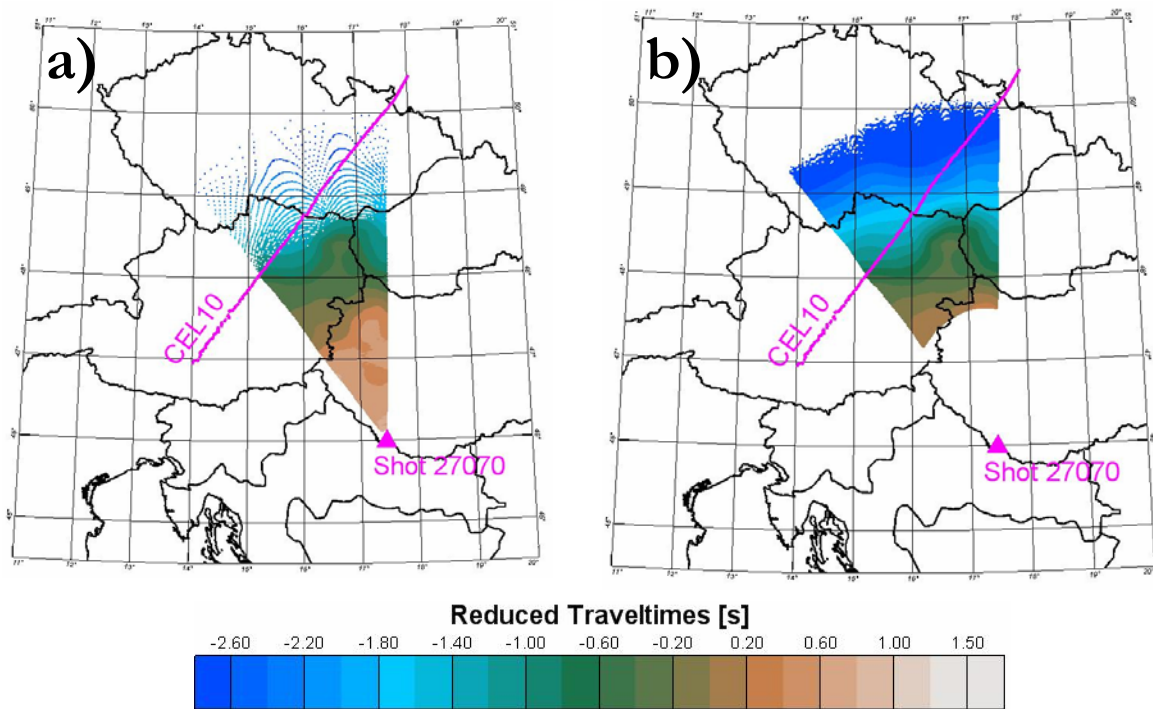


**Figure 5.11.** (a) Travel time computation of shot 27070 towards line CEL10. At short offsets, travel time coverage is sufficient but needs to be improved at greater offsets. Therefore the increment for the declination angle needs to be better adjusted. An improved coverage is obtained in (b); note that the range of the declination angle is adjusted in a way so that short offsets are cut off.

In the first application step, initial-value ray tracing was applied for several reflector depth models (55 km, 60 km, 70 km, 80 km) with a mantle velocity gradient of  $0.01 \text{ s}^{-1}$ . For reflector depths of 55 km and 80 km, travel times were computed for both velocity gradients,  $0.01 \text{ s}^{-1}$  and  $0.005 \text{ s}^{-1}$  (see *Figures 5.12* and *5.13*).

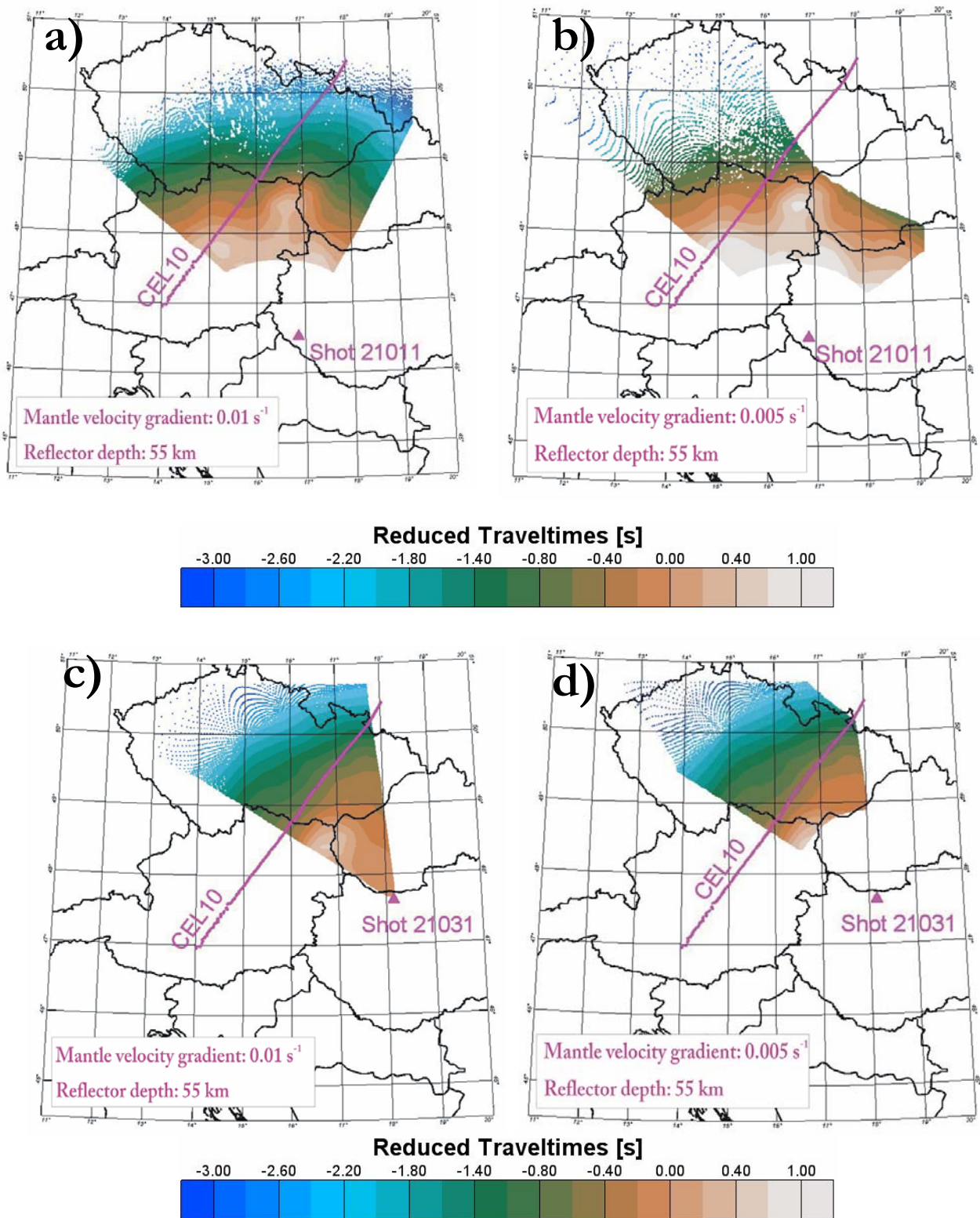


Figure 5.12.

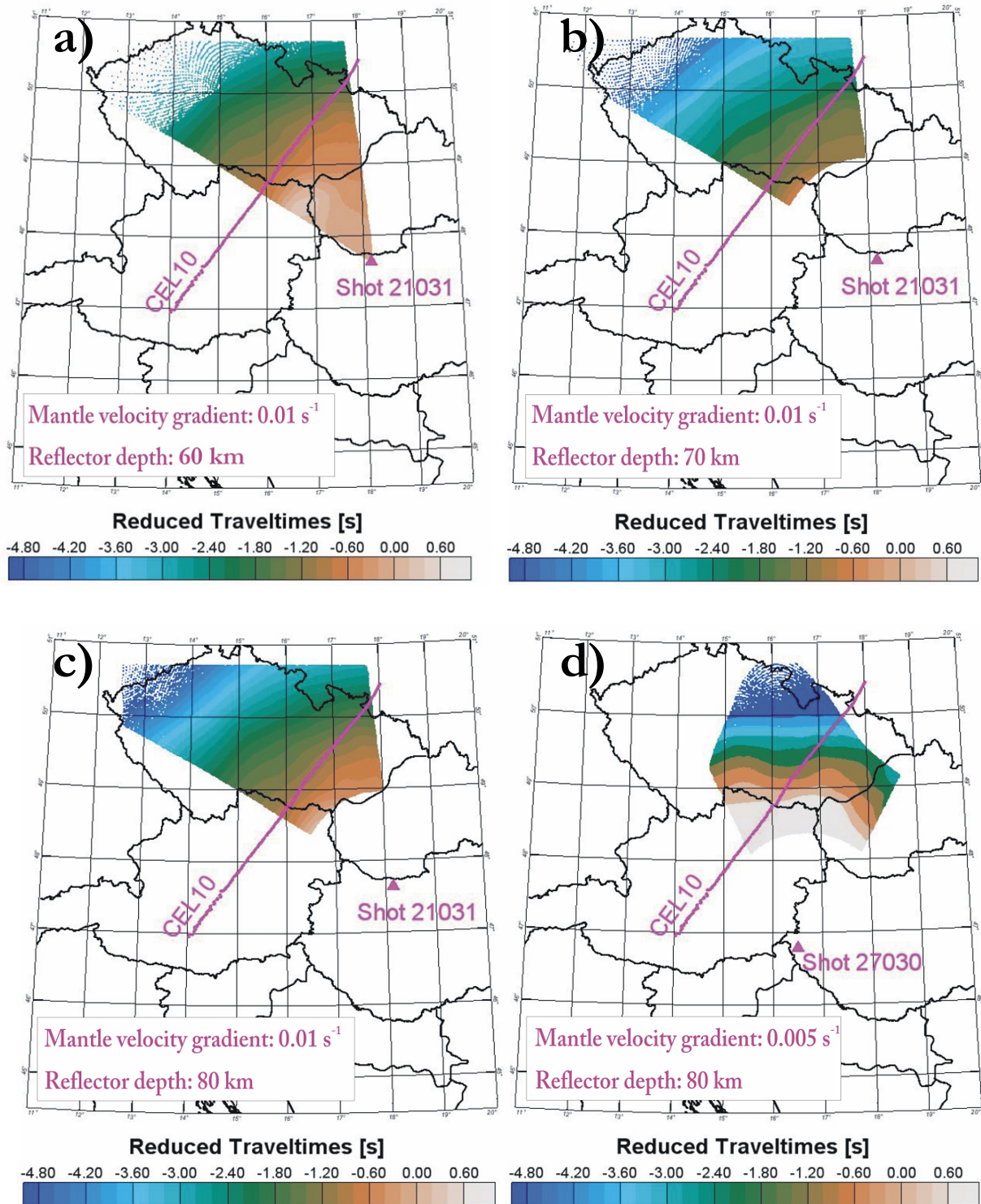
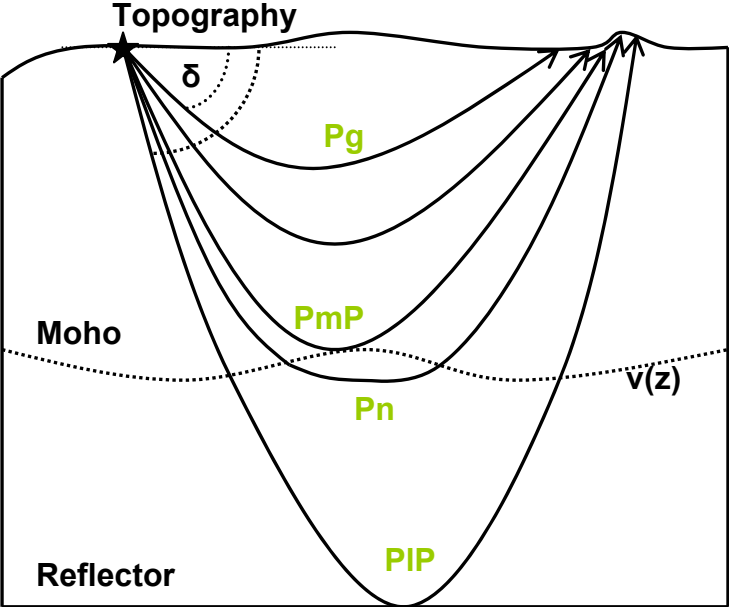


Figure 5.13.

Comparing *Figure 5.12a* (mantle gradient of  $0.01 \text{ s}^{-1}$ ) and *5.12b* (mantle gradient of  $0.005 \text{ s}^{-1}$ ) reveals a lack in the coverage of the travel time field in the latter figure. Due to crustal structures and variations in Moho depth, travel time computation fails in certain areas for a gradient of  $0.005 \text{ s}^{-1}$ . A similar effect is obtained in *Figure 5.13d*.

Reflection travel times of the PIP-phase are obtained at declination angles beyond  $\sim 60^\circ$ . At lower angles ( $< 60^\circ$ ), the ray stays in the first layer (crust) as Pg- and PmP-phase. At a specific angle, the ray reaches the second layer as a diving wave. Increasing the angle further results in the ray penetrating deeper and deeper into the model until it reaches the reflector interface. The travel time field will gradually be built up (illustrated in *Figure 5.14*).



**Figure 5.14.** At low declination angle  $\delta$  the ray propagates as Pg-phase; after a specific angle, the ray penetrates into the second layer, first as a Pn-phase, later as PIP.

The interpolated travel time fields of *Figures 5.12* and *5.13* now enable travel time sampling onto specific receivers. Synthetic travel times are now used to support improved travel time picking, since accurate picks are crucial for the subsequent inversion application. Furthermore, modelled travel times help to better estimate the depth of the reflector.

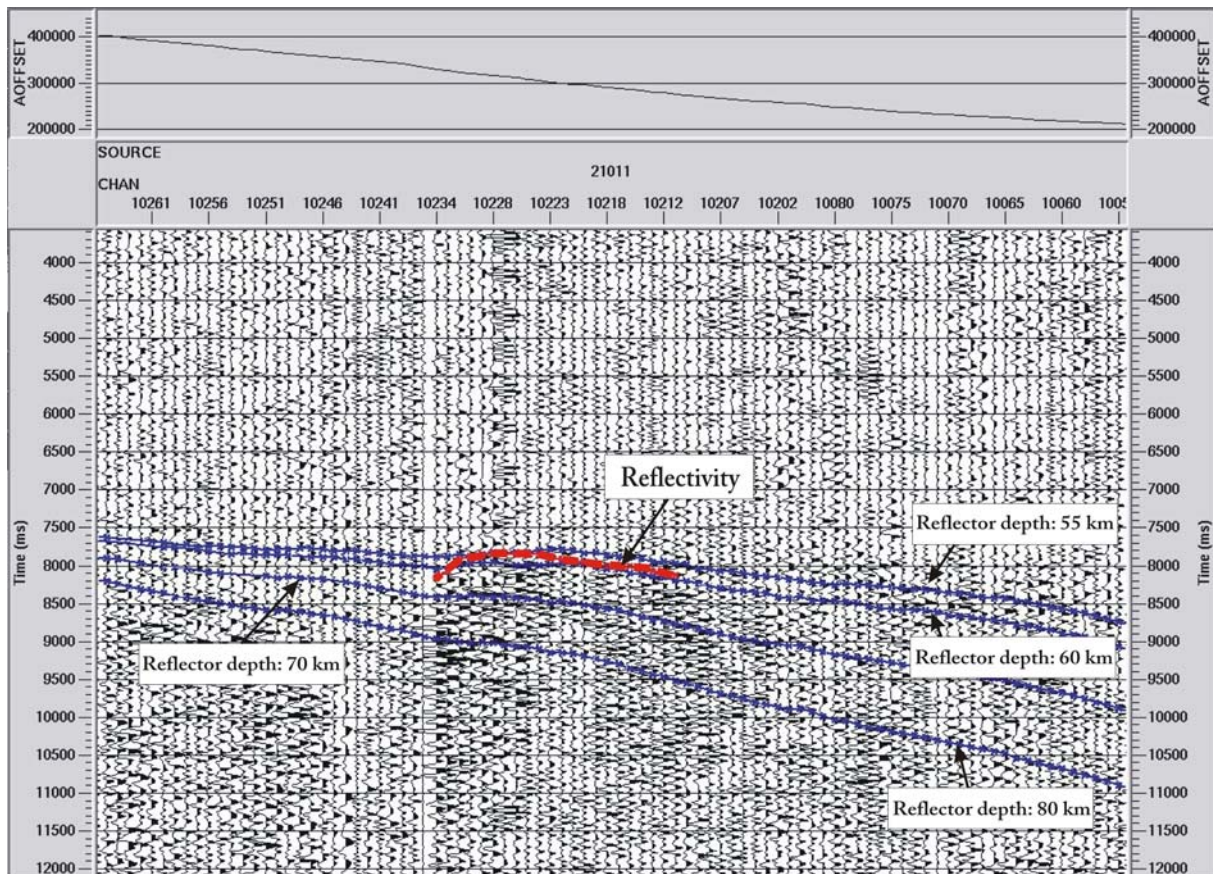


**Figure 5.15.** Synthetic travel times for various depths based on a mantle velocity gradient of  $0.01 \text{ s}^{-1}$  are introduced into the seismic section in order to better determine the course of reflectivity (red).

*Figure 5.15* gives an example of synthetic travel times computed for different reflector depths and picked reflective travel times. Modelled travel times based on reflector depths of 55 km and 60 km coincide partly with observed reflectivity and give a rough clue about the course of picking. The reflector depth for this very section can be estimated between a depth of 55 km and 60 km. Travel times in *Figure 5.15* are based on a mantle velocity gradient of  $0.01 \text{ s}^{-1}$ .

*Figure 5.16* demonstrates the influence of varying mantle velocity gradients ( $0.01 \text{ s}^{-1}$  and  $0.005 \text{ s}^{-1}$ ) on travel times. Similar travel times are obtained for reflector models of 55 km ( $0.005 \text{ s}^{-1}$ ) and 60 km ( $0.01 \text{ s}^{-1}$ )

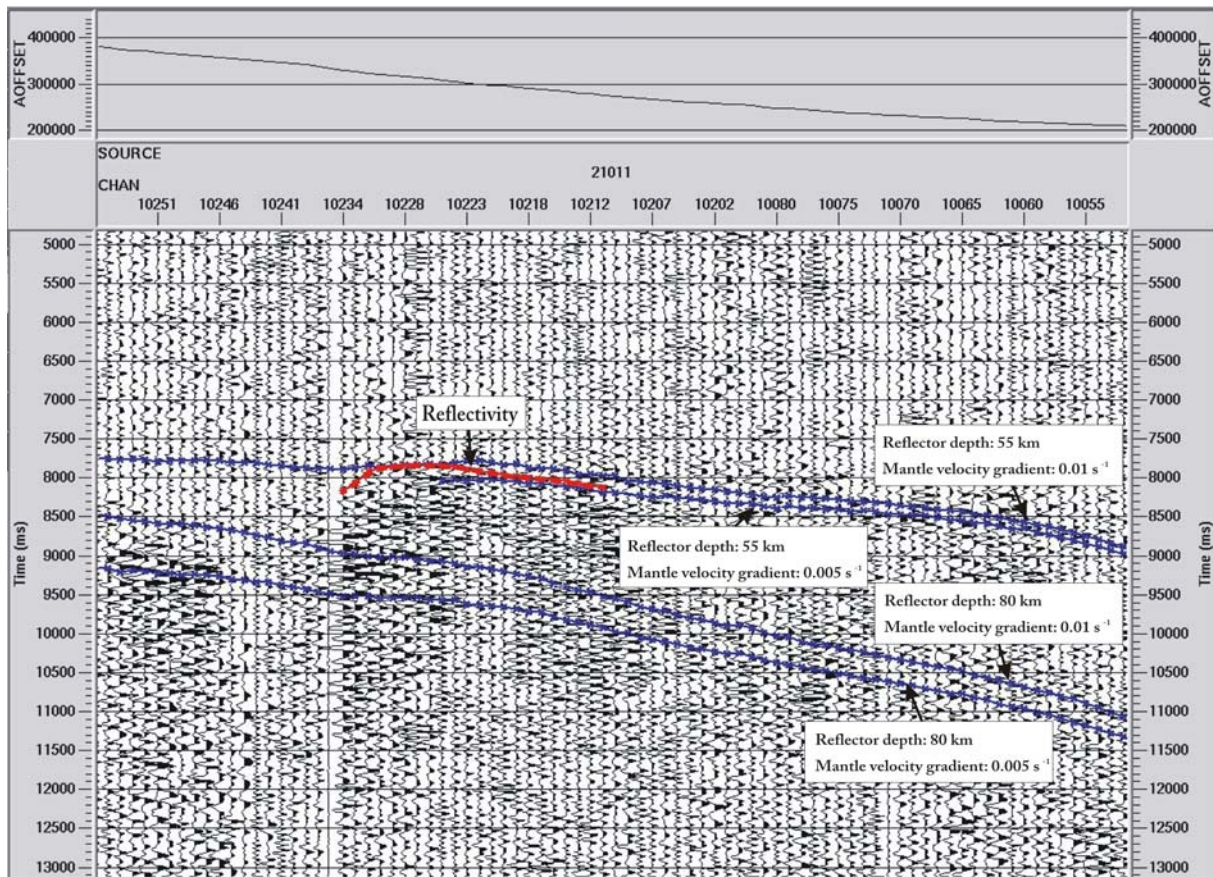


Figure 5.16. Comparison between mantle velocity gradients  $0.01 \text{ s}^{-1}$  and  $0.005 \text{ s}^{-1}$  for reflector depths of 55 km and 80 km.

In general, there are several possible reflector depth models that result in similar travel times – from lower depths with lower gradients to greater depths with higher gradients – the decisive factors are the **mantle velocity gradient** and the **depth of the reflector**. Thus, it is difficult to more accurately estimate the reflector depth as long as mantle velocities are poorly constrained.

Travel times related to reflector depths of 70 km and 80 km are long on other sections too and can therefore be excluded as possible solutions. A mantle velocity gradient much greater than  $0.01 \text{ s}^{-1}$  would be needed to yield a coincidence with picked travel times. Such high mantle gradients are very unlikely in the uppermost mantle.

As a comparison, velocity data of the Preliminary Earth Model (PREM) by *Dziewonski & Anderson (1981)* refer to an upper mantle velocity gradient of  $\sim 0.0006 \text{ s}^{-1}$ . Their model, however, may lack resolution in the uppermost layers and thus could cause these deviating values in velocity gradients.



## 5.3 Travel time computation based on the finite difference approach

---

In the previous section, travel times were computed by applying the ray tracing-based ‘ANRAY’ in order to facilitate travel time picking. Before the updated travel time picks are used for actual inversion, forward modelling of travel times with finite differences – just as with ‘ANRAY’ – will be carried out. Afterwards, both approaches will be compared.

### 5.3.1 Velocity parameterization

The velocity model extends 600 km to the east, 660 km to the north and 108 km in z-direction. Since all the interfaces, including the topography, need to be defined within this model box, a vertical shift of 8 km was applied. Thus, the depth value of 8 km represents the original zero-level (see *Appendix A.1*). The grids themselves represent cubes with the velocities defined at their nodes. The grid spacing has to be adjusted according to the complexity of the velocity distribution. Since the velocity distribution within the investigation area is relatively smooth without abrupt changes, except for the Moho discontinuity, a grid spacing of 2 km has been used during the first computations. A grid spacing of 4 km, however, shows a greater accuracy (travel time difference between both grid spacings:  $\sim 150$  ms) when compared to modelled travel times with ‘ANRAY’. Thus, all subsequent computations are based on a grid spacing of 4 km. The crust velocity distribution equals that used for travel time computation with ‘ANRAY’. Travel time modelling was carried out for mantle velocity gradients of  $0.01 \text{ s}^{-1}$ ,  $0.005 \text{ s}^{-1}$  and  $0.002 \text{ s}^{-1}$ .

### 5.3.2 Introduction of interfaces

Interfaces such as the crust-mantle boundary (Moho discontinuity), cannot be defined in terms of depth, but need to be introduced in terms of velocities. Since an interface is defined as an abrupt change in velocity, it is to be specified by assigning velocity values to grid points directly above and below the interface (*Figure 5.17*). The velocity values in between the grid cells are obtained through linear interpolation taking the values at the surrounding grid points. Subsequently, the interface can no longer be regarded as a sharp boundary between two layers of different seismic properties, but as a transition zone to higher/lower velocities. In our case, the Moho discontinuity is an interface which represents a jump in velocity from lower crustal velocities (6.5 – 7.0 km/s) to  $\sim 8$  km/s. It is obvious that the smaller the grid spacing the more accurate the interface can be represented. The drawback is a rise in computation time when smaller grid cells are chosen.

The modified version by *Hole* especially treats the inversion of reflection travel times. A reflector interface, unlike the Moho interface, can be introduced into the system much more easily, just by defining its depth in the input file (see *Appendix A.1*).

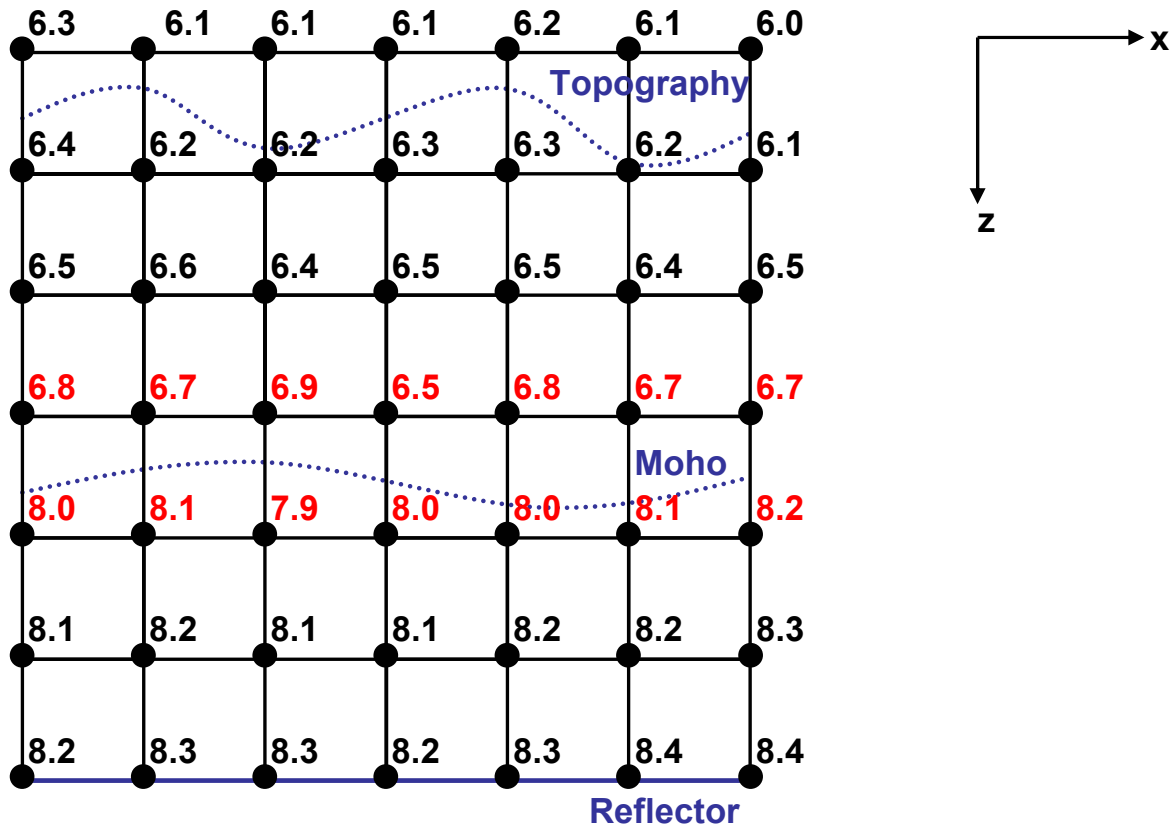


**Figure 5.17.** The interface representing the Moho is no longer defined as a boundary between two layers of different velocities, but through velocities at the grid points immediately above and below that interface (values marked in red). A velocity jump from  $\sim 6.7$  km/s to  $\sim 8.0$  km/s takes place. Velocities between the grid points are linearly interpolated.

### 5.3.3 Forward modelling of travel times for pre-defined reflector models

Based on the finite difference approach, travel times have been forward modelled for simply defined horizontal reflectors (reflector depths of 55 km and 80 km). For mantle velocity gradients, the values  $0.01 \text{ s}^{-1}$  and  $0.005 \text{ s}^{-1}$  were used. The resulting travel times for both gradients and a reflector depth of 55 km are shown in *Figure 5.18*. Comparing both gradients reveals a travel time difference of  $\sim 200 - 300 \text{ ms}$ .

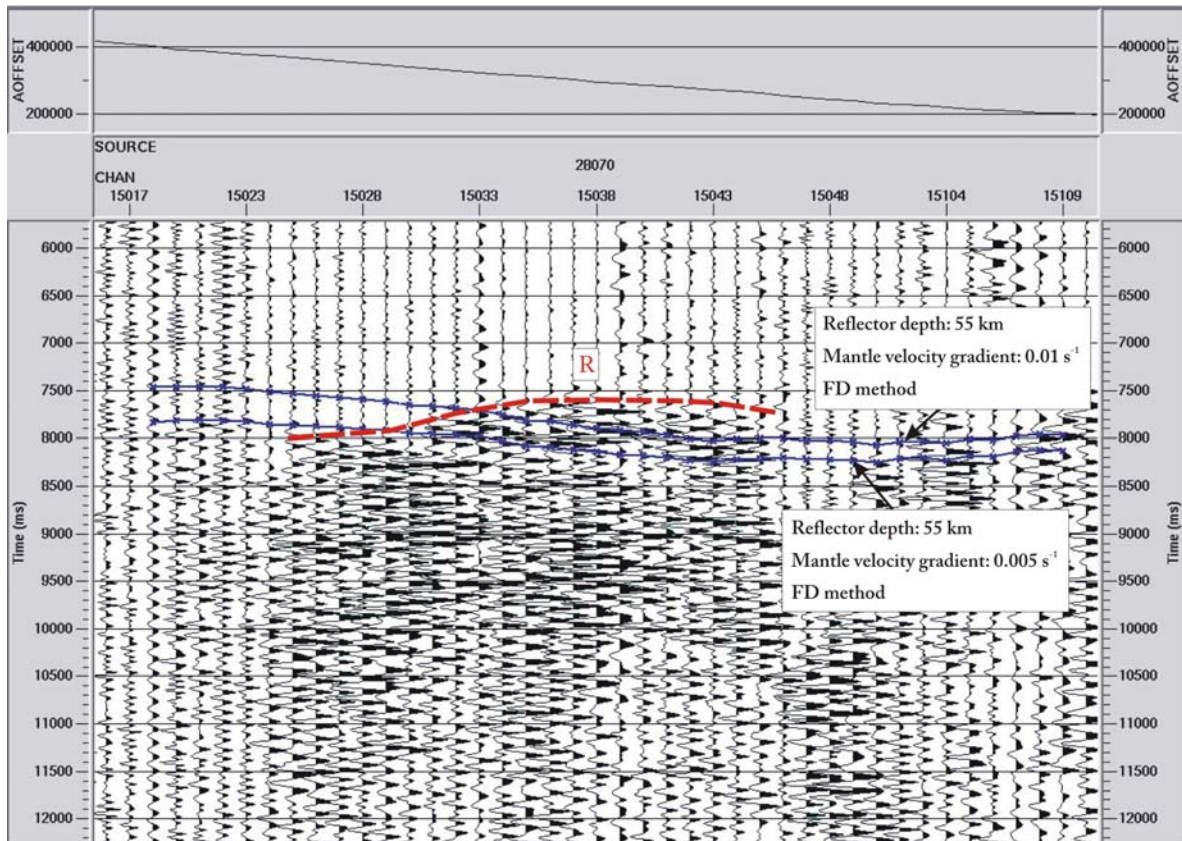


**Figure 5.18.** Travel times modelled with a mantle velocity gradient of  $0.005 \text{ s}^{-1}$  are 200 – 300 ms longer compared to travel times based on a velocity gradient of  $0.01 \text{ s}^{-1}$ .

### 5.3.4 Comparison with 'ANRAY'-computed travel times

Comparing both approaches – ray tracing-based travel time computation and finite difference-based travel time computation – shows a difference in travel times of  $\sim 200$  ms based on a model with a reflector depth of 55 km and a mantle velocity gradient of  $0.005 \text{ s}^{-1}$  (Figure 5.19). The reason may be found in the inaccurate definition of the crust-mantle boundary (see section 5.3.2) in the finite difference application which may result in a distortion of travel times. However, an accurate analysis is beyond the scope of this thesis.

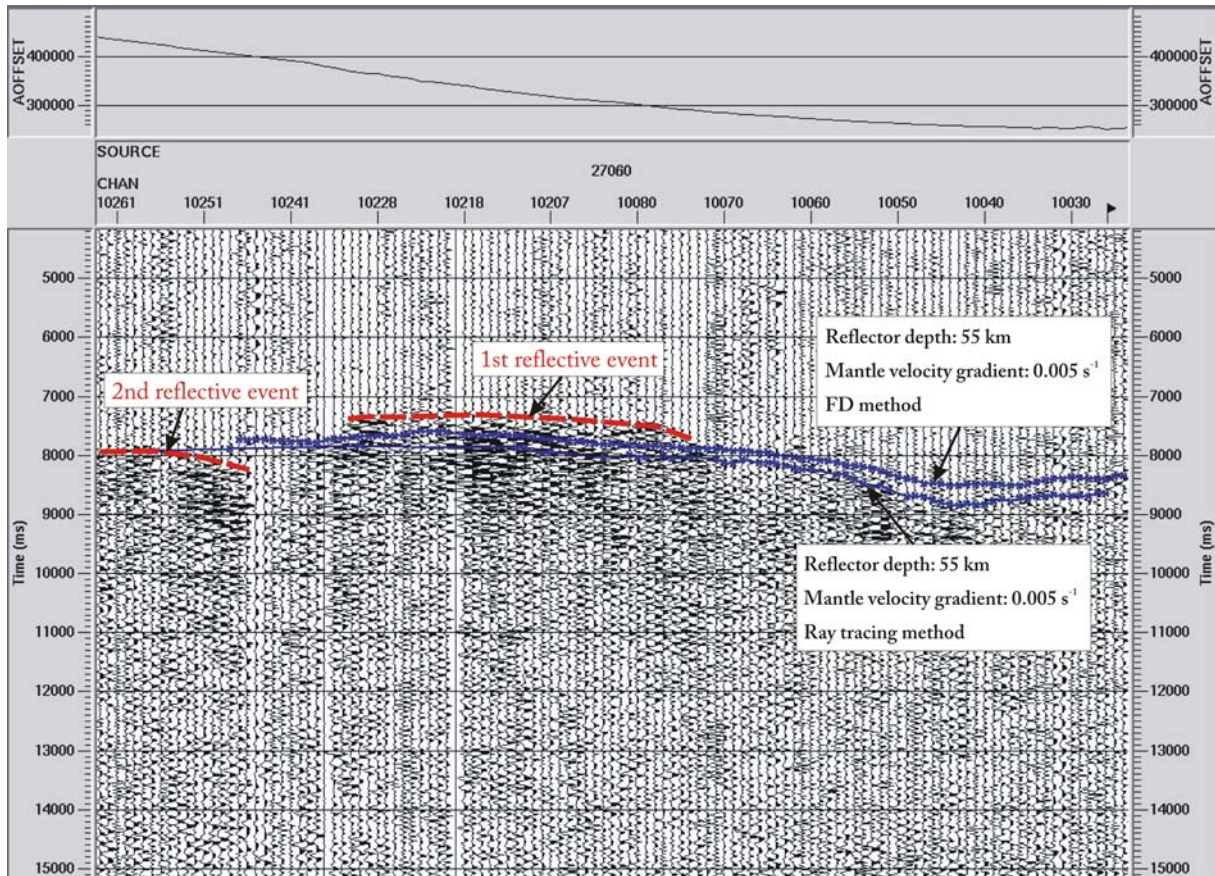


**Figure 5.19.** Comparison of travel times computed with finite differences (FD) and with ray tracing indicates a difference in travel times of  $\sim 200$  ms.

## 5.4 Inversion results

---

The performance of the inversion process depends on accurate travel time picks. Thus, several picking updates were carried out, especially since some of the reflective events are obtained in areas with lower signal-noise ratio, which makes accurate picking difficult. Uncertainty in these cases ranges approximately between 100 and 200 ms. Erroneous picks may result in artefacts after inversion, such as abrupt changes in depth among neighbouring values.

After a first inversion step, the newly calculated travel times were compared with the picked travel times and those that differed significantly were excluded from the next inversion steps. Reduction of travel time data, however, has the downside of yielding a less dense coverage.

Finally, 1078 travel times were used for the inversion. The data set consists of 23 shots (*Table 5.3b*) with recording profiles CEL01, CEL07, CEL09, CEL10 and CEL15. Inversion was carried out for three mantle velocity gradients -  $0.01 \text{ s}^{-1}$ ,  $0.005 \text{ s}^{-1}$  and  $0.002 \text{ s}^{-1}$ . The grid cell size is 4 km for each inversion. Three iterations were carried out for each inversion step. Smoothing parameters have been chosen as 31 - 21 -11 (see *Appendix A.1* for explanation). That means, smoothing extends over 120 km in x- and y-directions during the first iteration, 80 km during the second iteration and 40 km during the final one. The extent of smoothing was adapted to the number of travel times and since that number is relatively small, inversion was carried out with a comparably large smoothing extent to better compensate deviations in travel times. One inversion run was carried out with smoothing parameters of 13 -11 -8 (48 x 48 km, 40 x 40 km and 28 x 28 km).

The **initial reflector** is situated at a depth of **55 km**. Applying a z-shift (see *Appendix A.1*) of 8 km changes the reflector depth to 63 km (*Table 5.3c*). The appropriate parameters have been set in the control file (“<prefix>.ri”) in *Table 5.3a*.

(a)

```

# INPUT FILES -----
set shfile=newpick.his
set pars=../pars
set v1dfile=litho55.v1d
set r1dfile=litho55.r1d
set pref=newpick
# GENERAL -----
set i2d=0
set step=1
set floatsrc=1
set vred=999999999999.0
set xshift=0.
set zshift=8.
set cosmin=0.1
# DZGRID -----
set nsmooth=100
set c=1.
set nrng=300
set idisc=0
set zcmin=20.
set zcmax=100.
# SMOOTH -----
set mvan=3
set mvax=(31 21 11)
set mvay=(31 21 11)
set mvaz=(1 1 1)
set dflag=0

```

(b)

Shot ID	x-coordinate [km]	y-coordinate [km]	z-coordinate [km]
27020	384.17900	245.31900	0.23200
27030	394.90100	222.45800	0.23000
21010	422.09800	194.22700	0.24000
21011	422.09800	194.22700	0.24000
27050	436.40400	172.77400	0.22000
27060	455.57900	151.07700	0.14000
27070	469.56500	135.67900	0.12000
21020	474.27900	268.83700	0.31000
20020	228.89100	269.38700	1.41000
20030	243.40700	292.64400	1.44800
20060	342.27500	423.70400	0.35000
20080	412.81800	518.70300	0.61900
20081	412.84500	518.70400	0.61900
20100	467.79400	590.35100	0.42800
28030	423.31800	308.08000	0.15000
28040	452.29800	292.44600	0.12800
28060	486.75100	248.43000	0.24500
28070	507.87800	225.01000	0.16800
28080	522.83000	209.91900	0.13000
28090	547.73200	178.75900	0.14200
25010	566.53100	153.36200	0.11000
21030	516.95500	319.93200	0.13000
21031	516.95500	319.93200	0.13000

(c)

```

vel1d << END
ro.000.1d
ro.000.ref
4
0.0 0.0 0.
600. 660. 0.0
1
0. 63.
END

```

**Table 5.3.** (a) Control file 'litho55.ri' with links to the input files; (b) file 'newpick.his' containing 22 shots used for inversion; (c) file 'litho55.r1d' containing reflector specifications.

In terms of rms-travel time errors, the file '<prefix>.itr' gives a good overview of how well the system performs for the different velocity gradients. Travel time residuals of all three models are presented in *Table 5.4*.

After the first inversion step, the misfit for the model based on the mantle velocity gradient of  $0.005 \text{ s}^{-1}$  is lowest with 0.32 s, compared to 0.36 s and 0.37 s for the other models. After the third iteration, rms-travel time errors decline to 0.30 s and 0.29 s for the models with velocity gradients of  $0.005 \text{ s}^{-1}$  and  $0.002 \text{ s}^{-1}$ , whereas the model based on the mantle velocity gradient of  $0.01 \text{ s}^{-1}$  shows very little difference in rms-travel time errors with 0.35 s. Compared to the other two models, inversion based on the velocity gradient  $0.01 \text{ s}^{-1}$  shows definitely the poorest performance. The travel time error is already quite high after the first iteration and does not improve significantly after three iterations. This is an indication that a mantle velocity gradient of  $0.01 \text{ s}^{-1}$  is too high. Thus, further investigations concentrate on the other two velocity gradients.

In order to determine the influence of a smaller smoothing extent on rms-travel time errors, inversion was repeated for the model based on the mantle velocity gradient of  $0.005 \text{ s}^{-1}$ , this time taking smoothing parameters of 13 -11 -8. Since the structure is less strongly smoothed, the rms-travel time errors are expected to be lower. This is indeed the case, with rms-errors starting at 0.32 s and declining to 0.27 s after three iterations. Although showing a slight improvement compared to the larger smoothing extent from above, the rms-travel time error is still comparably high. This allows the assumption that travel time errors will not improve significantly for other smoothing parameters either and tend to range between 0.25 s and 0.30 s.

<b>(a) Mantle velocity gradient: <math>0.01 \text{ s}^{-1}</math></b>				
No. of iterations	smoothing parameter		reflector file	rms-traveltime residual [s]
1	31	31	ro.001.ref	0.36
2	21	21	ro.002.ref	0.34
3	11	11	ro.003.ref	0.35

<b>(b) Mantle velocity gradient: <math>0.005 \text{ s}^{-1}</math></b>				
No. of iterations	smoothing parameter		reflector file	rms-traveltime residual [s]
1	31	31	ro.001.ref	0.32
2	21	21	ro.002.ref	0.31
3	11	11	ro.003.ref	0.30

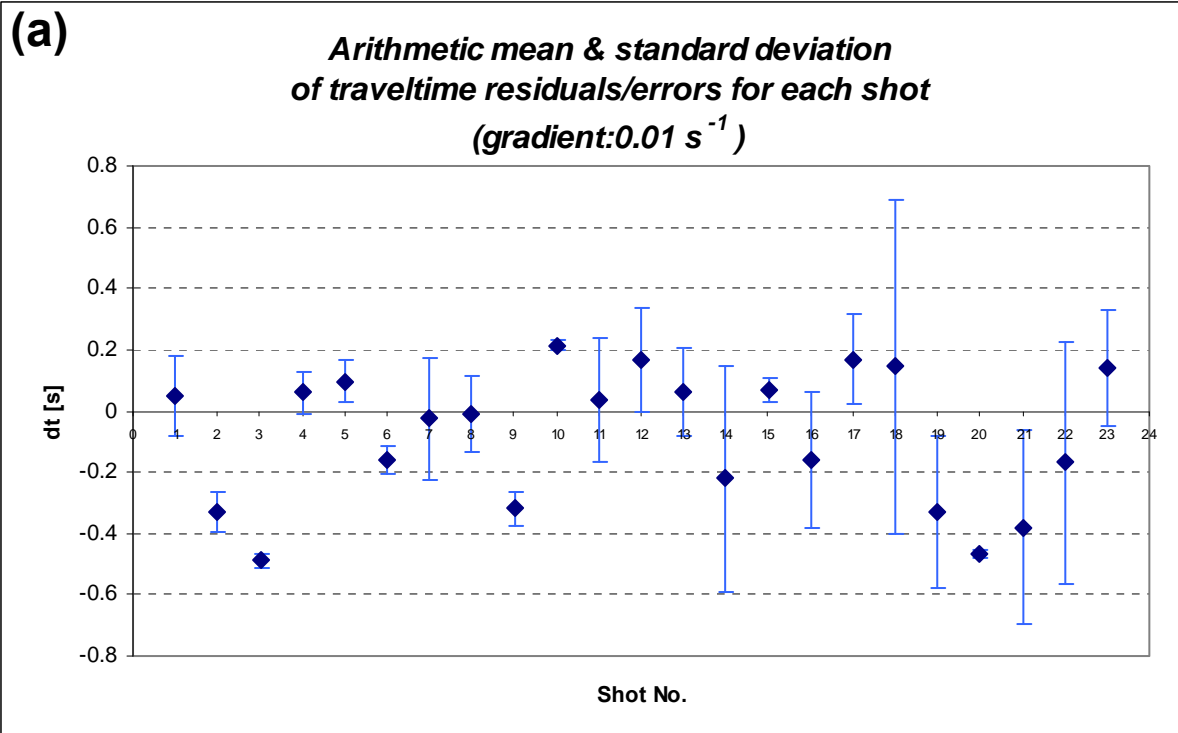
  

<b>(c) Mantle velocity gradient: <math>0.002 \text{ s}^{-1}</math></b>				
No. of iterations	smoothing parameter		reflector file	rms-traveltime residual [s]
1	31	31	ro.001.ref	0.37
2	21	21	ro.002.ref	0.33
3	11	11	ro.003.ref	0.29

<b>(d) Mantle velocity gradient: <math>0.005 \text{ s}^{-1}</math></b>				
No. of iterations	smoothing parameter		reflector file	rms-traveltime residual [s]
1	13	13	ro.001.ref	0.32
2	11	11	ro.002.ref	0.29
3	8	8	ro.003.ref	0.27

**Table 5.4.** Rms-travel time residuals for various mantle velocity gradients. Note the change in smoothing parameters in (d).



Shot No.	1	2	3	4	5	6	7	8	9	10	11	12
Shot ID	20020	20030	20060	20080	20081	20100	21010	21011	21020	21030	21031	25010
No. of picks	15	7	3	8	11	12	11	44	13	3	32	170
	13	14	15	16	17	18	19	20	21	22	23	
	27020	27030	27050	27060	27070	28030	28040	28060	28070	28080	28090	
	25	67	6	124	138	43	60	7	99	91	89	

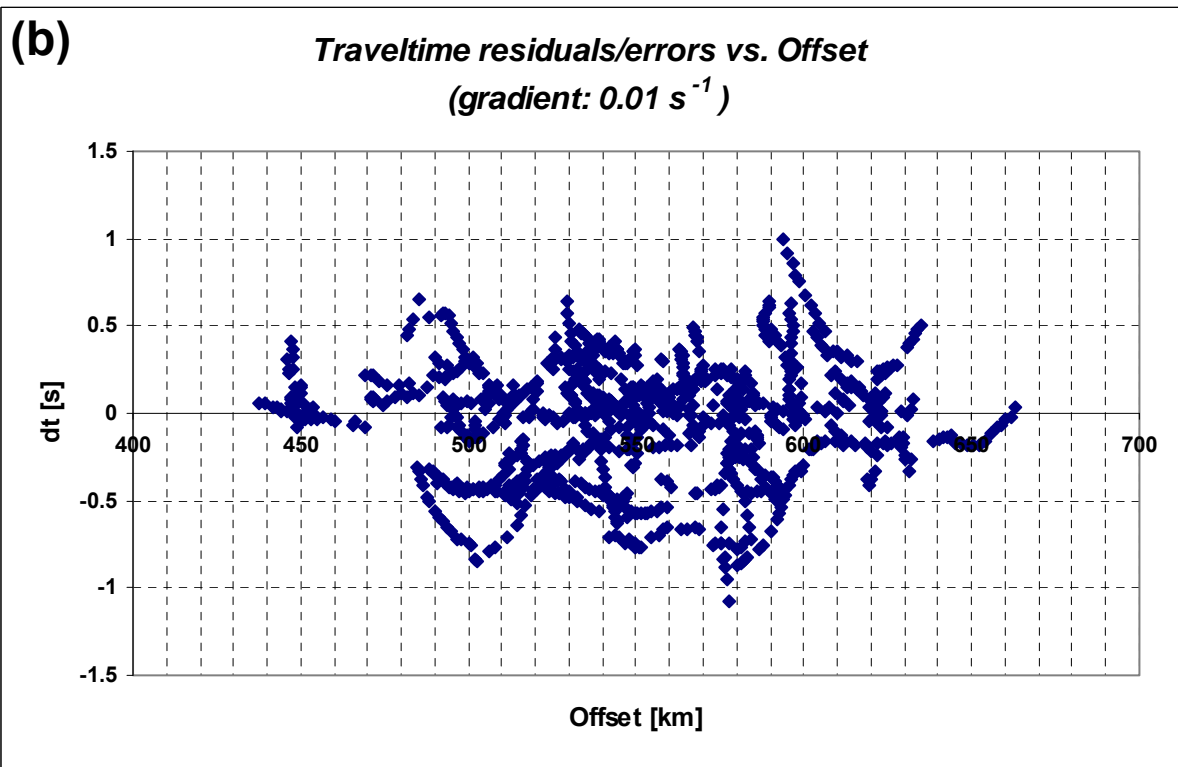
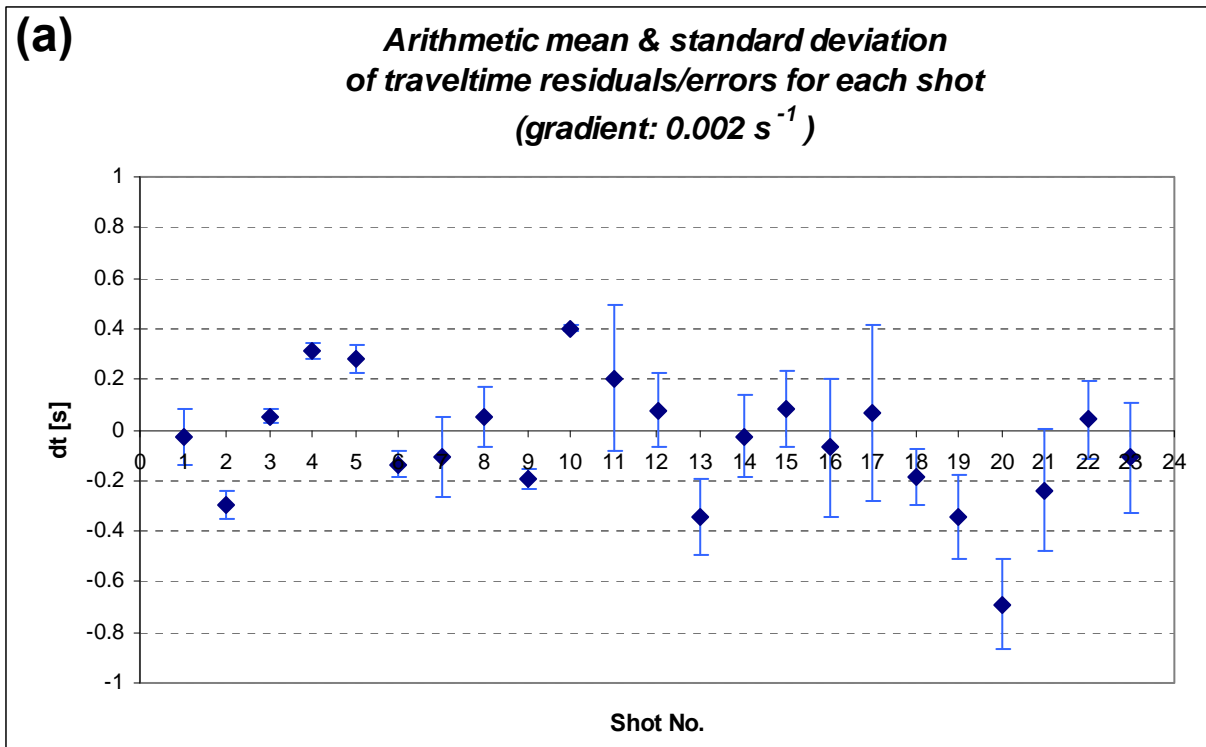


Figure 5.20.





Shot No.	1	2	3	4	5	6	7	8	9	10	11	12
Shot ID	20020	20030	20060	20080	20081	20100	21010	21011	21020	21030	21031	25010
No. of picks	15	7	3	8	11	12	11	44	13	3	32	170
	13	14	15	16	17	18	19	20	21	22	23	
	27020	27030	27050	27060	27070	28030	28040	28060	28070	28080	28090	
	25	67	6	124	138	43	60	7	99	91	89	

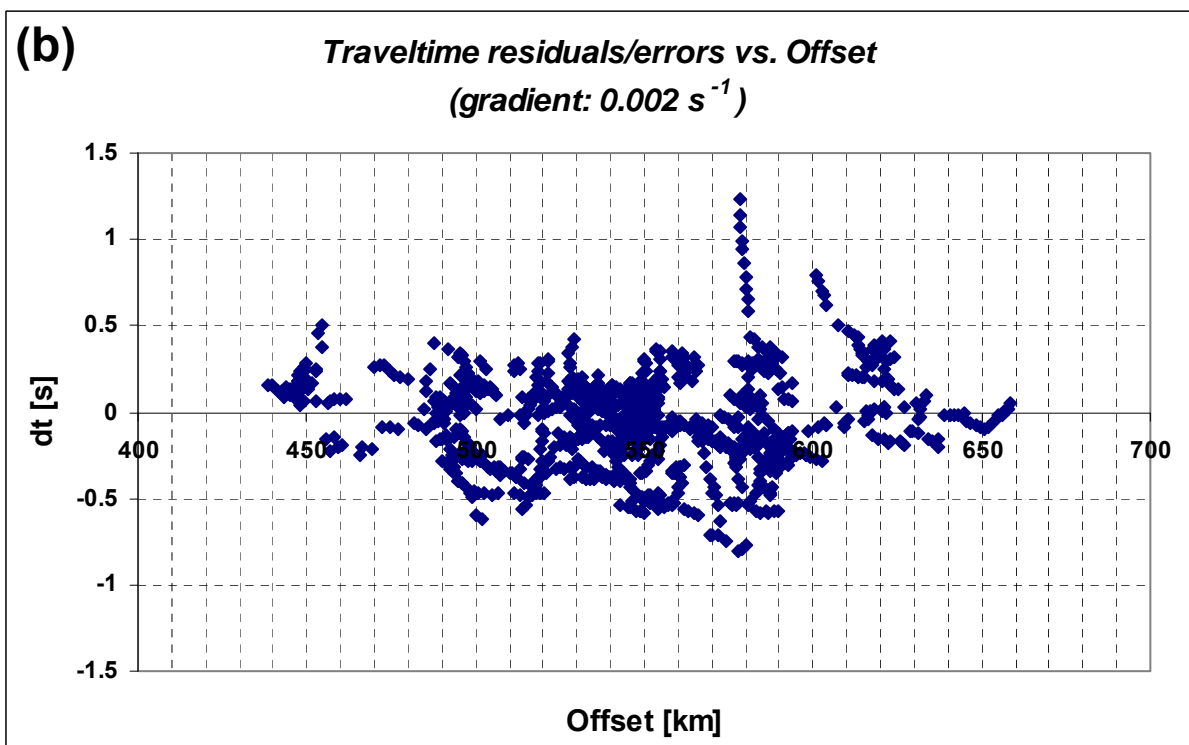
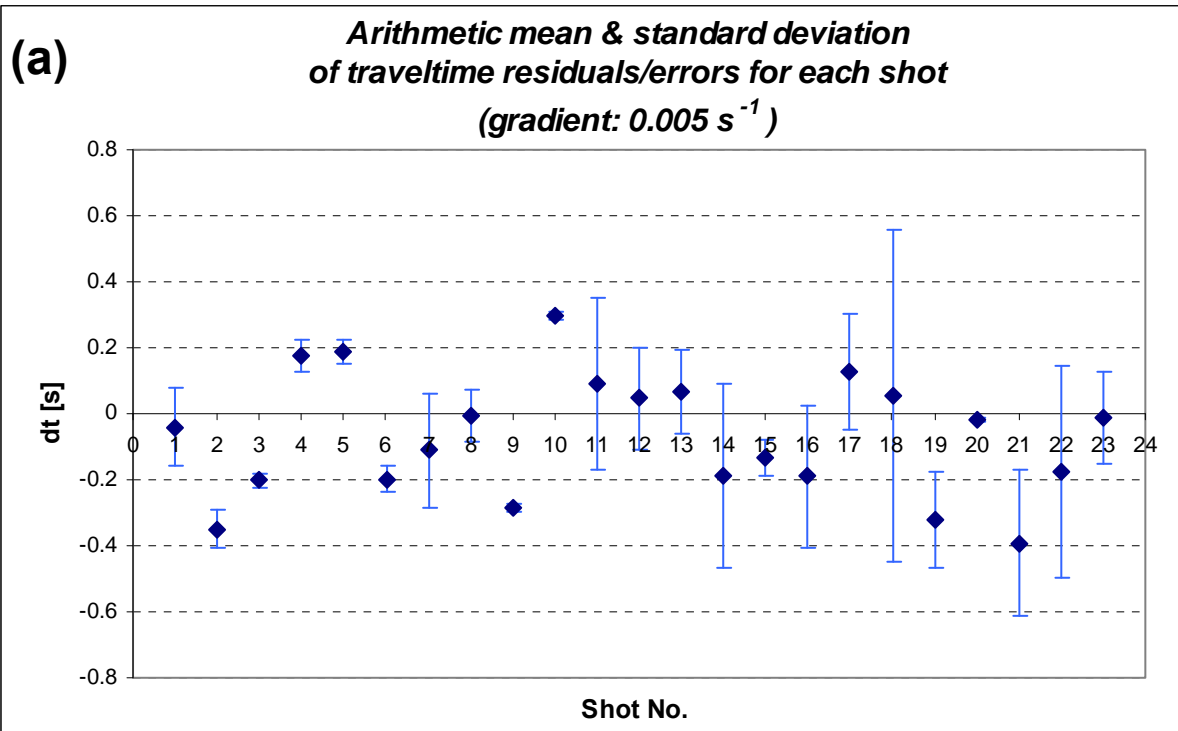


Figure 5.21.



Shot No.	1	2	3	4	5	6	7	8	9	10	11	12
Shot ID	20020	20030	20060	20080	20081	20100	21010	21011	21020	21030	21031	25010
No. of picks	15	7	3	8	11	12	11	44	13	3	32	170
	13	14	15	16	17	18	19	20	21	22	23	
	27020	27030	27050	27060	27070	28030	28040	28060	28070	28080	28090	
	25	67	6	124	138	43	60	7	99	91	89	

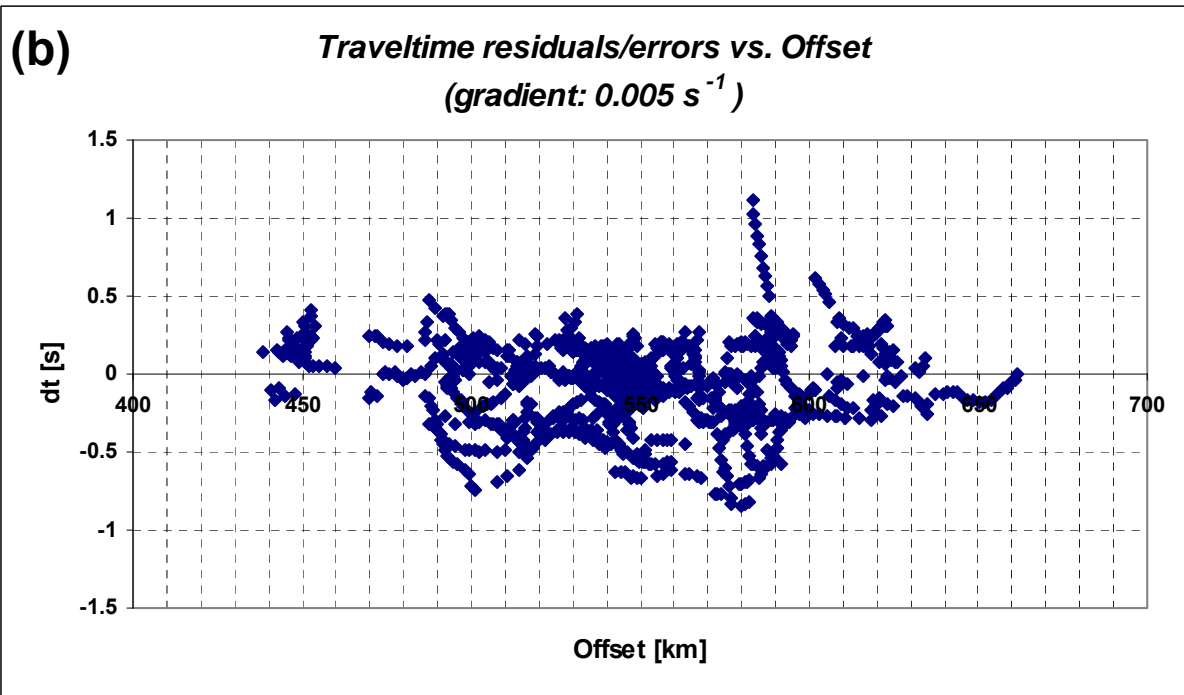
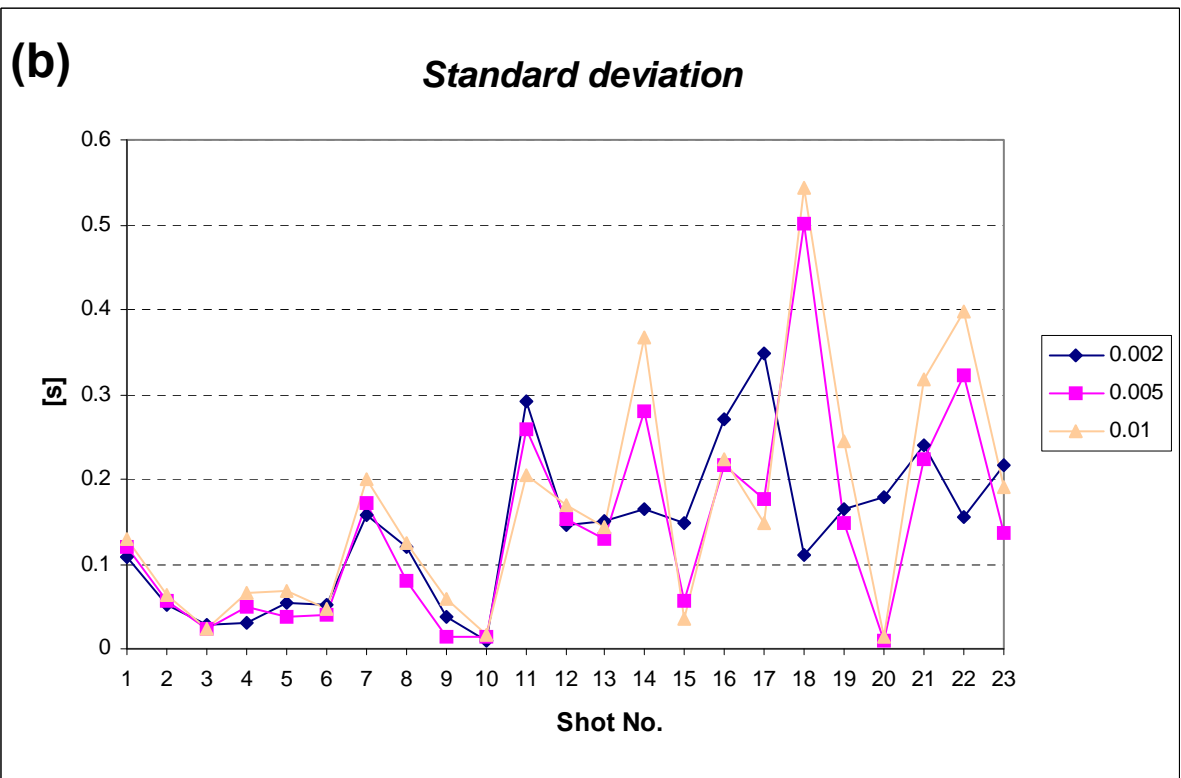
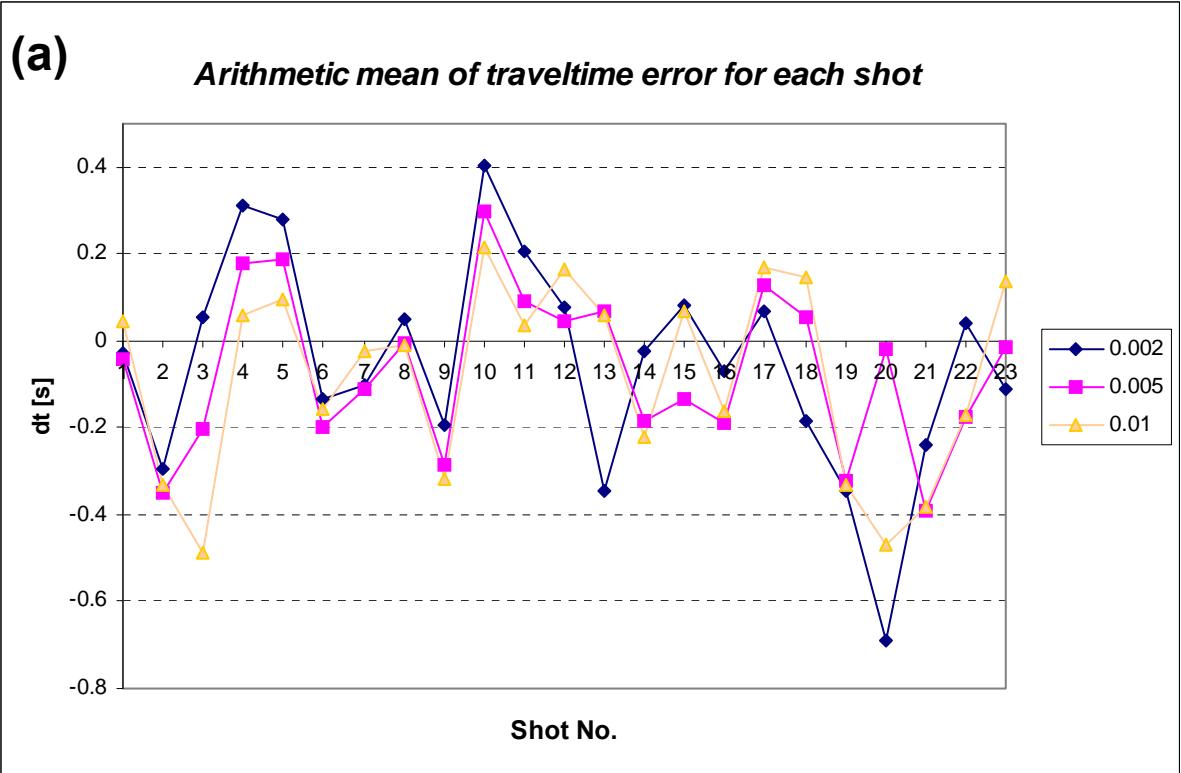


Figure 5.22.



<b>Shot No.</b>	1	2	3	4	5	6	7	8	9	10	11	12
<b>Shot ID</b>	20020	20030	20060	20080	20081	20100	21010	21011	21020	21030	21031	25010
<b>No. of picks</b>	15	7	3	8	11	12	11	44	13	3	32	170
	13	14	15	16	17	18	19	20	21	22	23	
	27020	27030	27050	27060	27070	28030	28040	28060	28070	28080	28090	
	25	67	6	124	138	43	60	7	99	91	89	

Figure 5.23. Travel time errors for each shot are listed in (a). (b) shows the appropriate standard deviations.

Rather than taking the rms-travel time error, it may be more illustrative to display the travel time misfits for each single shot, as shown in *Figures 5.20a, 5.21a, 5.22a and 5.23*. Arithmetic mean errors of all three gradients alternate between 0.4 s and -0.7 s (*Figure 5.23a*). In these cases, the mantle velocity gradients are partly too high (positive values) and too low (negative values). The misfit in travel times for the velocity gradient of  $0.01 \text{ s}^{-1}$  is large for shots 20060/21030/28040/28060/28070 ranging between -0.5 s and 0.2 s. Taking the velocity gradient of  $0.005 \text{ s}^{-1}$ , errors are large for shots 20030/21030/28070 with misfits of  $\pm 400 \text{ ms}$ . The velocity gradient of  $0.002 \text{ s}^{-1}$ , which shows the lowest misfit in terms of rms-values, reaches its maximum error at shots 21030 and 28060 with 0.4 s and -0.7 s respectively.

In terms of standard deviations, velocity gradients of  $0.01 \text{ s}^{-1}$  and  $0.005 \text{ s}^{-1}$  show similar values, whereas the values for the velocity gradient of  $0.002 \text{ s}^{-1}$  differ at specific shots. Standard deviations for shots situated in the Pannonian Basin (Shot No. 7 - 23) are significantly higher than those situated along CEL10 (Shot No. 1 - 6). This could be due to the fact that the velocity structure in the Pannonian Basin is poorly constrained. Furthermore, a correlation between the number of travel time picks and standard deviation can be recognized – the more travel times, the higher the standard deviation and vice versa. Except for shot 21010, standard deviations for shots with less than 20 travel time picks range between 0 and 0.1 s.

Plotting travel time errors against offset (*Figures 5.20b, 5.21b and 5.22b*) indicates no significant offset dependency.

Factors that may cause relatively high rms-travel time errors include the picking of wrong phases and therefore wrong travel times, poorly constrained crustal velocities in the sedimentary basins and trigger errors that are supposed to have occurred in the Pannonian Basin which result in a time shift.

After three iterations, the following three reflector depth models (Figure 5.24, 5.25 and 5.26) were created.

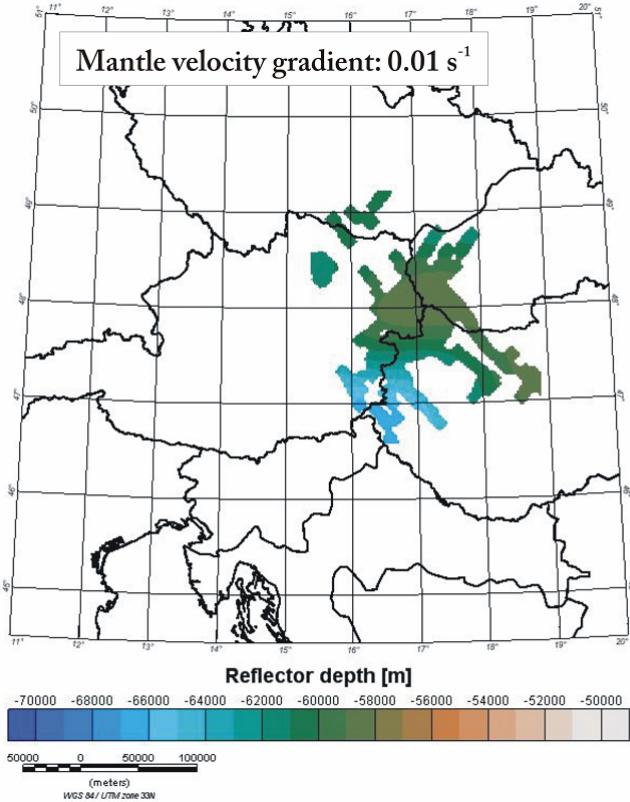


Figure 5.24.

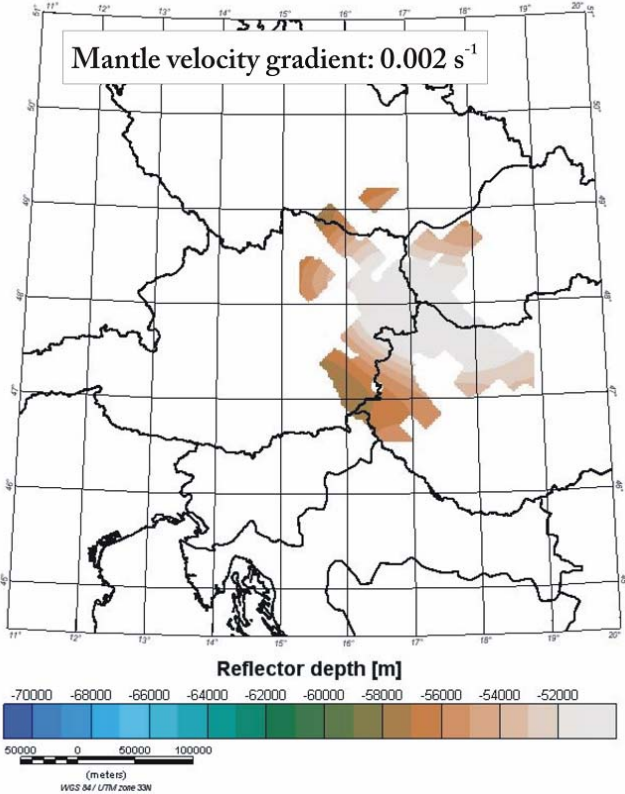


Figure 5.25.

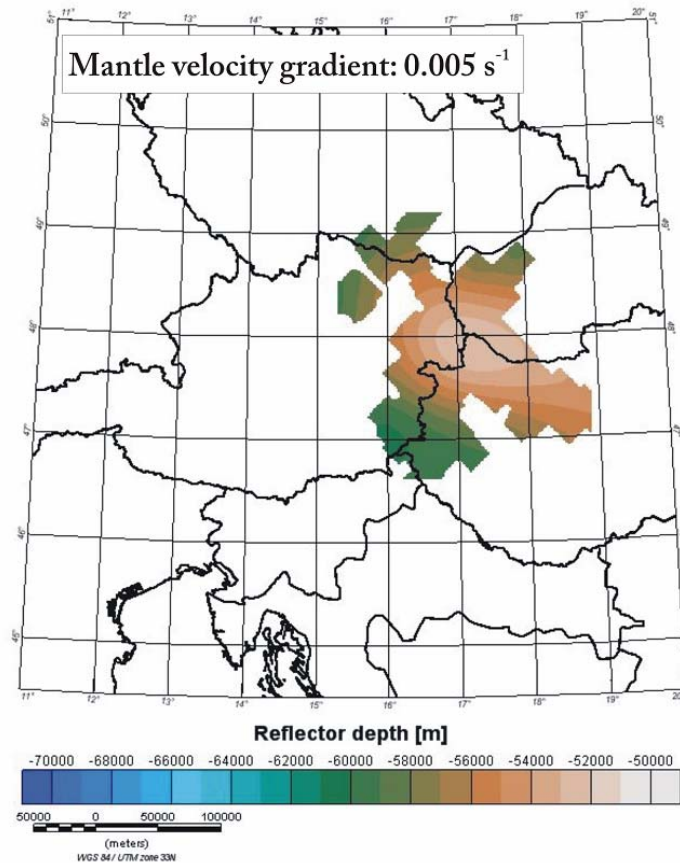


Figure 5.26.

Taking the difference plots (*Figures 5.27a/b/c*) for the various gradients reveals the influence of velocity gradients on depth. Referring to the top of the structure, the difference is  $\sim 6$  km for the model  $'0.01 \text{ s}^{-1}-0.005 \text{ s}^{-1}'$ ,  $4-5$  km for  $'0.005 \text{ s}^{-1}-0.002 \text{ s}^{-1}'$  and  $11$  km for  $'0.01 \text{ s}^{-1}-0.002 \text{ s}^{-1}'$ . Between the different models, there is no constant  $z$ -shift. Differences in depth are larger in the centre of the structure and smaller towards the edges. The reason for this may be found in the coverage of travel times, which is dense in the middle of the structure and lessens towards the edge.

Under the assumption of linear ray paths, the sensitivity between the change in velocity and resulting change in depth can be estimated by expressing the depth from equation E.50 and calculating  $dz/dv$ . Based on a simplified reflector depth model with an average crust and mantle velocity of  $7.3 \text{ km/s}$  and a reflector depth of  $55 \text{ km}$ , an increase in velocity of  $\sim 2 \%$  results in an increase in depth of  $\sim 17 \%$ . For wide-angle reflections, the relationship between the change in velocity and the resulting change in depth is evidently non-linear. For near vertical incidences, on the other hand, this relationship is almost linear. That means, an increase in velocity of  $\sim 2 \%$  leads to an increase in depth of only  $\sim 2 \%$ .

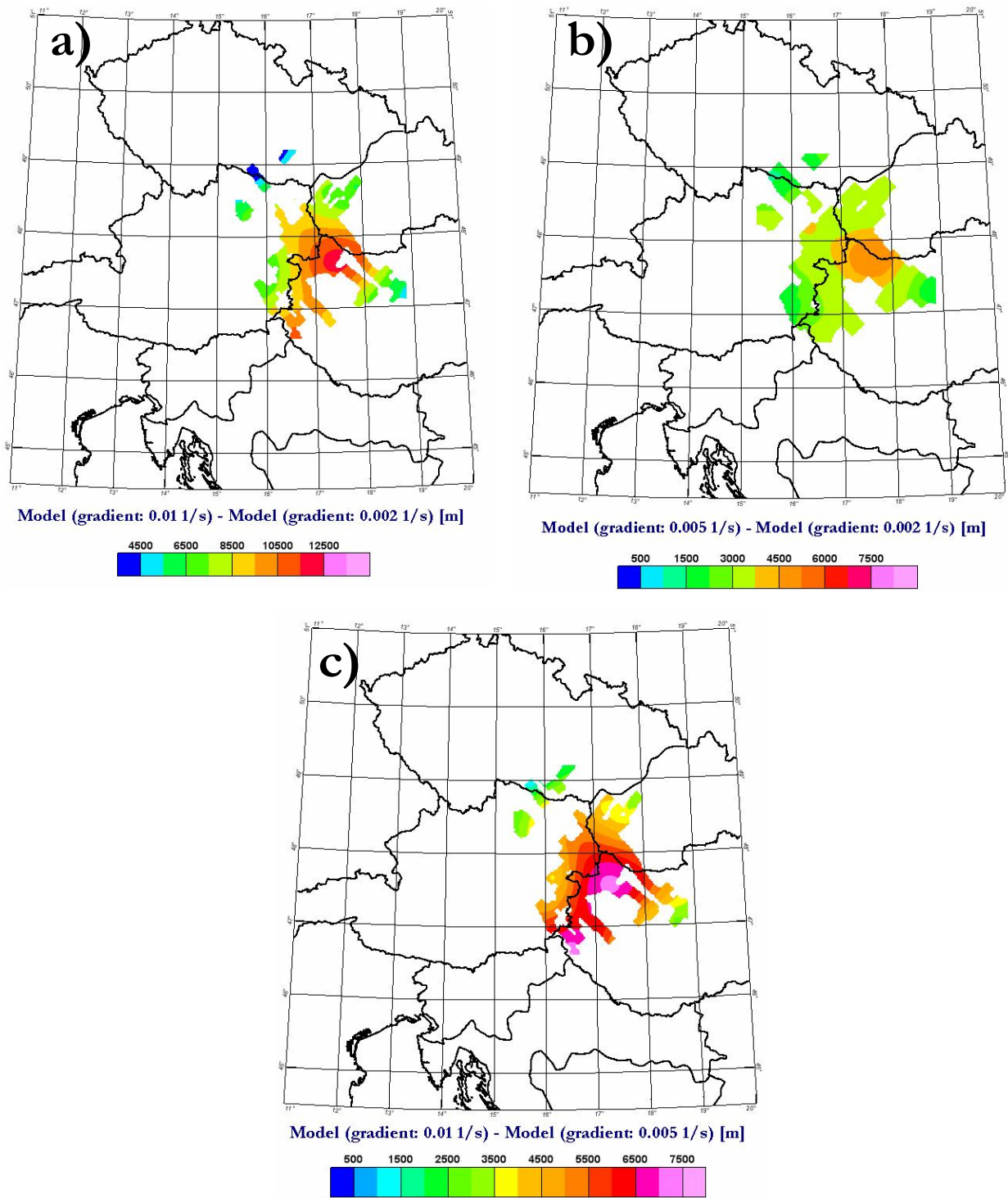


Figure 5.27. Difference plots between the various reflector depth models.

## Best fitting model

Since the model with a **mantle velocity gradient of  $0.005 \text{ s}^{-1}$**  shows the best performance during inversion, with an initial rms-travel time error of 0.32 s and 0.30 s after the third iteration, *Figure 5.28* represents the most likely result.

The reflector structure can be described as slightly up-doming with the top of the structure at an **average depth of 54 km**. The slopes dip to depths of  $\sim 60$  km. The reflector extends  $\sim 150$  km to the east and  $\sim 150$  km to the north and is situated at the boundary of Austria, Hungary and Slovakia.

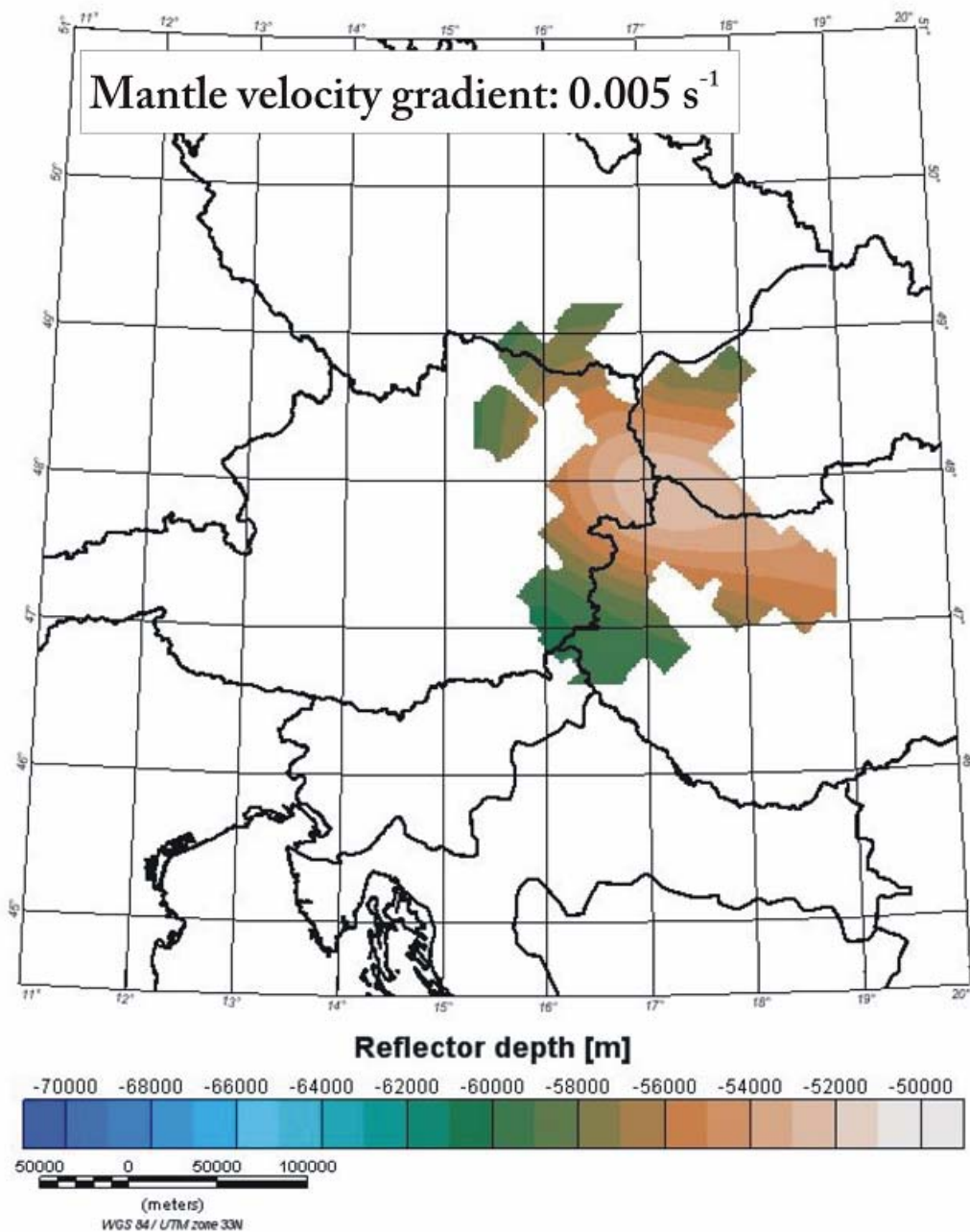


Figure 5.28.



## 6 Interpretation of 'R2'- travel times

Second reflective events ('R2') (Figure 6.1) are obtained in a couple of seismic sections and appear at offsets >350 km. Their occurrence is characterized by a delay in travel time of up to 1000 ms and by a gap in reflectivity between the first ('R1') and the second event ('R2').

These latter events allow for the following interpretations

- a second distinct reflector at a different depth (special case: lithosphere-asthenosphere boundary)
- the second event results from multiple reflections between the Moho and 'R1'

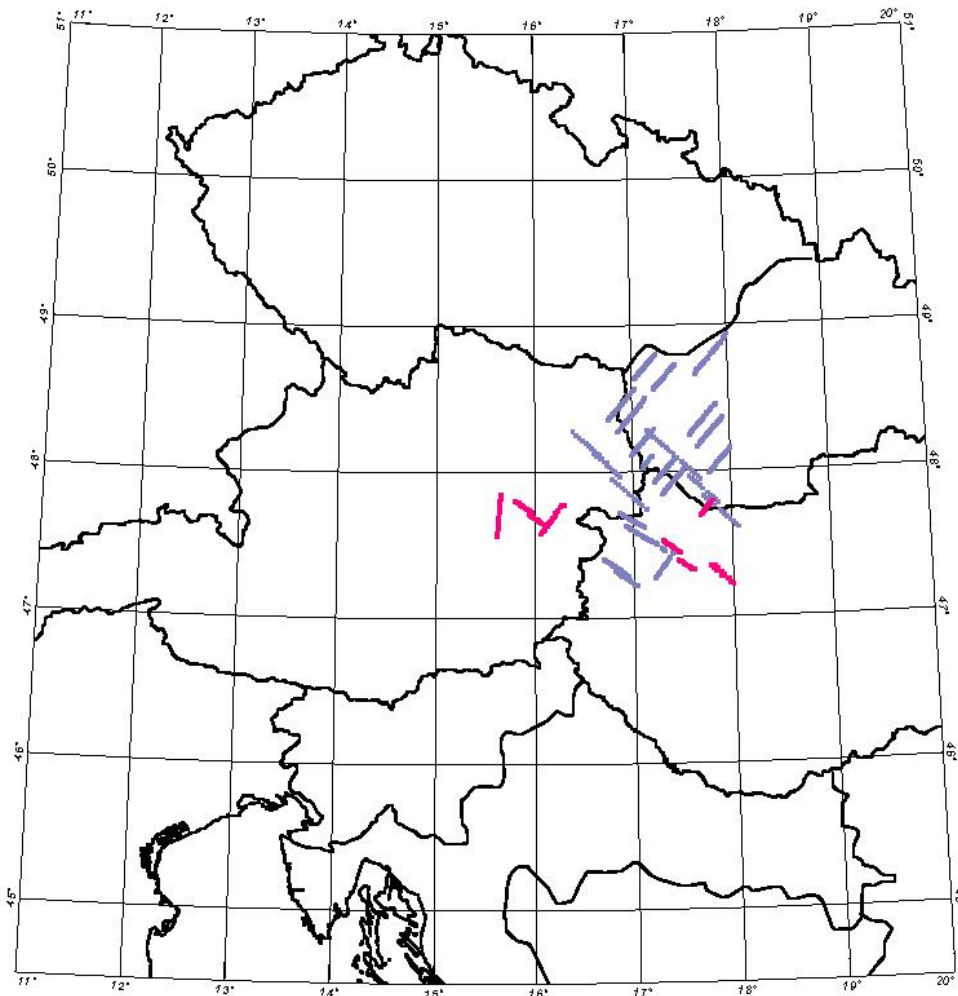


**Figure 6.1.** Travel time coverage after application of the CMP-method. Travel times dotted in blue refer to the reflective event 'R1', those dotted in pink to 'R2'.

## Interpretation as a second distinct reflector

The occurrence of two reflective events may simply be interpreted as two distinct reflectors at different depths. Modelling of travel times with 'ANRAY' based on a mantle velocity gradient of  $0.01 \text{ s}^{-1}$  for two different depths reveals a good match between the first reflective event and a reflector depth of **55 km**, while the second event could be associated with a reflector depth of **80 km** (Figure 6.2). These depth values, however, apply for the seismic section of Figure 6.2 only; for other sections, different depths may apply.

Using the difference plots of Figure 5.27 the depth of the second reflective event can be estimated for the more likely velocity gradient of  $0.005 \text{ s}^{-1}$ . The reflector is then situated at a depth of approximately 70 km.

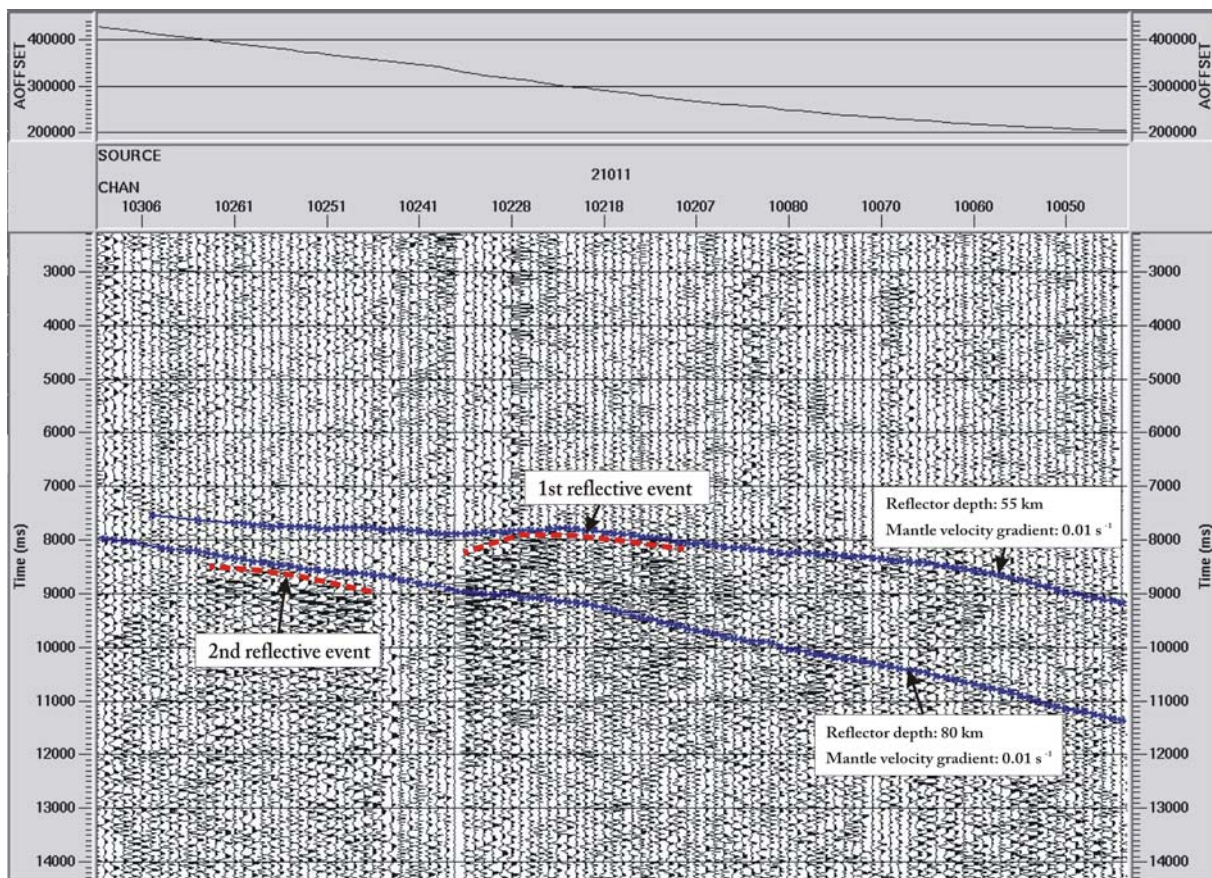


**Figure 6.2.** A reflector situated at a depth of 55 km could cause the first reflective event, a second reflector at a depth of 80 km may result in the second reflective event. Computation of travel times is based on a mantle velocity gradient of  $0.01 \text{ s}^{-1}$ .

## Special case of a second reflector: lithosphere-asthenosphere boundary

A special case of a second reflector is the lithosphere-asthenosphere boundary. Referring to the model by *Lenkey (1999)*, the lithosphere-asthenosphere boundary is situated at depths between  $\sim 70 \text{ km}$  in the Panonnian Basin and  $\sim 200 \text{ km}$  in the Eastern Alps. This boundary (Figure 6.3), however, is not well constrained and may be inaccurate in some places. Since velocities for such great depths are poorly known as well, reflection travel times may be modelled inaccurately and therefore need to be regarded cautiously. A rather good match with a travel time difference of  $\sim 1 \text{ s}$  between the picked second reflective event and the calculated travel times (based on the

finite difference method, mantle velocity gradient of  $0.005 \text{ s}^{-1}$ ) is obtained in *Figure 6.4*. For most other seismic sections, however, travel times differ hugely and thus make the assumption of the lithosphere-asthenosphere boundary rather implausible. Moreover, since exact velocities for such great depths are unknown, the assumption of a constant velocity gradient may pose another significant source of error.

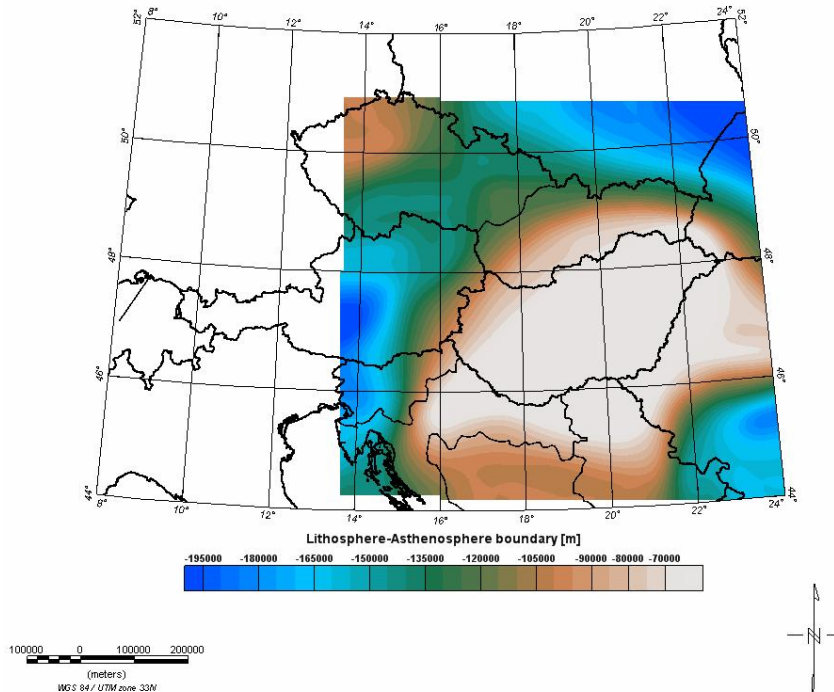


**Figure 6.3.** Depth values of the lithosphere-asthenosphere boundary.

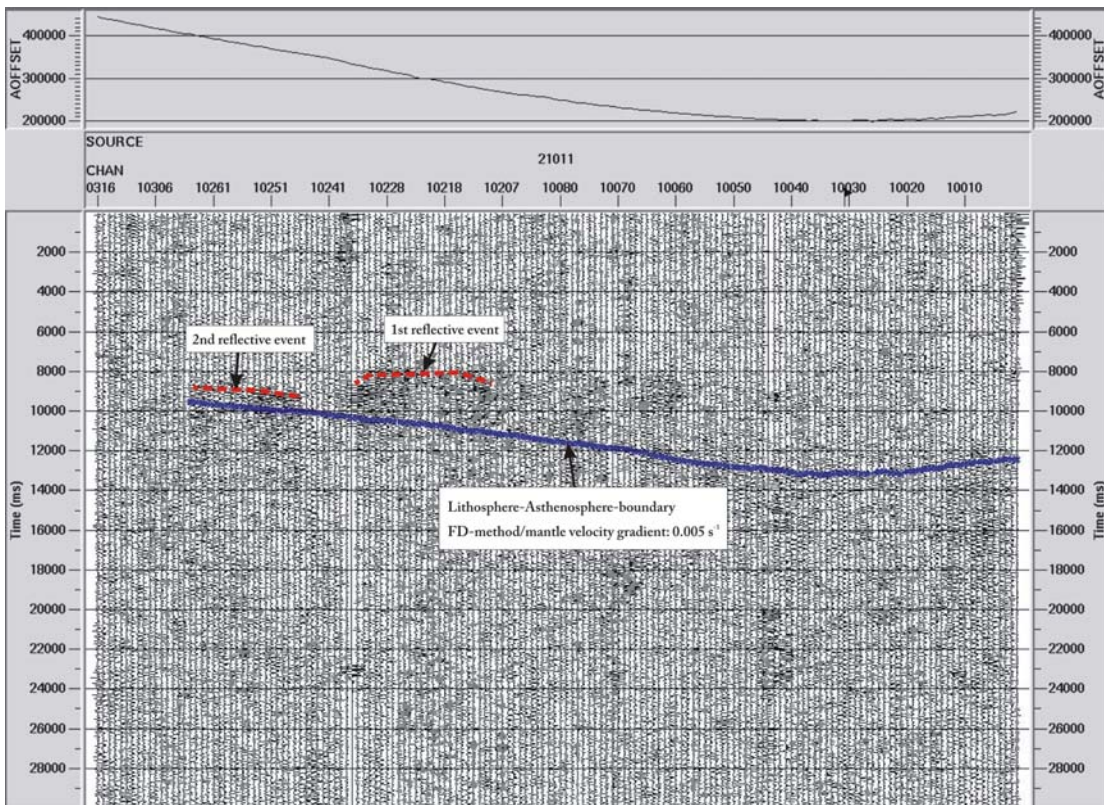


**Figure 6.4.** Travel times based on the lithosphere-asthenosphere model of *Figure 6.3* are approximately 1 s longer compared to the second reflective event.

## Interpretation as a multiple reflection

The gap in reflectivity and the time shift between the two reflective events may be caused by a multiple reflection between the Moho and 'R1'. Comparisons of computed multiple reflection travel times (based on a reflector depth of 55 km and a mantle velocity gradient of  $0.005 \text{ s}^{-1}$ ), however, refute this assumption, as the computed times are over 1 s longer than the second reflective event (*Figure 6.5* displays one example).

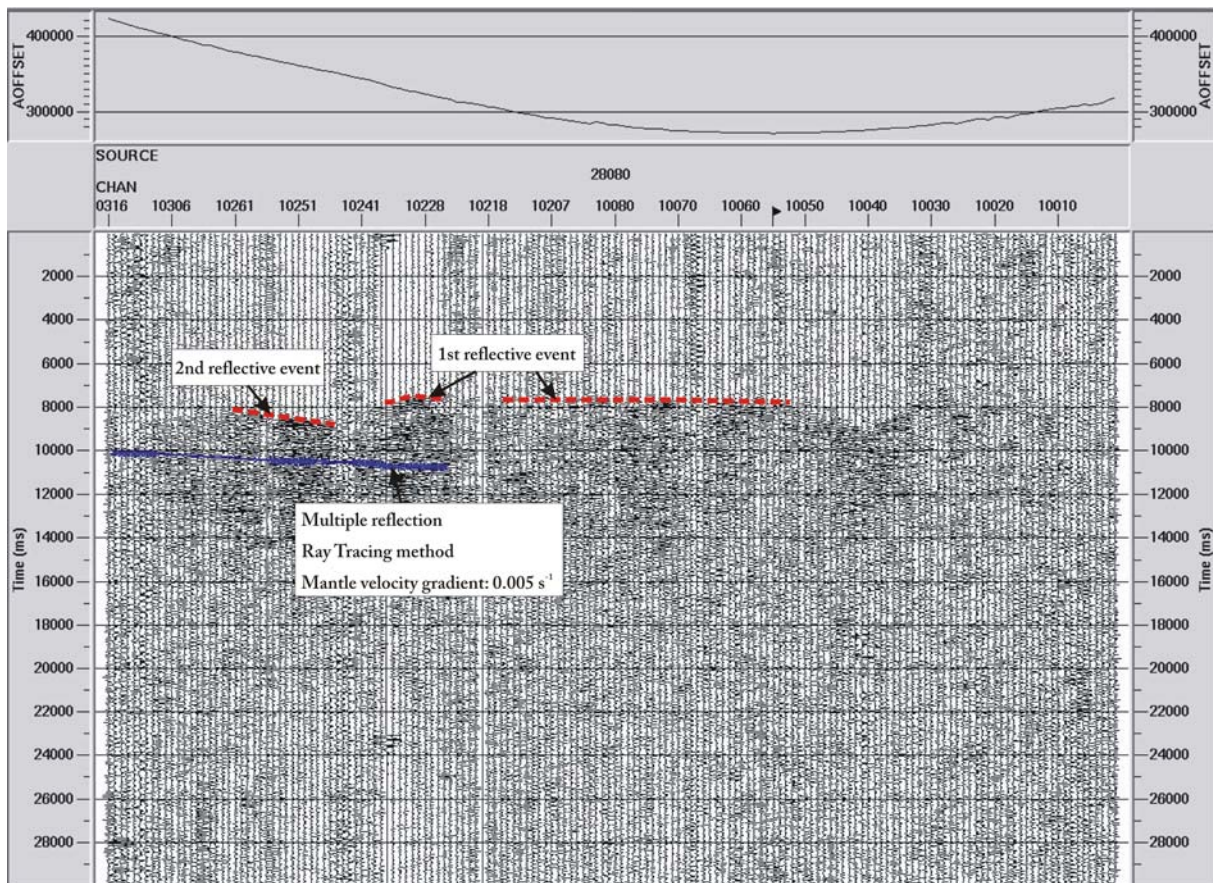


**Figure 6.5.** Travel times from multiple reflection do not coincide with the first arrivals of the second reflective event, with over 1 s difference. Thus, a multiple reflection does not explain the occurrence of the second reflective event.

Summing up, multiple reflections do definitely not explain the occurrence of the second reflective event with travel time differences of over 1 s. The lithosphere-asthenosphere boundary, as a special case of a second reflector, is too vaguely determined to be explicitly assigned to the second reflective event. Additional uncertainty arises due to unknown velocities at these great depths.

The most likely explanation for the occurrence of the second reflective event is a distinct **second reflector** at a depth of  $\sim 80 \text{ km}$  (based on a mantle velocity gradient of  $0.01 \text{ s}^{-1}$ ). For the more plausible velocity gradient of  $0.005 \text{ s}^{-1}$ , the **reflector depth** can be estimated at  $\sim 70 \text{ km}$ .

## 7 Comparison with related studies and tectonic interpretation

Upper mantle reflection travel times obtained from wide-angle seismic reflection experiments originate from a slightly up-doming, sub-horizontal mantle reflector situated at a depth of approximately 55 km in the geological transition zone of Eastern Alps/Carpathians and Pannonian Basin. Travel time inversion was based on a mantle velocity gradient of  $0.005 \text{ s}^{-1}$ .

Seismic studies in adjacent areas show mantle reflectors in similar depths and thus confirm that mantle reflectors are more widespread than originally thought in the transition zone of the Eastern Alps and the Carpathians.

Investigation of the lithospheric structure of the Bohemian Massif and the Variscan belt during the SUDETES 2003 experiment revealed a sub-horizontal upper mantle reflector at a depth of 55 – 60 km [Hrubcova *et al.* 2005] (Figure 7.1). Since only one seismic section has been modelled, little information is given about the lateral reflector extent. However, due to geographic proximity and good coincidence with our model, this reflector is very likely to represent the same feature as the reflector from this thesis.

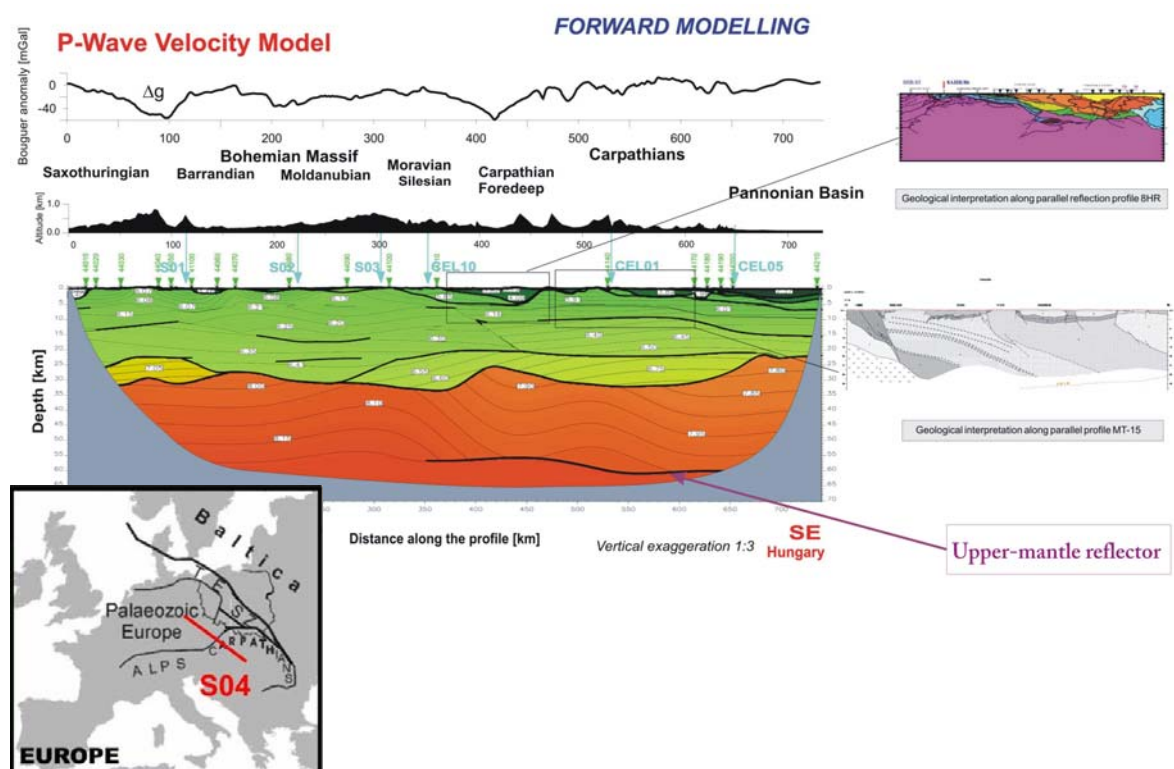


**Figure 7.1.** Geological and velocity model along the seismic section S04 from the SUDETES 2003 data set. The profile, which runs across the Carpathians, shows a distinct reflector at depths of 55-60 km [Hrubcova *et al.* 2006].

Based on the CELEBRATION 2000 seismic experiments, *Sroda (2008)* investigated reflections from the Carpathian upper mantle. Tomographic modelling of travel times revealed a mantle reflector of ca. 200 x 200 km size beneath the Carpathians. This reflector, as illustrated in *Figure 7.2*, dips in north-south direction, from 45-50 km in the south to 65-70 km in the north. The discontinuity was interpreted as a shear zone which originated in a compressional stress regime during collision of the continental lithospheric plates. In terms of depth and shape, the reflector derived by *Sroda (2008)* differs significantly from our model and may therefore be regarded as a separate reflector unit.

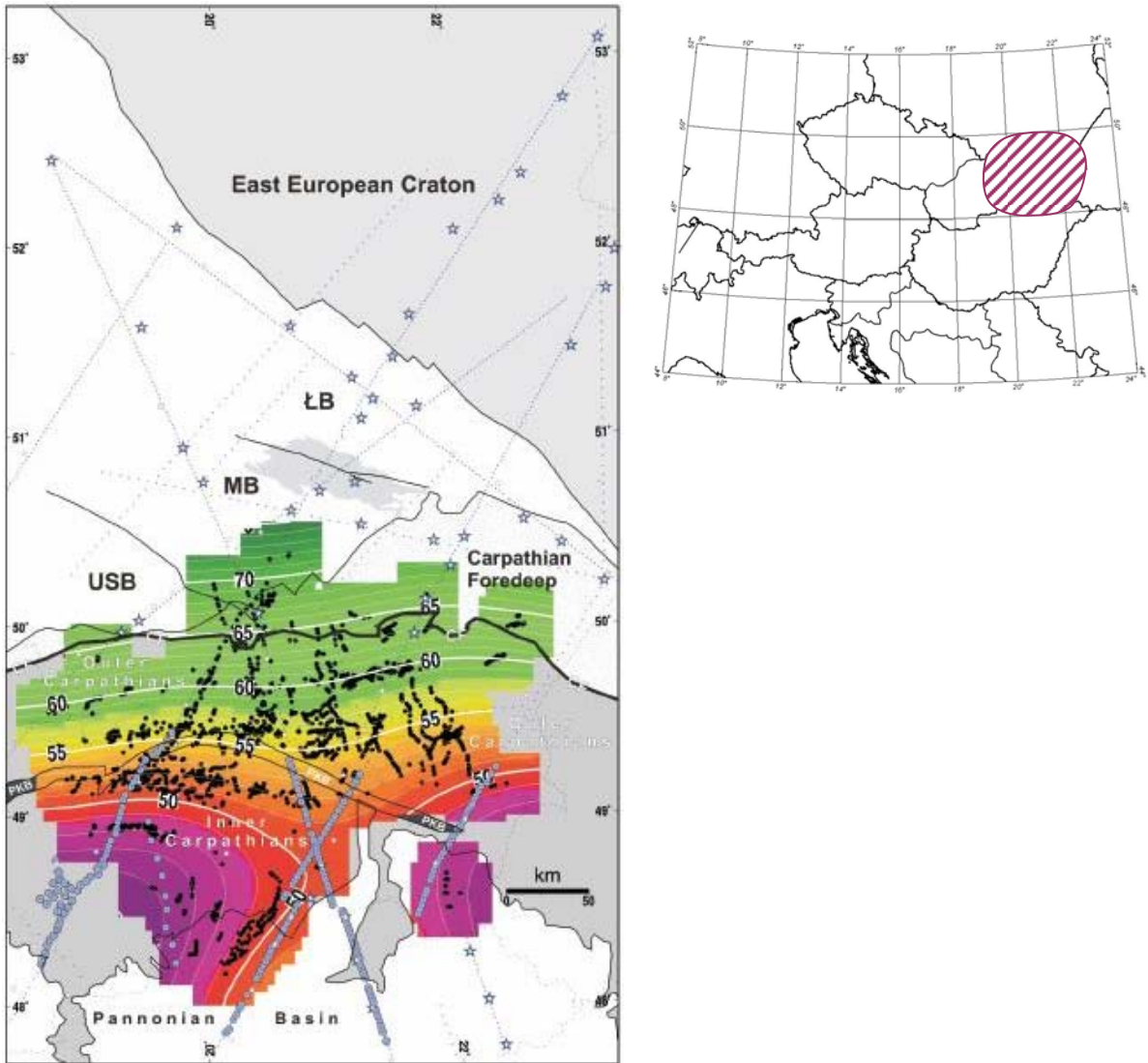


**Figure 7.2.** Map of the Carpathian mantle reflector derived by *Sroda (2008)*. Blue stars represent shot points; blue circles represent receivers.

Interpretation in terms of the origin of upper mantle reflectivity in our area of investigation is a difficult task, but its occurrence is likely to be related to tectonic processes in that region. The approach of interpreting the mantle reflector as part of the subduction slab of the European plate underthrusting the Pannonian Fragment is not suitable since our reflector model is not significantly dipping.

Shear zones which are characterized by a decrease in both velocity and density can be excluded as an explanation too since our studies indicate a velocity increase.

Our mantle reflector, which best represents the category ‘**Sub-horizontal mantle reflectors**’ (section 2.3), is most likely to be caused by intrusion of mafic material into the upper mantle (Figure 7.3). The original cause may be found in the collision of the European Plate with the Adriatic Microplate which is accompanied by an escape process of the Pannonian Fragment. Extensional processes of the Pannonian Fragment lead to a decrease in crustal thickness. Tectonic weak zones related to crustal thinning may facilitate the intrusion of mafic material from the asthenosphere into the upper mantle and lower crust and may result in the observed reflectivity. This explanation is further supported by gravity measurements in the region. Figure 7.4a shows the residual Bouguer gravity after subtraction of the gravity effect of the upper 10 km of the crust and the Moho topography [Brückel et al. 2006] It reveals a strong positive anomaly [60-80 mgal] which coincides well with our reflector model region. This anomaly could be explained through higher-density mafic material which intruded into the upper mantle and lower crust. This concept of intrusion would also explain the occurrence of high lower crustal velocities ( $> 7$  km/s) in the region (Figure 7.4b).

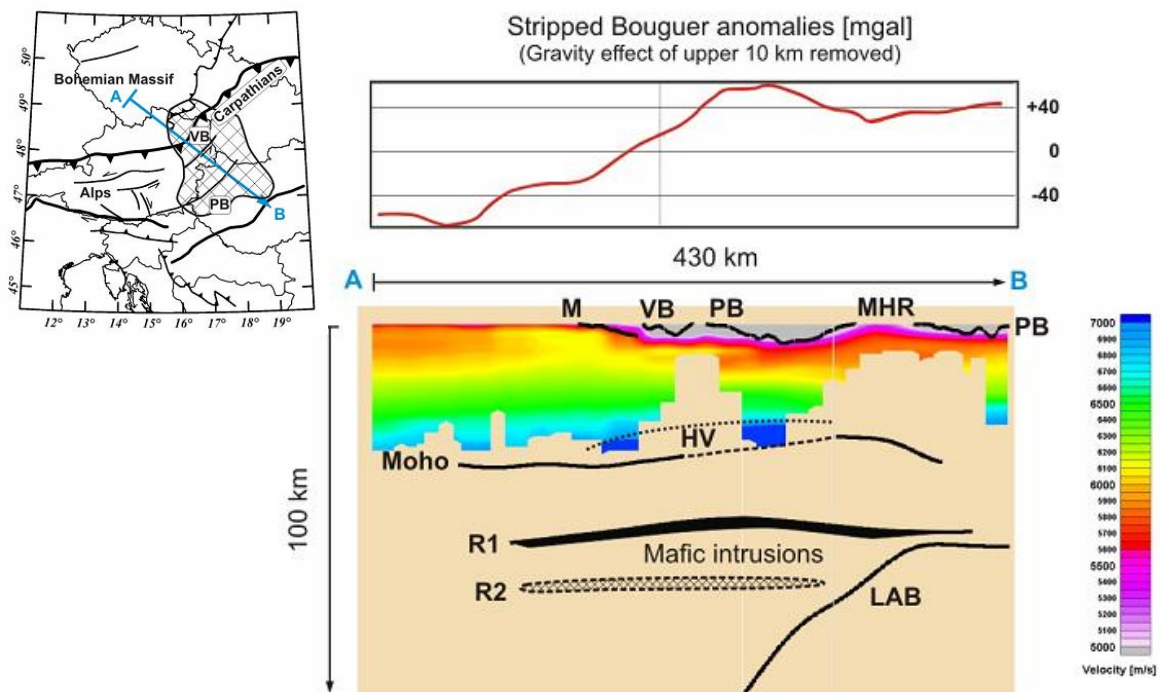


**Figure 7.3.** A vertical cross-section through our reflector model. (M: Molasse; VB: Vienna Basin; PB: Pannonian Basin; MHR: Mid-Hungarian mountain range). The colour-coded velocity field of the crust is shown together with the Moho (broken line: zone where no clear PmP-phases are obtained). R1 is the reflector modelled with a mantle velocity gradient of  $0.005 \text{ s}^{-1}$ . R2 is the assumed second mantle reflector approximately 25 km below R1. LAB: Lithosphere-asthenosphere boundary. The stripped Bouguer anomaly, shown on top, coincides well with the imagination of mafic intrusions into the upper mantle.

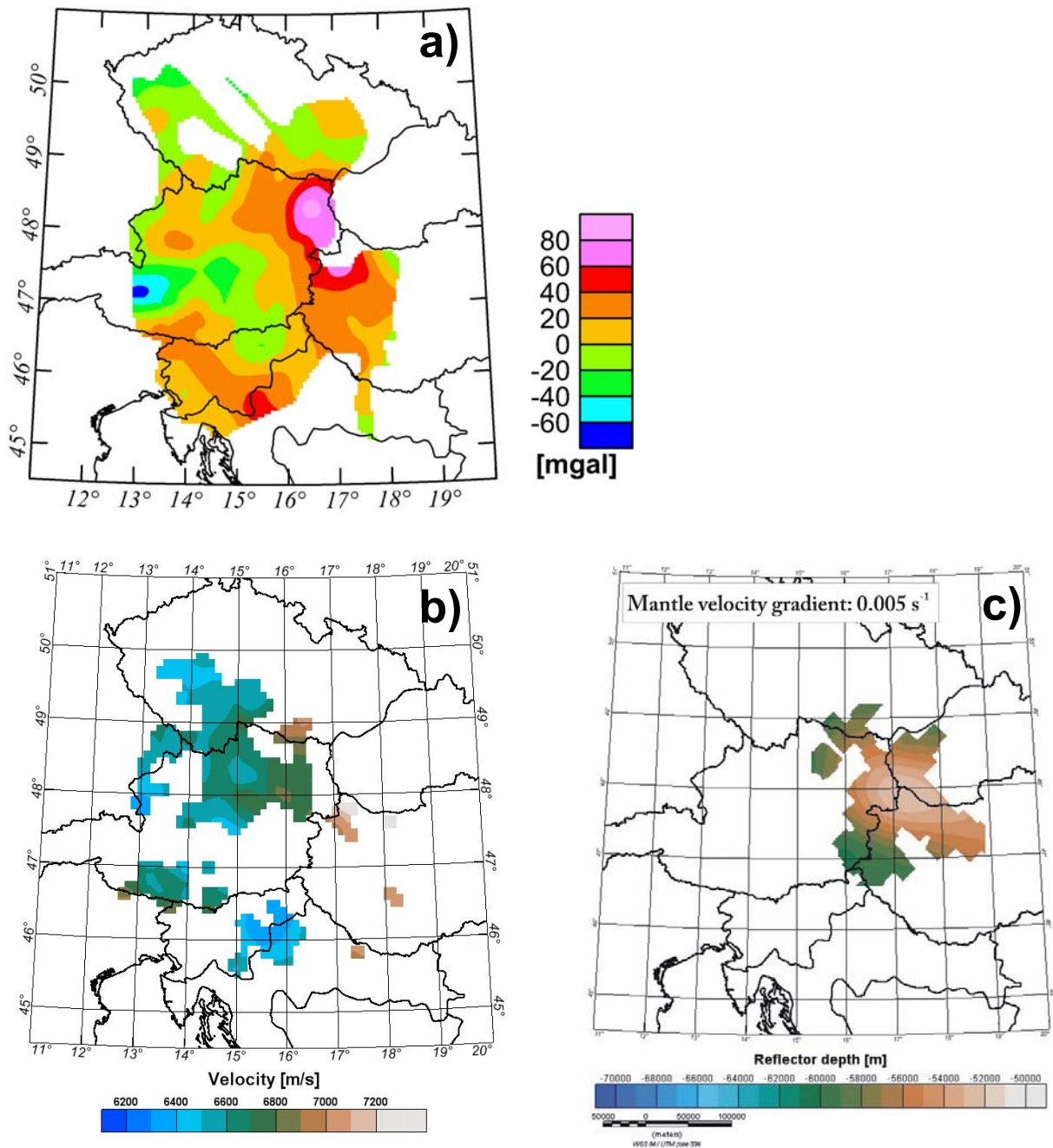


**Figure 7.4.** (a) The residual Bouguer anomaly after subtraction of crustal corrections should show density anomalies in the lower crust and uppermost mantle only. The approach of mantle intrusions as the origin of mantle reflections is further supported by high lower crustal velocities. (b) Depth slice through Pg velocities at a depth of 26 km [Brückl et al. 2006]. (c) Reflector depth model.



## 8 Conclusion and outlook

---

Wide-angle refraction and reflection data sets of ‘CELEBRATION 2000’ and ‘ALP 2002’ experiments reveal upper mantle reflectivity in the transition zone from the Eastern Alps to the Carpathians. Based on the finite difference method, reflection travel times were inverted for depth and shape. The underlying crustal velocity model and Pn- velocities are very well determined through analysis of the above mentioned data sets. Upper mantle velocities, in contrary, are poorly constrained, thus inversion was applied for several velocity gradients –  $0.01 \text{ s}^{-1}$ ,  $0.005 \text{ s}^{-1}$  and  $0.002 \text{ s}^{-1}$ . Comparing the appropriate travel time residuals yields **two realistic reflector models**: a reflector based on the **gradient of  $0.005 \text{ s}^{-1}$**  at a depth of  **$\sim 55 \text{ km}$**  and another one based on the **gradient of  $0.002 \text{ s}^{-1}$**  at a depth of  **$\sim 52 \text{ km}$** . However, when taking the starting travel times residuals into account, the model with the gradient  $0.005 \text{ s}^{-1}$  is to be favoured (travel time residuals of 32 ms [ $0.005 \text{ s}^{-1}$ ] and 37 ms [ $0.002 \text{ s}^{-1}$ ]). The reflector shape can be described as sub-horizontal and slightly up-doming.

The origin of the mantle reflector is most likely to be associated with mafic intrusions into the upper mantle due to tectonic extension in that region. This approach is supported by further geophysical investigations (positive Bouguer gravity and high lower crustal velocities).

Second reflective events observed in some seismic sections most likely originate from a distinct second reflector at a greater depth of approximately 70 km.

The first estimation of the reflector depth (see section 5.1) of 70 km, based on a mantle velocity gradient of  $0.01 \text{ s}^{-1}$ , is actually not very accurate in hindsight and demonstrates that a layered 1D-model with constant velocities is not suitable for depth estimations.

In general, upper mantle reflectivity seems to be more widely spread than thought in the region of the Eastern Alps and the Carpathians. Lithospheric investigations in adjacent areas (*Figure 8.1*), reveal mantle reflectors in similar depths as our model. Research done by *Hrubcova (2005)* north of our reflector area also shows a sub-horizontal mantle reflector at a depth of  $\sim 55 \text{ km}$ . The mantle reflector model by *Sroda (2008)* is situated in a different geological zone and does not really correspond in terms of depth and shape, but due the proximity of both reflectors, it may be interesting to verify if there is a link between both models. This should be examined in future seismic experiments.

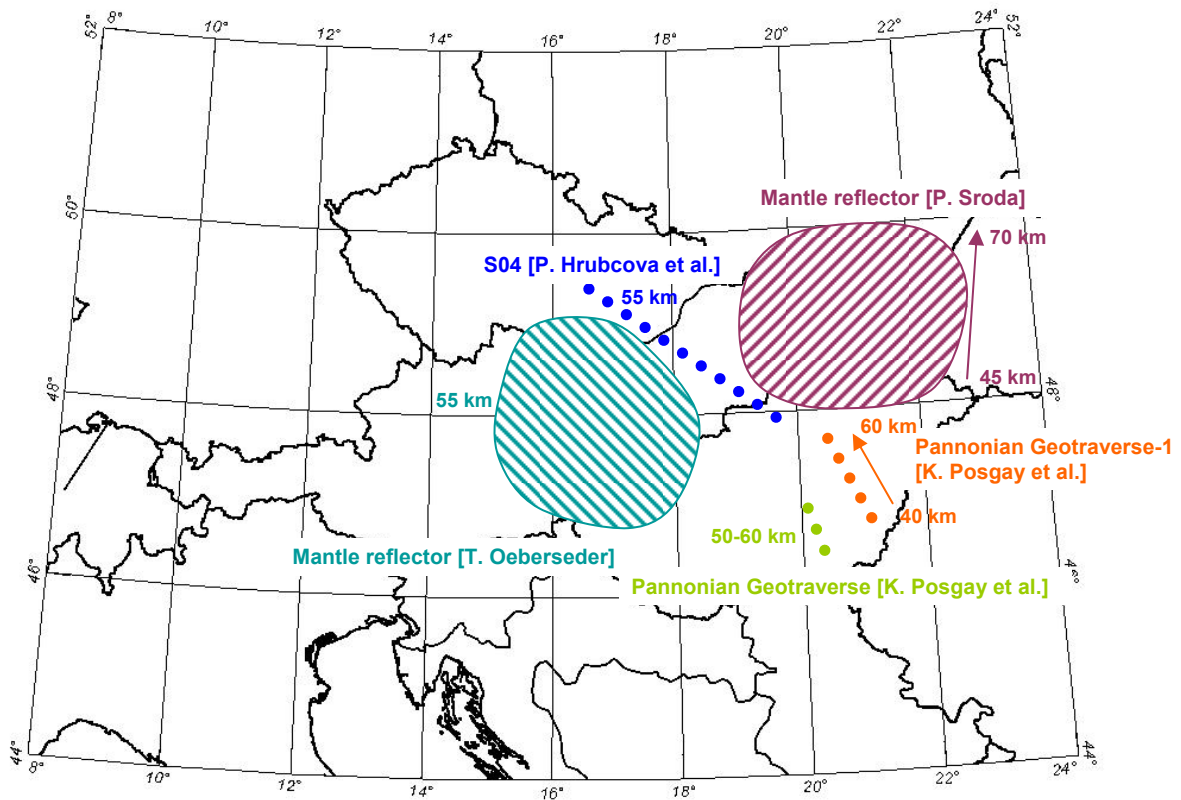


**Figure 8.1.** Overall view of observed mantle reflectors in the Eastern Alps/Carpathians with assigned depth values. Arrows indicate the direction of the reflector dip.

# A Appendix

## A.1 Inversion program by Hole (1996)

Before the data structure and the parameters of the inversion program by *Hole (1996)* shall be explained, adjustments to the data set need to be made. The coordinate system needs to be changed in a way, so that its origin coincides with the model boundaries (see *Figure A1a*). The  $z$ -coordinate has to be positive in the downward direction. The top interface, e.g. topography (*Figure A1b*), has to be shifted in a way so that it lies entirely beneath the plane  $z=0$ . Consequently, to maintain the original model, all its interfaces (e.g. Moho-discontinuity, reflectors...) and velocities needs to be shifted by the same amount.

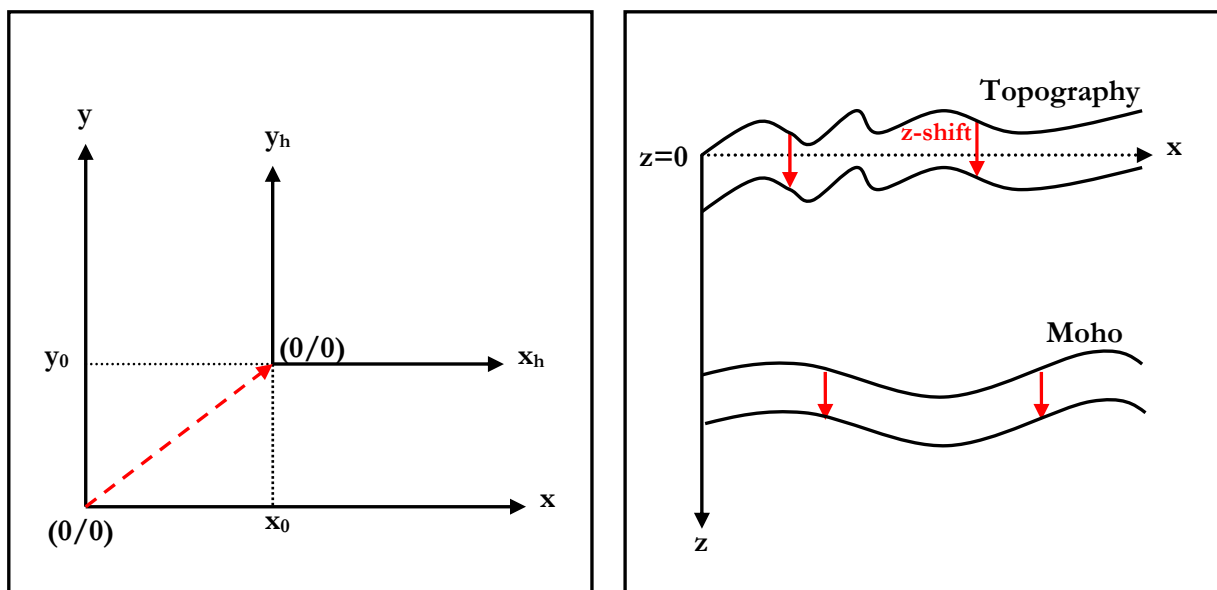


**Figure A1.** (a) Cartesian coordinate transformation necessary for the inversion application; (b) inversion procedure by Hole requires a model-shift in  $z$ -direction so that the whole structure is beneath the  $z=0$ -plane.

Hole's inversion program has primarily been designed for UNIX-based systems and requires the compilation of two directories – one that is used for inversion execution, and another containing all the files associated with shot and receiver geometries and travel time data. The initial data set containing shot/receiver geometries and travel times needs to be split up into four different files,

```
<prefix>.his  
<prefix><shot-ID>.hir  
<prefix><shot-ID>.hip  
<prefix><shot-ID>.rir
```

with the  $\langle \text{prefix} \rangle$ .his-file containing a list of all shots (specified by shot-IDs) with their order determining the course of computation.

Its prefix can be chosen arbitrarily, but needs to be transferred to the other three file types too (.hir/.hip/.rir). For each shot defined in the file '<prefix>.his' we need a complete set of files: '<prefix><shot-ID>.hir', '<prefix><shot-ID>.hip' and '<prefix><shot-ID>.rir'. *Figure A2* illustrates the splitting of the original data set into four different files with geometry, travel time and receiver specifications.

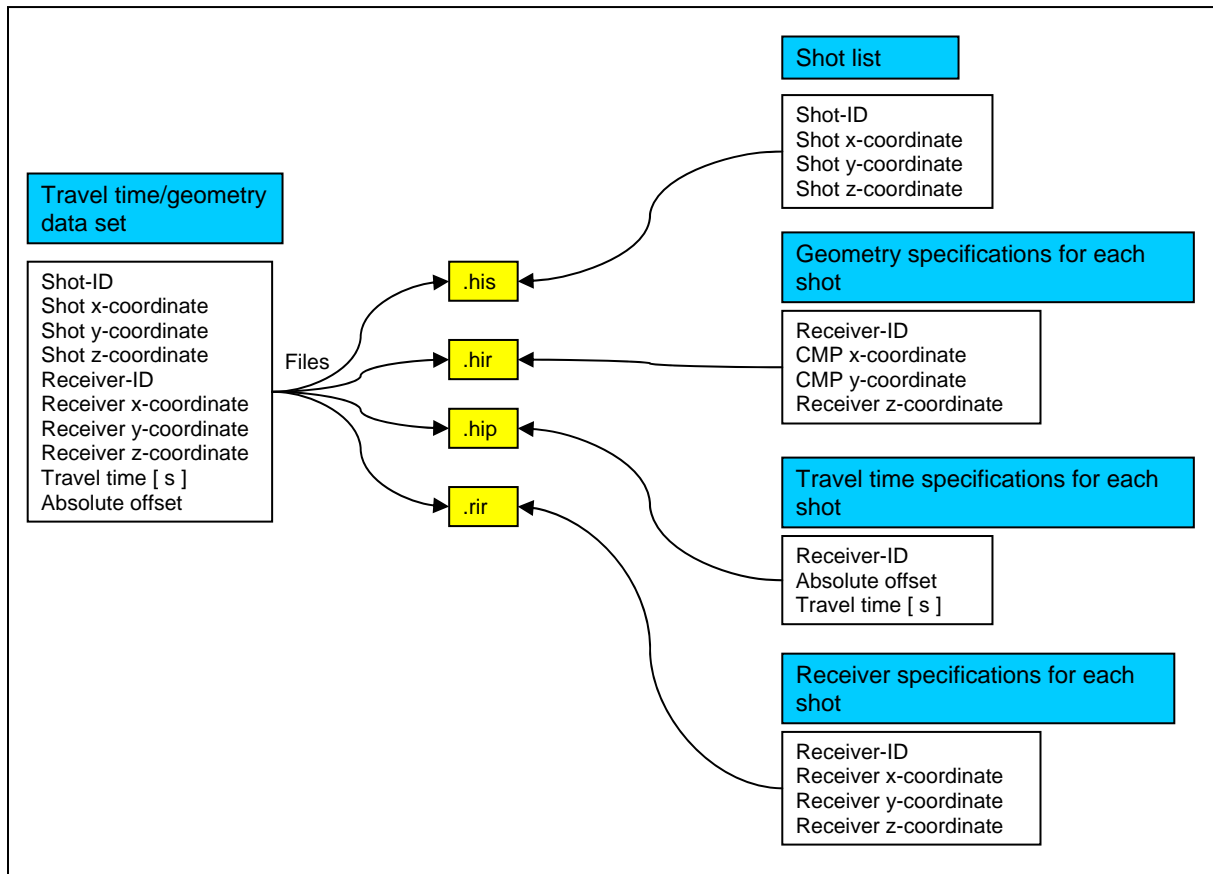


**Figure A2.** The data set including travel time and geometry specifications needs to be split into four files, each containing specific data. The file '.his' contains a list of all shots, the file '.hir' cmp locations, the file '.hip' travel time specifications and the file '.rir' the receiver geometry.

In addition to the above mentioned file types, files relating to velocities and reflector specifications are needed. All those files (including files '.his', '.hip', '.hir', '.rir') need to be linked to a script file that is retrieved when the inversion program is to be executed. The files are to be named as follows

```

<prefix>.ri          (script file)
<prefix>.v1d
<prefix>.r1d
vel.mod
vreset.mod

```

vel.mod and vreset.mod are two identical velocity files that have to be named in that very way, otherwise the system will not work properly.

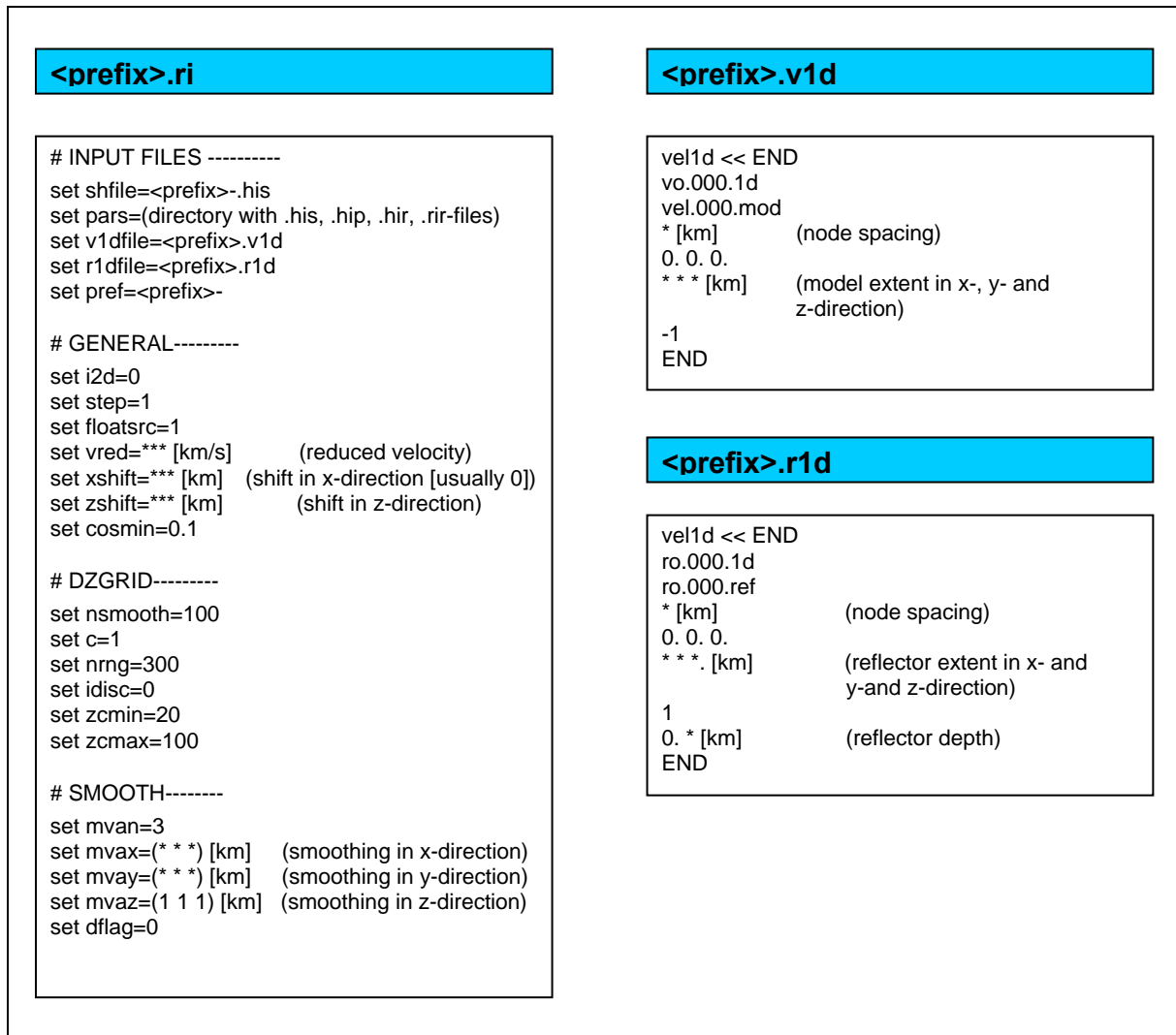


**Figure A3.** Files ‘<prefix>.ri’, ‘<prefix>.v1d’, ‘<prefix>.r1d’, needed for the inversion. The asterisk represents a number to be filled in (its meaning is explained in brackets).

The file ‘<prefix>.ri’ (*Figure A3*) acts as the executing file, therefore, input files have to be linked to this file. Additionally, a number of parameters can be changed and adjusted in this file. Amongst them are shifts in x- and z- direction (the amount by which the model is moved downwards) and the parameter that controls the reduction of travel times. Taking high values for this parameter yields unreduced travel times.

The relationship between reduced travel times and unreduced travel times is given by

$$t_{\text{reduced}} = t_{\text{unreduced}} - (\text{absolute offset}/v_{\text{reduced}}) \quad (\text{A.1})$$

The number of iterations used for inversion can be adjusted when using ‘mvax’, ‘mvay’ and ‘mvaz’ under ‘#SMOOTH’ in *Figure A3*. These parameters define the extent of smoothing in x-, y- and z-direction after each iteration. The number of iterations is defined by the numbers allocated to ‘mvax’, ‘mvay’ and ‘mvaz’. Two arbitrary values, e.g. 11 and 9 for both - ‘mvax’ and ‘mvay’ (‘mvaz’ can be neglected since smoothing in z-direction is not needed), means two iterations to be carried out with smoothing over a distance of 11 grid nodes in both x- and y-

directions during the first iteration, and over a distance of 9 grid nodes during the second iteration.

As shown in *Figure A3*, more parameters can be adjusted, but they do not influence the output significantly and may remain unchanged. Parameters to be adjusted for the file ‘<prefix>.v1d’ are the extent of the velocity model in x-, y- and z-direction and its node spacing (all in km). The velocity model itself is specified by ‘vel.000.mod’.

Reflector characteristics, such as lateral and vertical extent and the reflector depth (all in km), can be adjusted in the file ‘<prefix>.r1d’. This file allows to define the reflector as a plane horizontal interface at a certain depth. At the beginning of computation, the program creates the file ‘ro.000.ref’ referring to the depth and extent of the reflector of file ‘<prefix>.r1d’. The file ‘ro.000.ref’ acts as the initial reflector depth model; after each iteration this file will be updated (‘ro.001.ref’, ‘ro.002.ref’, ‘ro.003.ref’...).

In cases where an initial reflector model is needed that contains some kind of structure and differs from a horizontal plane, the file ‘ro.000.ref’ containing the wanted reflector structure needs to be introduced into the system before the computation starts. Additionally, the number ‘1’ in the r1d-file needs to be amended to ‘-1’ (*Figure A4*). Thus, the system refers directly to the altered file ‘ro.000.ref’ and ignores the reflector depth value below ‘-1’.

```

vel1d << END
ro.000.1d
ro.000.ref
* [km]          (node spacing)
0. 0. 0.
***. [km]      (reflector extent in x- and
                y-and z-direction)
-1
0. * [km]      (reflector depth)
END

```

**Figure A4.** Modified file ‘<prefix>.r1d’ (compare with *Figure A3*) for reflector structures that differ from a plane horizontal interface.

After having defined the data structure of the inversion program, it can be started in the UNIX-based system using the following command

```
ri++ <prefix>.ri model=vel.mod> <prefix>.log
```

with ‘<prefix>.log’ being the output file.

Computation is carried out for each shot in the file ‘<prefix>.his’ and is recorded in the file ‘<prefix>.log’. The principle of computation involves the inversion of all shots during the first iteration, then during the next iteration and so on. As a result, the rms-travel time residual and the change in depth  $\Delta z$  will be displayed for each shot. Computation has finished (without errors) when ‘Summing DZ’ is displayed at the end of the file ‘<prefix>.log’.

Except for the file '<prefix>.log', many more will be created during computation, of which the most important are

**ro.001.dz** → file containing the changes in depth  $\Delta z$  after first iteration  
**ro.002.dz** → file containing the changes in depth  $\Delta z$  after second iteration  
...  
**<prefix>.itr**

The .dz-files can be regarded as an open summary of the <prefix>.log-file for each iteration. Travel time residuals for each shot will be written into these files, whereas travel time residuals of all shots together during one iteration are documented in the file '<prefix>.itr' (*Figure A5*). This is a very useful file, as it illustrates the influence of iterations on rms-travel times.

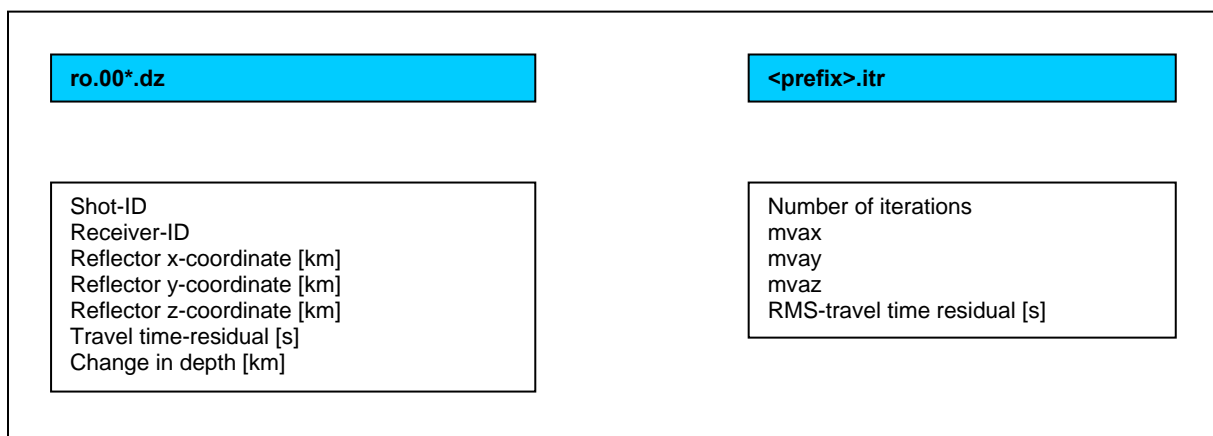


**Figure A5.** Output files 'ro.00\*.dz' and '<prefix>.itr'.

## A.2 Description of the program ‘ANRAY’

---

The program package ‘ANRAY’ has been developed by *Cerveny* and is used for the computation of ray-related properties, such as travel times, ray amplitudes and ray synthetic seismograms. Fundamentally, ‘ANRAY’ is based on the ray tracing equations that have been explained in detail in section 3.2.1.

Important characteristics of the package ‘ANRAY’ include

- the model is 3-D and consists of layers of non-zero thickness
- elastic parameters, such as density and seismic velocities inside the layers are determined either by linear interpolation or by B-spline interpolation
- a point source can be situated anywhere in the model
- the package allows computations in both isotropic and anisotropic layers
- two modes of ray tracing may be carried out: two-point ray tracing and initial-value ray tracing (for explanation, see sections 3.2.2 and 3.2.3)
- receivers can be distributed along the surface, as well as along vertical profiles

### A.2.1 Description of the model

Before the model shall be explained, attention should be drawn to the coordinate system used in the ‘ANRAY’ - package. An altered Cartesian coordinate system is used with the x-axis pointing towards north and the y-axis pointing east. The z-axis is chosen to be positive downwards.

The model resembles a box with plane vertical boundaries bounded at the top and at the bottom by plane/curved interfaces. The space between two interfaces is defined as a layer. Except for the top and bottom boundary, several more interfaces may be introduced into the model. Those interfaces usually separate layers of different elastic parameters. Two interfaces are not allowed to intersect. Interfaces are determined by depth values below or above a 2-D grid, the values in between the grid points are interpolated by bicubic splines resulting in the interface to be smooth.

The elastic parameters, which are also specified at grid points, are interpolated either by linear interpolation or by B-spline interpolation. The units of length and velocity must be used consistently, either in km and km/s, m and m/s or m and m/ms. The density should always be specified in  $\text{g/cm}^3$ .

### A.2.2 Description of input and output files

The data structure of the package ‘ANRAY’ encompasses the input data file ‘LIN’ and the output files ‘LOU’, ‘LU1’, ‘LU2’ and ‘LU3’. Output data describing the computations are stored in the file ‘LOU’. The file ‘LU1’ stores data for plotting ray diagrams, travel time curves and amplitude distance curves. Data that allow the computation of ray synthetic seismograms are stored in the file ‘LU2’. Velocity surfaces can be plotted through the file ‘LU3’.



### A.2.2.1 Input data in the file 'LIN'

The file 'LIN' contains many parameters to be set – the most important ones shall be explained in this section. The neglected ones are documented in the manual on the following website: <http://seis.karlov.mff.cuni.cz>

The input file begins with the specification of interfaces and grids. It contains the following parameters:

- NINT: number of interfaces in the model. The first interface represents the model surface and the last interface represents the model bottom
- MX, MY: number of grid lines  $x=\text{const.}$  and  $y=\text{const.}$
- SX(1),..., SX(MX): x-coordinates of grid lines
- SY(1),..., SY(MY): y-coordinates of grid lines
- Z(1),..., Z(MX\*MY): z-coordinates (depths) of the interface at the grid points beginning at line SX(1) from SY(1) to SY(MY), then followed by line SX(2) and so on

The above parameters need to be specified for each single interface.

The next parameter controls the density distribution in the model (IRHO):

- IRHO=1: density is constant throughout each layer

The following set of parameters specifies the distribution of elastic parameters. Approximation of elastic parameters between the grid points is available in two modes: iso-surface interpolation and B-spline approximation. The latter one has been used throughout this thesis, thus only the parameters required for B-spline interpolation shall be mentioned here.

- IANI: specifies properties of the layer  
IANI=0: layer is isotropic
- NX: number of grid lines in x-direction
- NY: number of grid lines in y-direction
- NZ: number of grid lines in z-direction
- X1(1), X1(2),..., X1(NX): coordinates of the grid lines in x-direction
- Y1(1), Y1(2),..., Y1(NY): coordinates of the grid lines in y-direction
- Z1(1), Z1(2),..., Z1(NZ): coordinates of the grid lines in z-direction

The values of the elastic parameters (P- and S-wave velocities) are assigned in the following way (see also *Figure A7*)

```
X(1), Y(1), Z(1) X(1), Y(1), Z(2) X(1), Y(1), Z(3) ... X(1), Y(2), Z(1) X(1), Y(2), Z(2) X(1), Y(2), Z(3) ...
X(2), Y(1), Z(1) X(2), Y(1), Z(2) X(2), Y(1), Z(3) ... X(2), Y(2), Z(1) X(2), Y(2), Z(2) X(2), Y(2), Z(3) ...
X(3), Y(1), Z(1) X(3), Y(1), Z(2) X(3), Y(1), Z(3) ... X(3), Y(2), Z(1) X(3), Y(2), Z(3) X(3), Y(2), Z(3) ...
...
```

For isotropic layers, the squares of P- and S-wave velocities are to be taken.

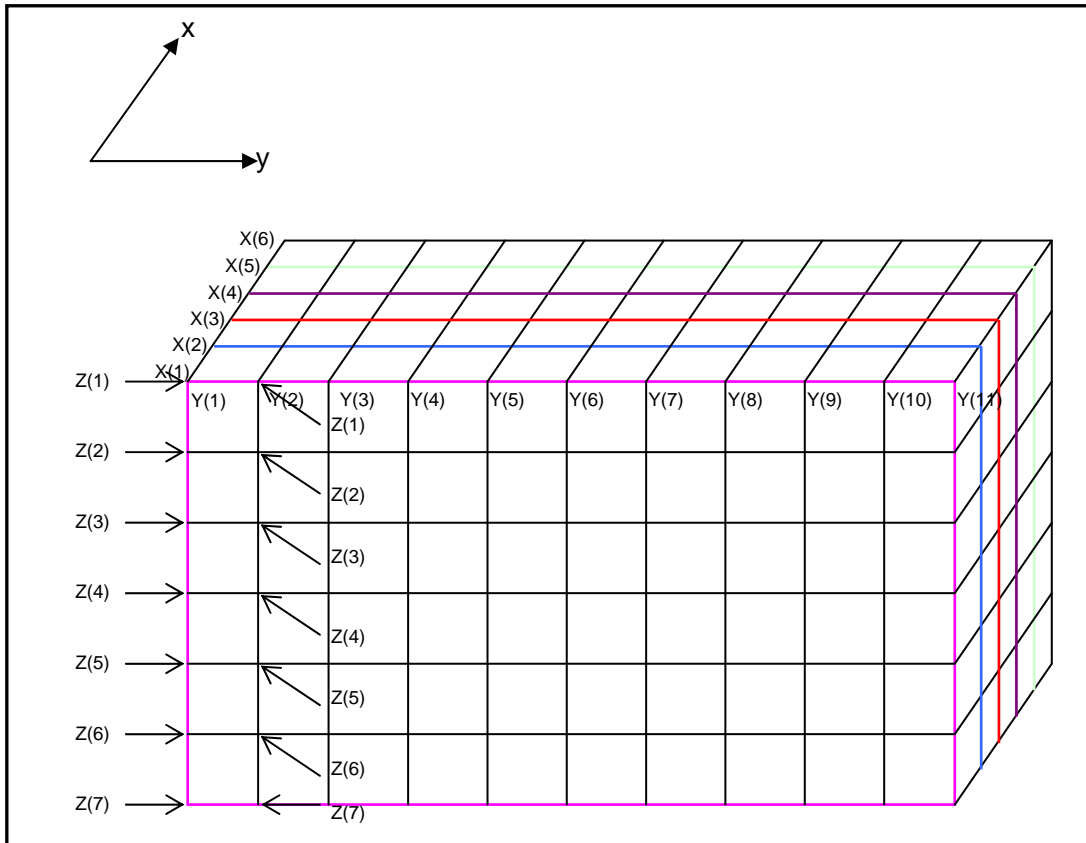


**Figure A6.** Scheme of how elastic parameters are to be assigned to the grid points. At first, values are assigned along the vertical plane X(1) followed by plane X(2), X(3) and so on.

The following parameters deal with ray specific properties:

- MEP: specifies whether initial-value ray tracing or two-point ray tracing is to be performed
  - MEP=0: initial-value ray tracing
  - MEP=1: two-point ray tracing is to be performed with one single receiver; performance with more receivers requires the value 'MEP' to be changed accordingly
- MDIM: controls the level of computations
  - MDIM=0: only rays and travel times are computed
  - MDIM=1: Spreading free amplitudes; reflection/transmission/conversion coefficients are evaluated along the rays
  - MDIM=2: ray amplitudes including geometrical spreading

If two-point ray tracing is to be carried out, parameters include

- PROF: azimuthal angle specifying the angle along which the receivers are situated. The angle is measured in radians from the positive x-axis towards the positive y-axis.
  - PROF=0.0: receivers are situated along the x-axis
  - PROF=1.57: receivers are situated along the y-axis
- DST: distances of receivers from the origin of the profile (XPRF, YPRF)
- XPRF, YPRF: origin regarding the orientation of the receiver profile; usually coincides with the source coordinates

- XREC, YREC: receiver x- and y-coordinates

For regular receiver intervals, PROF and XPRF, YPRF stay the same - the receiver distances, however, do not need to be quoted for each single receiver, but simplify to

- RMIN: distance between the first receiver and the origin (XPRF, YPRF)
- RSTEP: receiver interval

Regarding the source, the following parameters are to be specified

- XSOUR, YSOUR, ZSOUR: (x,y,z)-coordinates of the source
- TSOUR: initial time
- REPS: vicinity to the receiver; the process terminates if a ray is found within this vicinity (only needed for two-point ray tracing)

If initial-value ray tracing is to be carried out, additional parameters need to be set

- AMIN, ASTEP, AMAX: declination angle defined by an initial angle, an angle increment and a maximum angle
- BMIN, BSTEP, BMAX: azimuthal angle specified by an initial angle, an angle increment and a maximum angle

For both modes of ray tracing, the last parameters include the determination of the number of ray segments (see *Figure A7*)

- KREF: number of ray segments
- CODE (I, 1): number of the layer in which the I-th segment of the ray is situated
- CODE (I, 2)=3: compressional wave

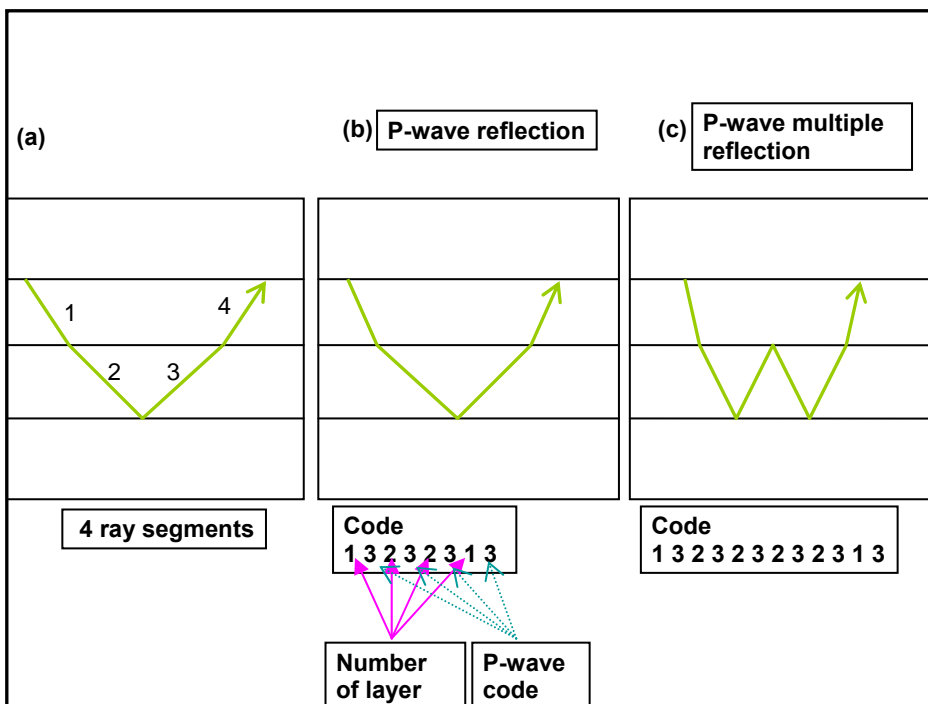


**Figure A7.** Ray code for a simple p-wave reflection (b) and a multiple reflection (c). (a) indicates the number of segments for a simple reflection

### A.2.2.2 Output data to the file 'LOU'

As mentioned above, 'ANRAY' generates several output files with each file containing different ray specific results. Calculated travel times and amplitudes are stored in the file 'LOU'. The other files have not been used, therefore, will not be described here.

The file 'LOU' consists of a repetition of the input parameters followed by the actual ray tracing results. The results are described through the following parameters:

- DD: coordinate of the receiver, at which the ray should arrive (in two-point ray tracing)
- R: radius of the termination point in two-point ray tracing
- XX, YY, ZZ: coordinates of the termination point of the ray
- **T**: **travel time** of the ray
- AZIM, DEC: initial azimuthal and declination angle at the source (in radians)
- IND: Parameter describing the history of the ray  
Important values of IND are:
  - (3) termination of the ray on the model surface
  - (4) termination of the ray on the lower boundary of the model
- IND1: ABS(IND1): number of the interface last hit by the ray
- ITER: number of iterations needed to find the ray within the vicinity of the receiver
- **APX (J, I), APY (J, I), APZ(J, I)**:  
(J, I): complex **amplitudes** of (x,y,z)-components of the polarization vector at the termination point; (J) represents the imaginary part and (I) the real part

## References

---

- Alsdorf, D., Brown, L., Nelson, D.** (1996), Possible upper mantle fabric on seismic profiles from the Tethyan Himalaya and tectonic interpretation, *J. geophys. Res.* 101, 25 305-25 320
- ANCORP Working Group** (1999), Seismic reflection image revealing offset of Andean subduction-zone earthquake locations into oceanic mantle, *Nature* 28, 341-344
- Anderson, D.** (1989), *Theory of the Earth*, Blackwell Science Publications, Oxford
- BABEL Working Group** (1990), Evidence for early Proterozoic plate tectonics from seismic reflection profiles in the Baltic shield, *Nature* 348, 34-38
- Balling, N.** (2000), Deep seismic reflection evidence for ancient subduction and collision zones within the continental lithosphere of north-western Europe, *Tectonophysics* 329, 259-291
- Behm, M., Brückl, E., Mitterbauer, U.**, A new seismic model of the Eastern Alps and its relevance for Geodesy and Geodynamics, *Österreichische Zeitschrift für Vermessung und Geoinformation* (2/2007), 121-133
- Behm, M. et al.** (2007), Application of stacking and inversion techniques to three-dimensional wide-angle reflection and refraction seismic data of the Eastern Alps, *Geophys. J. Int.* 170
- Brückl, E. et al.** (2007), Crustal structure due to collisional and escape tectonics in the Eastern Alps region based on profiles Alp01 and Alp02 from the Alp2002 seismic experiment, *Journal of Geophysical Research*, Vol. 112
- Brückl, E., Mitterbauer, U., Behm, M. and Working Groups CELEBRATION 2000 & ALP 2002** (2006). Studies on Crustal Structure and Gravity in the Eastern Alps. In *Geodetic Deformation Monitoring: From Geophysical to Engineering Roles*. IAG Symposium 131. F. Sanso and A.J. Gil (Eds). Springer, 181-192
- Calvert et al.** (1995), Archean subduction inferred from seismic images of a mantle suture in the Superior Province, *Nature* 375, 670-674
- Cerveny, V.** (1987), Ray Tracing algorithms in three-dimensionally laterally varying layered structures, *Seismic Tomography*, Reidel Publishing Company, 99-134
- Cerveny, V.** (2001), *Seismic Ray Theory*, Cambridge University Press, 109
- Christensen, N., Mooney, W.** (1995), Seismic velocity structure and composition of the continental crust: A global view, *J. Geophys. Res.* 100, 9761-9788
- Cook, F., Hall, K., Roberts, B.** (1998), Tectonic delamination and subcrustal imbrication of the Precambrian lithosphere in northwestern Canada mapped by LITHOPROBE, *Geology* 26, 839-842
- Cook, F., Velden, A., Hall, K.** (1999), Frozen subduction in Canada's northwest territories: LITHOPROBE deep lithospheric reflection profiling of the western Canadian shield, *Tectonics* 18, 1-24

- DEKORP-BASIN Research Group** (1999), Deep crustal structure of the Northeast German basin: New DEKORP-BASIN '96 deep-profiling results, *Geology* 27, 55-58
- Doglioni, C. & Bosselini, A.**, (1987). Eoalpine and mesoalpine tectonics in the Southern Alps. *Geologische Rundschau*. 76(3), 735–754
- Hansen, T., Balling, N.** (2003), Upper mantle reflectors: modelling of seismic wavefield characteristics and tectonic implications, *Geophys. J. Int.* 157, 664-682
- Hole, J.** (1996), Inversion of three-dimensional wide-angle seismic data from the southwestern Canadian Cordillera, *Journal of Geophysical Research*, Vol. 101, 8503-8529
- Hole, J., Zelt, B.** (1994), 3-D finite-difference reflection travel times, *Geophys. J. Int.* 121, 427-434
- Hrubcova, P., Sroda, P., Spicak, A., Guterch, A., Grad, M., Keller, R., Brückl, E., Thybo, H.** (2005). Crustal and uppermost mantle structure of the Bohemian Massif based on data from CELEBRATION 2000 Experiment, *Journal of Geophysical Research* 110, B11305
- Kearey, P., Vine, F.** (1996), *Global Tectonics 2nd Edition*, Blackwell Science, 19-28
- Knapp et al.** (1996), A lithosphere-scale seismic image of the southern Urals from explosion-source seismic reflection profiling, *Science* 274, 226-228
- Lecomte, I., Hamran, S.** (1993), Local plane-wavenumber diffraction tomography in heterogeneous backgrounds, Part II: Green's functions and finite-difference travel times, *J. seism. Explor.* 2, 287-299
- Lenkey, L.** (1999), Geothermics of the Pannonian basin and its bearing on the tectonics of basin evolution, PhD thesis, Vrije Universiteit, Amsterdam, 215 pp
- Lie, J., Pedersen, T., Husebye, E.** (1990), Observations of seismic reflectors in the lower lithosphere beneath the Skagerrak, *Nature* 345, 165-168
- Lowrie, W.** (1997), *Fundamentals of Geophysics*, Cambridge University Press, 157-158
- Meissner, R.** (1996), Faults and folds, fact and fiction, *Tectonophysics* 264, 279-293
- MONA LISA Working Group** (1997a), Deep seismic investigations of the lithosphere in the southeastern North Sea, *Tectonophysics* 269, 1-19
- Posgay, K., Hegedus, E., Timar, Z.** (1990), The identification of mantle reflections below Hungary from deep seismic profiling, *Tectonophysics* 173, 379-385
- Posgay, K. et al.** (1995), Asthenospheric structure beneath a Neogene basin in southeast Hungary, *Tectonophysics* 252, 467-484
- Qin, F. et al.** (1992), Finite-difference solution of the eikonal equation along expanding wavefronts, *Geophysics* 57, 478-487
- Rawlinson, N., Sambridge, M.** (2003), Seismic Travel time tomography of the crust and lithosphere, *Advances in Geophysics* 46, 81-197

- Rudnick, R., Fountain, D.** (1995), Nature and composition of the continental crust: A lower crustal perspective, *Reviews of Geophysics* 33, 267-309
- Schmid, S., Fügenschuh, B., Kissling, E. & Schuster, R.** (2004). Tectonic map and overall architecture of the Alpine orogen. *Swiss J. Geosci.*, 97(1), 93–117
- Snyder, D.** (1991), Reflections from a relict Moho in Scotland, *Geodyn. Ser.* 22, 307-313
- Sroda, P. et al.** (2006), Crustal and upper mantle structure of the Western Carpathians from CELEBRATION 2000 profiles CEL01 and CEL04: seismic models and geological implications, *Geophys. J. Int.* 167, 737-760
- Steer, D., Knapp, J., Brown, L.** (1998), Super-deep reflection profiling: exploring the continental mantle lid, *Tectonophysics* 286, 111-121
- Telford, W., Geldart, L., Sheriff, R.** (1990), *Applied Geophysics* 2nd Edition, Cambridge University Press, 155-157
- Tooley, R., Spencer, T., Sagoci, H.** (1965), Reflection and transmission of plane compressional waves, *Geophysics* 30, 552-570
- Vidale, J.** (1988), Finite-difference calculation of travel times, *Bull. seism. Soc. Am.* 78, 2062-2076
- Vidale, J.** (1990), Finite-difference calculation of travel times in three dimensions, *Geophysics* 55, 521-526
- Vissers, R., Drury, M., Newman, J., Fliervoet, T.** (1997), Mylonitic deformation in upper mantle peridotites of the North Pyrenean Zone (France): implications for strength and strain localization in the lithosphere, *Tectonophysics* 279, 303-325
- Vissers, R., Drury, M., Hoogerduijn Strating, E., Spiers, C., van der, Wal D.** (1995), Mantle shear zones and their effect on lithosphere strength during continental breakup, *Tectonophysics* 249, 155-171
- Warner, M., McGeary, S.** (1987), Seismic reflection coefficients from mantle fault zones, *Geophys. J. R. astr. Soc.* 89, 223-230
- Yilmaz, O.** (1987), *Seismic Data Processing*, SEG, 1346-1351; 2014-2019

### **Website References**

[www.gupf.tu-freiberg.de/geologie/geo\\_minerale.html](http://www.gupf.tu-freiberg.de/geologie/geo_minerale.html); viewed in July 2009

Documentation to the package ‘ANRAY’: <http://seis.karlov.mff.cuni.cz>; viewed in October 2008

[www.earthscrust.org/earthscrust/science/transects/drum\\_scotland.html](http://www.earthscrust.org/earthscrust/science/transects/drum_scotland.html); viewed in January 2009

PREM Model by Dziewonski & Anderson, 1981:

[http://geophysics.ou.edu/solid\\_earth/prem.html](http://geophysics.ou.edu/solid_earth/prem.html); viewed in July 2009

School of Geosciences, The University of Sydney:  
[www.geosci.usyd.edu.au/users/prey/Geol-1002/HTML.Lect1/sld015.htm](http://www.geosci.usyd.edu.au/users/prey/Geol-1002/HTML.Lect1/sld015.htm); viewed in July 2009



# Acknowledgement

---

I would like to thank Michael Behm (Technical University of Vienna) for providing me with this topic and for supervising my thesis. He always supported me when problems occurred and he spent a lot of time with me discussing various topics. I am very grateful for his continuous contribution of new ideas.

# Curriculum Vitae

## Personal Data

**Name:** Thomas Oeberseder  
**Date of birth:** 21<sup>st</sup> August 1984, Grieskirchen  
**Nationality:** Austrian  
**Marital Status:** Single

## Education

**2004-2009:** MSci studies in Geophysics at the University of Vienna  
**1999-2003:** Secondary School in Grieskirchen

## Work experience

**2007:** Internship at ExxonMobil Production Germany, Hanover

## Bibliography

**2009:** Oeberseder, T. and Behm, M.; Poster presentation at EGU Vienna; 'Upper-mantle reflections from the Alpine-Carpathian-Pannonian transition zone'

## Further Information

**Languages:** English, German, French  
**Computer Skills:** MS Office, Matlab, Anray, ProMax, Oasis Montaj, Surfer